THE TECHNIQUE OF

ČERENKOV RING IMAGE DETECTION

Proefschrift

ter verkrijging van de graad
van Doctor aan de Rijksuniversiteit te Leiden,
op gezag van de Rector Magnificus Dr. J.J.M. Beenakker,
hoogleraar in de faculteit der Wiskunde en Natuurwetenshappen,
volgens besluit van het College van Dekanen
te verdedigen op woensdag 28 maart 1990
te klokke 14.15

door

Dirk Langerveld

geboren te Poortugaal in 1961

Stellingen

behorende bij het proefschrift

The Technique of Čerenkov Ring Image Detection

1. Het gebruik van vaste stof radiatoren in 'Ring Imaging Čerenkov' detektoren zoals de DELPHI centrale RICH detektor biedt grote voordelen boven vloeistof radiatoren. Met materialen zoals Silica Aerogel (Henning *et al.*) en gecomprimeerd kwartspoeder (Linney *et al.*) zijn radiatoren te construeren met een brekingsindex tussen 1.01 en 1.20.

    S. Henning et al., *Physica Scripta 23 (1981) 697*
    A. Linney et al., *Nucl. Instr. and Meth. 100 (1972) 545*

2. De parametrisatie door Arnold *et al.* van de absorptielengte voor ultraviolet licht in TMAE-damp als funktie van de temperatuur is onjuist.

    R. Arnold et al., *Nucl. Instr. and Meth. A270 (1988) 289*
    dit proefschrift, formule 4.6

3. De discrepantie tussen de absolute opbrengst van de K-lijnen in het röntgenspektrum uitgezonden door antiprotonisch waterstof (protonium), gemeten door Van Eijk *et al.* en Baker *et al.*, kan verklaard worden door de veronderstelling dat er een hoekcorrelatie bestaat tussen de richting waarin een röntgenquantum wordt uitgezonden en de richtingen waarin de in het annihilatieproces gecreëerde deeltjes uitgezonden worden.

    C.W.E. van Eijk et al., *Nuclear Physics A486 (1988) 604*
    C.A. Baker et al., *Nuclear Physics A483 (1988) 631*

4. De werkzame doorsnede voor de binding van elektronen aan C_5F_{12}-molekulen zoals bepaald door Fraissard *et al.* is een orde van grootte te hoog doordat de gebruikte formule onjuist is.

    D. Fraissard et al., *Nucl. Instr. and Meth. A252 (1986) 524*
    dit proefschrift, formule 3.64

5. Om de ruimtelading in een driftdetektor te kunnen berekenen in het geval dat TMAE-damp toegevoegd is aan het driftgas is het noodzakelijk dat de mobiliteit van TMAE-molekulen experimenteel bepaald wordt.

6. Diskrete magnetische niveaus in niet-periodieke superroosters (GaAs-$Ga_{1-x}Al_xAs$) in een hoog (≥ 1 T) magnetisch veld, evenwijdig aan de groeirichting, verbreden als funktie van het magnetische veld, dit in tegenstelling tot diskrete magnetische niveaus in periodieke superroosters.

   D. Toet, ICSP-conferentie Thessaloniki 1990

7. De belangrijkste beperking voor het gebruik van microstrip detektoren onder de zware experimentele omstandigheden bij toekomstige versnellers met hoge luminositeit (SSC, LHC) is hoogst waarschijnlijk het optreden van een snelle veroudering van de detektoren die zich manifesteert in een toename van de ruis en een afname van de pulshoogte.

8. Het is een verheugende ontwikkeling dat wetenschapsfilosofen en -historici, die zich lange tijd beperkt hebben tot de theoretische kant van de wetenschap, tegenwoordig meer en meer hun aandacht op het experiment richten.

   A. Franklin, The Neglect of Experiments (Cambridge U.P., 1986)
   P. Galison, How Experiments End (Chicago U.P., 1987)

9. Over honderd jaar zal CERN een museum zijn. Het nageslacht zal ons er erkentelijk voor zijn als we het versnellerspark en de (afgedankte) experimenten als wetenschappelijke monumenten in ere houden.

10. Het is opmerkelijk dat ruim twintig jaar na de ontdekking van dradenkamers het klaarblijkelijk nog steeds niet mogelijk is om de vaardigheden nodig voor het bouwen van deze detektoren uit de literatuur te leren.

11. Hij was in Dresden. (....) Hij dacht, als ik niet het besef heb dat ik in Dresden ben, waar ben ik dan? (....) Hij herinnerde zich iets, dat hij ergens gelezen had (of had hij het zelf bedacht?): *De ziel gaat te paard.*

    Harry Mulisch, Het Stenen Bruidsbed (De Bezige Bij, 1959)

12. Vrouwen zijn een bron van leven.

THE TECHNIQUE OF

ČERENKOV RING IMAGE DETECTION

Proefschrift

ter verkrijging van de graad
van Doctor aan de Rijksuniversiteit te Leiden,
op gezag van de Rector Magnificus Dr. J.J.M. Beenakker,
hoogleraar in de faculteit der Wiskunde en Natuurwetenshappen,
volgens besluit van het College van Dekanen
te verdedigen op woensdag 28 maart 1990
te klokke 14.15

door

Dirk Langerveld

geboren te Poortugaal in 1961

Promotiecommissie:

Aan mijn ouders

Contents

Chapter 1

Introduction

1.1 General introduction

Throughout the history of mankind scientists are looking for structure in a natural environment that at first sight seems to be chaotic. The object of science is not to study the structures themselves but to obtain insight in the basic phenomena behind them. A famous example is the heliocentric astronomical model suggested by Copernicus, confirmed with empirical evidence by Galilei, which formed the basis for Kepler's laws of planetary motion, leading to Newton's concept of the gravitational force. Other examples are the formulation of electro-magnetism by Maxwell; Darwin's theory of evolution presented in "The Origin of Species" and Mendeleev's periodic table of elements.

Bearing the achievements of science in mind one could foresee that one day humanity would be capable of understanding all phenomena. An area of science where this utopia is still far away is that of elementary particles physics, also called high energy physics. It studies the elementary particles that constitute matter and the interactions between them. For reasons that are still unclear, the interactions fall into four types, the electromagnetic, weak, strong and gravitational interaction.

The present state of art in elementary particles physics is called the Standard Model. It is based on the Electro-Weak Theory of Glashow, Weinberg and Salam that unifies the electro-magnetic and the weak interaction, and on the Quantum Chromo-Dynamics theory, that describes the strong interaction. Up till now (january 1990) no experimental evidence against the Standard Model has been found.

In order to create possibilities for further tests of the Standard Model and for verification of its predictions, a new accelerator (LEP) has been constructed at CERN, the European centre of high energy physics. An apparent contradiction is that in order to study the smallest imaginable particles the biggest imaginable machines are necessary. One of the four experiments located along the LEP accelerator is the DELPHI experiment.

The subject of this thesis is the method of particle identification by using ring imaging Čerenkov (RICH) detectors and the application of this method in the DELPHI barrel RICH detector. The outline is as follows. The remaining part of this chapter is devoted

to a description of the LEP machine and the DELPHI detector. After an introduction
to Čerenkov radiation and its applications in chapter 2, an overview is presented of the
drift properties of electrons in gases that are relevant for RICH detectors. A detailed
description of the barrel RICH detector is given in chapter 4. The last three chapters
contain experimental data obtained with prototypes and with the final components of the
detector. The subject of chapter 5 is the wire chamber used for the barrel RICH detector,
except for its gating system which is presented in chapter 6. In chapter 7 attention is given
to the problems associated with electron drift over long distances.

1.2   The LEP collider

Presently the biggest particle accelerator ever constructed is the Large Electron Positron
(LEP) collider. The machine is positioned in a tunnel with a circumference of 27 km
situated at a depth of about 100 m. The reason for the exceptional size of the collider
is to limit the energy loss by synchrotron radiation of the particles. The radiative energy
loss per revolution is inversely proportional to the radius of curvature and increases with
the fourth power of the energy. The electrons and positrons are circulating in one vacuum
tube, with the same energy but in opposite directions. The maximal energy per particle
is limited in the initial phase to 50 GeV. Later this will be up-graded to 100 GeV. Both
types of particles are concentrated in 4 bunches with a length of 10 cm each. Only at 4 of
the interaction regions experiments have been designed.

The four experiments are called OPAL, ALEPH, L3 and DELPHI. Each collaboration
consists of several hundreds of physicists originating from many countries. Although the
aim of all four experiments is an optimal detection of all particles that are created in the
collisions between electrons and positrons, some interesting differences can be observed.
The DELPHI experiment is described in the next section. Of the other three experiments
only the most striking properties are mentioned here.

The most conservatively designed experiment is OPAL. A big jet chamber (radius 1.9
m; length 4 m; pressure 4 bar) is used as the central tracking detector, located in a magnetic
field of 0.4 T. The chamber records the tracks of charged particles within a solid angle close
to 4π with good spatial and double track resolution. The momentum resolution is $0.2 \cdot p_t\%$
where p_t is the transverse momentum expressed in GeV/c. Conventional calorimeters
provide accurate energy information.

The tracking chamber in the ALEPH experiment is a high resolution TPC (radius 1.8
m; length 2x2.2 m). The magnetic field generated by a superconducting coil is 1.0 T. The
momentum resolution in combination with a micro vertex detector is $0.12 \cdot p_t\%$.

In the design of the L3 experiment emphasis is given to the electromagnetic calorimeter
and the muon detector. The calorimeter consists of 12000 bismuth germanium oxide (BGO)

cristals. An energy resolution of $1.2\%/\sqrt{E[GeV]}$ can be achieved. The muon detector consists of 3 layers of drift chambers, 1.2 m apart. The muon detector is situated inside the magnetic coil (field 0.5 T). With its radius of 6.8 m it is the largest conventional magnet ever constructed. The muon detector was designed to have a momentum resolution of 2% for muons with an energy of 45 GeV.

The tunnel for the LEP collider including the experimental halls has been constructed over a period of 4 years. Installation of the experiments was started at the end of 1987. In june 1989 the first particle beams were circulating in the LEP machine. A first pilot run for physics was performed in august 1989.

1.3   The DELPHI detector

The most intricate of the four LEP experiments is DELPHI [1, 2], a DEtector with Lepton, Photon and Hadron Identification. It combines a good 3-dimensional track localization and a reasonable energy resolution with an exceptionally good identification of leptons, photons and hadrons. Apart from the standard particle identification by dE/dx measurement, DELPHI is equipped with ring imaging Čerenkov detectors; this forms its main distinction from the other LEP experiments. A superconductive solenoid (radius 2.6 m), at present the biggest ever constructed, creates a magnetic field of 1.2 T, enabling high resolution momentum determination.

The detector is subdivided into a cylindrically shaped barrel part and two end caps. Using cylindrical coordinates r, ϕ and z with the z-direction along the beam axis, the barrel part covers: $40° < \phi < 140°$.

Starting from the interaction region and going outwards the following detector components are shown in the cross section of figure 1.1.

- The micro vertex detector; it consists of two layers of silicon strip detectors. The detector is located at a radius of 9 cm around the centre of the beam pipe. The aim is an accuracy in the rϕ-coordinate of 5 μm, to obtain a good reconstruction of the primary and secondary vertices.

- The inner detector consists of a jet chamber (from r=12 to r=22 cm) and 5 trigger layers. The detector combines the availability of fast trigger information with an accurate determination of tracks close to the interaction region. Resolutions of 100 μm in rϕ and 200 μm in the z-coordinate are feasible.

- The central detector is a large volume time projection chamber (TPC) working at atmospheric pressure and designed with the following aims: good two-track separation with 3-dimensional localization, particle identification by dE/dx measurement and good momentum resolution. A position resolution in rϕ of 250 μm and in z of
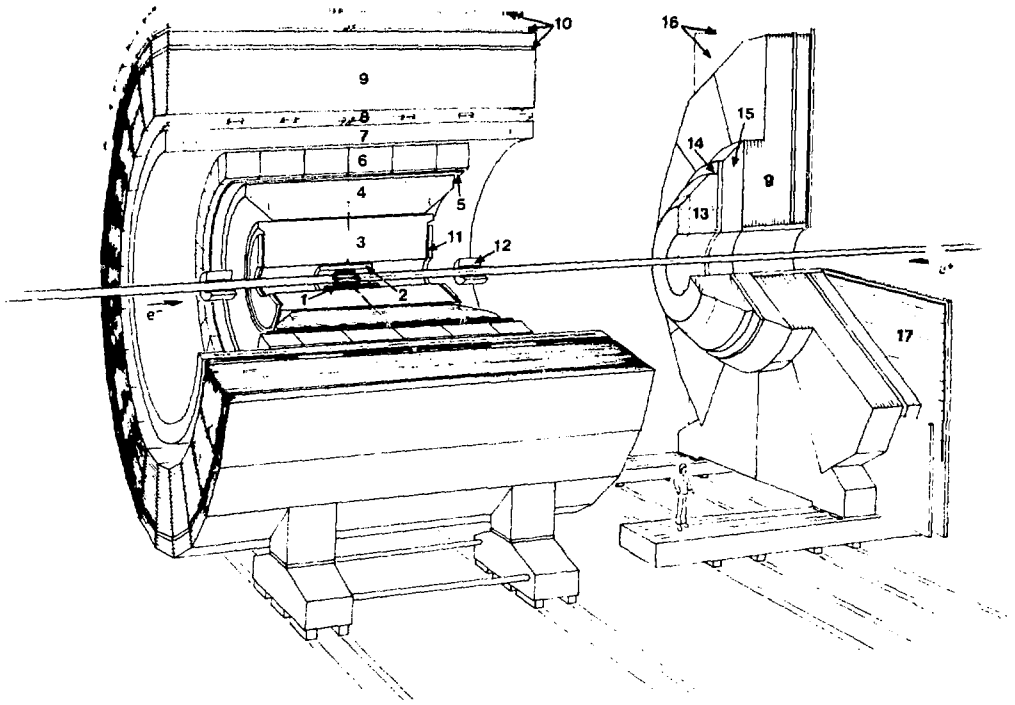
Figure 1.1: The DELPHI detector; (1) vertex detector; (2) inner detector; (3) TPC; (4,13) RICH detectors; (5) outer detector; (6,15) electromagnetic calorimeters; (7) superconducting solenoid; (8,17) scintillators; (9) hadron calorimeter; (10,16) muon detectors; (11) forward chamber A; (12) SAT; (14) forward chamber B.

1 mm are foreseen. If the TPC information is combined with the information from the vertex, inner and outer detectors a momentum resolution $\sqrt{(0.06 \cdot p_t)^2 + (1.5)^2}\%$ can be obtained.

- In the barrel RICH hadron identification in the energy range from 2 to 25 GeV can be obtained. The barrel RICH is described in detail in chapter 2 and 4.

- The outer detector, located at a radius of 200 cm, is the last tracking chamber inside the magnetic field. It provides a position resolution in rϕ of 300 μm and in z of 10 cm. The detector plays an important part in the first level trigger.

- The electromagnetic calorimeter is a high density projection chamber (HPC). It consists of alternating layers of lead sheets and drift chambers. An energy resolution of about $25\%/\sqrt{E}$ can be obtained.

- The first detector outside the magnet coil is a layer of scintillating counters. It offers a fast signal for the first level trigger and an anti-coincidence shielding against cosmic

rays.

- The hadron calorimeter determines the energy of hadrons with a resolution of about $100\%/\sqrt{E}$. The calorimeter is incorporated in the return yoke of the magnet.

- The muon detector consists of two layers with drift chambers. One layer is inside the hadron calorimeter, the other layer forms the outer boundary of DELPHI.

In the two forward regions one finds approximately the same structure as in the barrel region. In each end cap the following detectors are mounted:

- Two wire chambers, called forward chambers A and B, with a position resolution of 150 μm each. They provide fast trigger information for tracks in the forward directions. Chamber A is directly mounted onto the TPC.

- The functioning of the forward RICH is analogous to that of the barrel RICH. The drift of electrons perpendicular to the magnetic field is a complication. The average drift distance ($\approx$30 cm) is much smaller than in the barrel RICH, thus reducing the problem of the electron attenuation length. The positioning of the liquid radiators is optimized such that the angle between a track from the interaction region and the radiator plane is always close to 90°. As a result the foreseen performance of the forward RICH is slightly better than that of the barrel RICH.

- The forward electromagnetic calorimeter consists of 4500 lead glass blocks with phototriode read-out. Tests have shown that an energy resolution of $11\%/\sqrt{E}$ can be obtained.

- The forward hadron calorimeter is identical to the hadron calorimeter in the barrel.

- The forward muon detector consists of two layers of drift chambers, identical to the barrel muon detector.

- The small angle tagger calorimeter (SAT) covers polar angles from 2.5° to 7.2°. It consists of alternating layers of lead sheets, concentric with the beam axis and scintillating fibers running parallel to the beam. The light is collected behind the calorimeter and measured by photodiodes. The main task of the SAT is to reduce the gap in the forward region around the beam pipe, and to monitor the luminosity by measuring Bhabha-events.

Chapter 2

Čerenkov radiation and its applications

2.1   Introduction

The faint emission of a bluish-white light from transparent substances in the neighbourhood of strong radioactive sources has been observed by many workers in the field of radioactivity. The first scientist that studied this phenomenon systematically was the Russian physicist P.A. Čerenkov . Between 1934 and 1938 he performed an exhaustive series of experiments leading to the insight that the effect was different from fluorescence and other known forms of luminescence. His results were in excellent agreement with a theory proposed in 1937 by Frank and Tamm. In 1958 the Nobel Prize for physics was awarded to Čerenkov , Frank and Tamm for their work on the effect that has been named after its discoverer.

For a review of the experiments performed by Čerenkov and coworkers, the theory of Čerenkov radiation and its implications we refer to the work of Jelley [3] and Zrelov [4].

In the next section only those characteristics of the Čerenkov effect are discussed that are useful for the application of Čerenkov radiation in detectors for particle identification. Two types of Čerenkov counters are briefly discussed (section 2.3 and 2.4) before entering on the main application, as far as this work is concerned, of Čerenkov radiation in ring imaging Čerenkov detectors.

2.2   Čerenkov radiation

A charged particle moving in a transparent medium with a velocity v larger than the phase velocity of light in that medium (c/n; with n the index of refraction) emits radiation in a well defined direction. The angle between the direction of the particle and the emitted radiation, the Čerenkov angle θ_c, is given by:

$$\cos \theta_c = \frac{1}{\beta n} \qquad (2.1)$$

with $\beta = v/c$. The radiation is emitted in azimuth isotropically around the track of the particle. Since the index of refraction depends on the frequency of the emitted Čerenkov radiation ($n = n(\omega)$), also the Čerenkov angle is frequency dependent: $\theta_c = \theta_c(\omega)$. This effect is called chromatic dispersion.

At the threshold velocity for radiation $\beta_{th} = 1/n$ the Čerenkov angle is zero. For higher velocities the angle increases quickly, until β approaches 1 and the Čerenkov angle is at its maximal value: $\theta_{c,max} = \arccos 1/n$.

When dealing with relativistic particles it is often more convenient to use the Lorentz variable:

$$\gamma = \frac{E}{mc^2} = \frac{1}{\sqrt{1 - \beta^2}} \tag{2.2}$$

Inserting the above equation gives:

$$\cos\theta_c = \frac{1}{n\sqrt{1 - \frac{1}{\gamma^2}}} \tag{2.3}$$

$$\gamma_{th} = \frac{1}{\sqrt{1 - \frac{1}{n^2}}} \tag{2.4}$$

The energy radiated per unit path length l of the particle and per unit frequency interval is [3]:

$$\frac{d^2W}{dld\omega} = \frac{(Ze)^2\mu_0}{4\pi}\omega\sin^2\theta_c \tag{2.5}$$

where μ_0 is the permeability of the vacuum and Ze is the charge of the particle. Here we only consider unit charge, i.e. $Z^2 = 1$.

It is often more useful to express the radiation intensity in terms of the number of emitted photons N_e. From equation 2.5 one can deduce easily that the number of photons per unit path and per unit frequency interval is

$$\frac{d^2N_e}{dld\omega} = \frac{e^2\mu_0}{4\pi\hbar}\sin^2\theta_c \tag{2.6}$$

Equation 2.5 and 2.6 suggest that the radiated energy is infinite. This is not the case due to the frequency dependence of the index of refraction $n = n(\omega)$. Čerenkov radiation is emitted only in those frequency bands for which $n(\omega) > 1/\beta$.

It should be noted that the energy loss of a particle caused by Čerenkov radiation is about two orders of magnitude smaller then the energy loss caused by Coulomb interaction with the medium (excitation and ionization).

2.3   The threshold Čerenkov counter
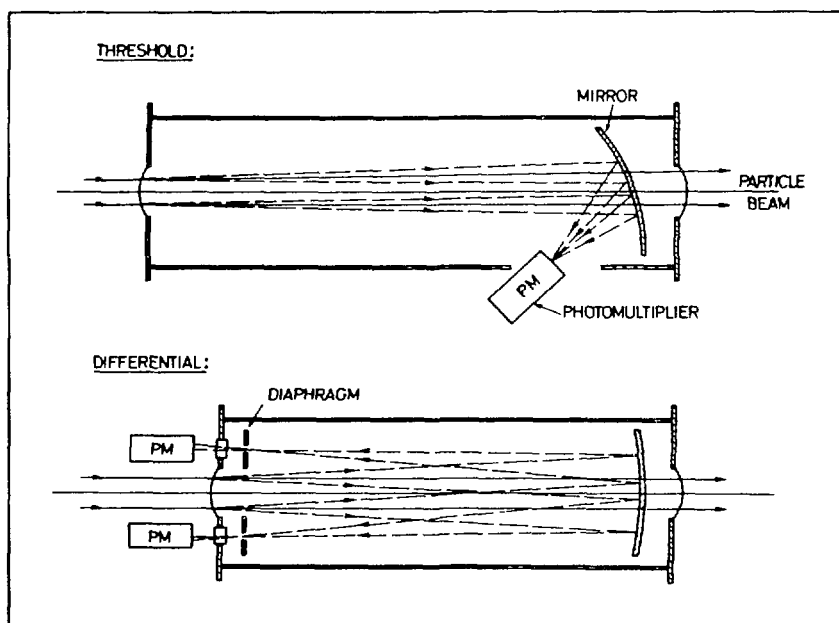
Figure 2.1: Layout of a threshold and a differential Čerenkov counter.

The threshold Čerenkov counter detects particles that have a velocity that is sufficiently high to produce Čerenkov light in its radiator. In this type of counter the Čerenkov angle is not explicitly used. The threshold velocity β_{th} depends on the refractive index n of the medium: $\beta_{th} = 1/n$. Two particles that have the same momentum but different masses m_1 and m_2 $(m_2 > m_1)$ can be discriminated by appropriate selection of the refractive index, such that particle 1 will emit Čerenkov light whereas particle 2 will not. Identification of more than two kinds of particles is possible by placing several threshold counters in series.

The layout of a threshold Čerenkov counter is shown in figure 2.1 [5]. The length of a counter can be several meters. The Čerenkov light is focussed onto a photomultiplier by means of a mirror. The choice between a gaseous, liquid or solid radiator depends on the design of the counter. A gas has the advantage that the refractive index can be changed by varying the pressure. In figure 2.2 this is illustrated with the results of two measurement taken at CERN with a threshold Čerenkov counter in a pion beam, that contained also some electrons, muons and kaons.
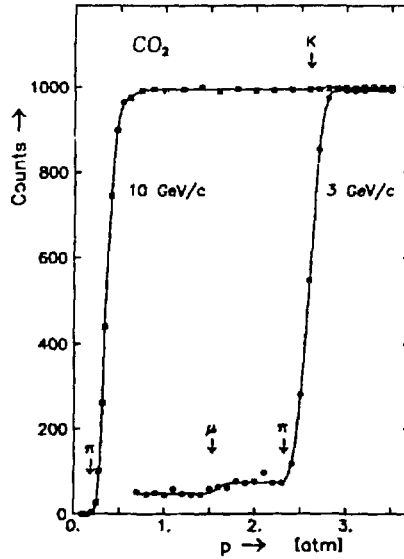
Figure 2.2: The number of detected particles in a threshold Čerenkov counter filled with CO_2 gas as a function of the pressure for beam momenta of 10 GeV/c and 3 GeV/c; for some particles the thresholds for radiation are indicated.

2.4   The differential Čerenkov counter

In a differential Čerenkov counter the emission angle of Čerenkov radiation is explicitly used. In figure 2.1 the layout is shown. The mirror with focal length f focuses the Čerenkov light on an annular diaphragm with radius r. Several photomultipliers are positioned behind the opening. The radius of the diaphragm selects the Čerenkov angle ($r = f \tan \theta_c$) and thus a small velocity interval. A velocity resolution $\Delta\beta/\beta$ of 10^{-5} can be obtained.

The main limitation for the velocity resolution is chromatic dispersion in the emitted Čerenkov light. The photomultipliers are sensitive to a certain wavelength region. Since the refractive index depends on the wavelength a spread in the Čerenkov angle can be expected. The dispersion can in first order be compensated optically. This type of detector is known as a DISC Čerenkov counter (differential isochronous self-collimating). A resolution $\Delta\beta/\beta$ of 10^{-7} has been obtained [5].

2.5   The ring imaging Čerenkov detector

The differential Čerenkov counters described in the previous section have several drawbacks. The tracks of the particles ideally should coincide with the optical axis of the counter and the detector is sensitive for only one preselected value of the Čerenkov angle. This makes the detector useless for experiments were one wants to identify particles over large solid angles and over a broad energy range. With the technique of Ring Imaging Čerenkov (RICH) detection these restrictions can be overcome. In a RICH detector the Čerenkov radiation is projected onto a medium of detection. By combining the positions of all detected photons the Čerenkov angle can be reconstructed and thus the velocity of the particle is obtained (equation 2.1). If the energy or momentum is known the mass of the particle can be calculated, thus leading finally to identification of the particle.
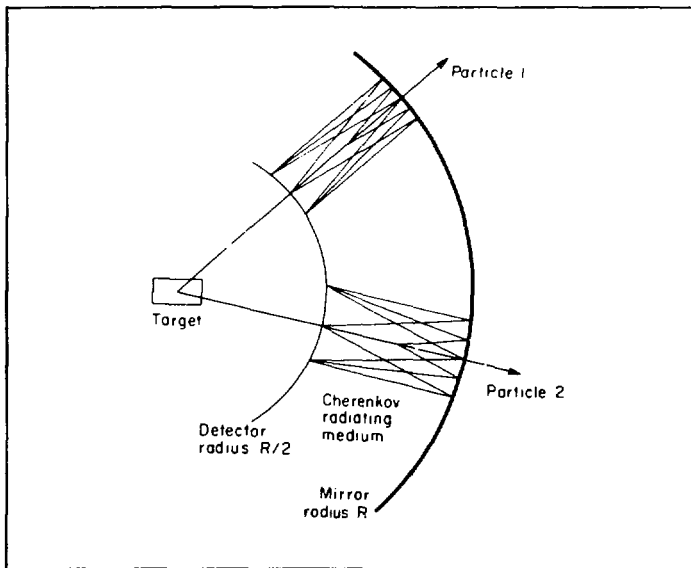
Figure 2.3: Principle of a large phase space acceptance ring imaging Čerenkov detector [6].

2.5.1   The historical development

The principle of a ring imaging Čerenkov detector is shown in figure 2.3. A spherical mirror of radius R, surrounding the interaction region at its centre, focuses the Čerenkov radiation emitted by a traversing particle on a sperical detection surface at radius $\frac{1}{2}R$. The radiating medium is between $\frac{1}{2}R$ and R. Both for particles originating from the optical centre of the mirror and for particles that are slightly off axis the image is a ring.

The photon detector ideally has the following qualities:
- It covers a large surface.
- It has a uniform sensitivity.
- The spatial position of all photons in the ring image can be obtained.
- The quantum efficiency for photon detection is high.
- A good time resolution to separate most events.

These requirements can never be met with standard techniques like photographic plates or photomultipliers. In 1977 Séguinot and Ypsilantis [6] proposed a detector based on the photo-ionization process in a gaseous volume. The thus created free electrons are detected bij a detector that allows full reconstruction of the positions where the photons were converted.
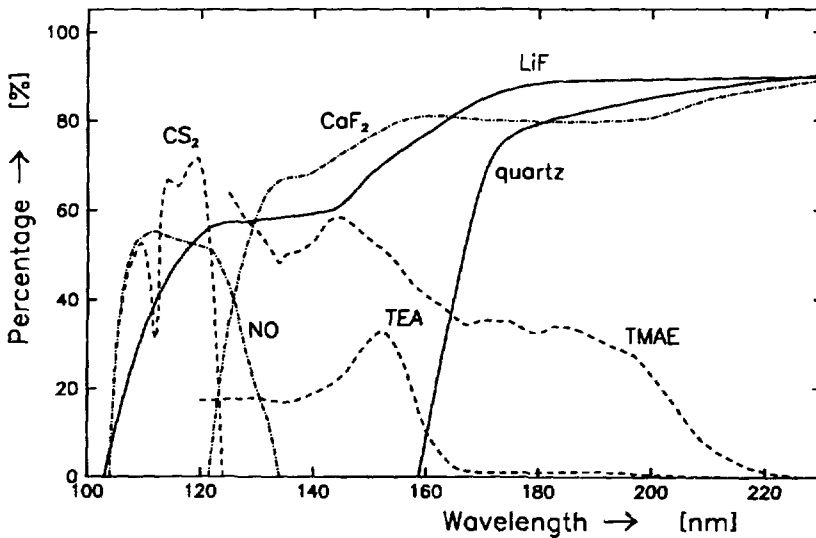
Figure 2.4: The quantum efficiency for photo-ionization in CS$_2$ [6], NO [6], TEA [7], and TMAE [7] as well as the transmission through 4 mm thick windows made of LiF [8], CaF$_2$ [8] and fused quartz [9]. The Q.E. for CS$_2$ and NO have not been corrected for losses in the entrance window (LiF) and have to be considered as lower limits.

Nitric oxyde (NO), carbon di-sulphide (CS$_2$) and benzene (C$_6$H$_6$) were considered to be of interest as photoconverters. In NO and CS$_2$ the quantum efficiency for the conversion process is above 50% (see figure 2.4), but at rather low wavelength. This demands the use of lithium fluoride (LiF) crystals as the window separating the radiator and the detector; LiF is expensive and highly hygroscopic.

A considerable improvement was the introduction of TEA [10] and TMAE [11]. TEA

(tri-ethylamine) can be used in combination with windows made of CaF_2 (figure 2.4) or MgF$_2$. TMAE (tetrakis(dimethylamino)ethylene) can be used in combination with fused quartz offering the possibility of detectors with virtually unlimited window size. The cross sections for photon absorption in TEA and TMAE are comparable. The vapour pressure of TMAE is unfortunately rather low; 0.35 Torr at room temperature, to be compared with 55 Torr for TEA. With TEA full photon absorption can be obtained in a gas layer of 1-2 mm, while with TMAE even at high temperatures (35-40)°C the absorption length is as long as 20-30 mm.
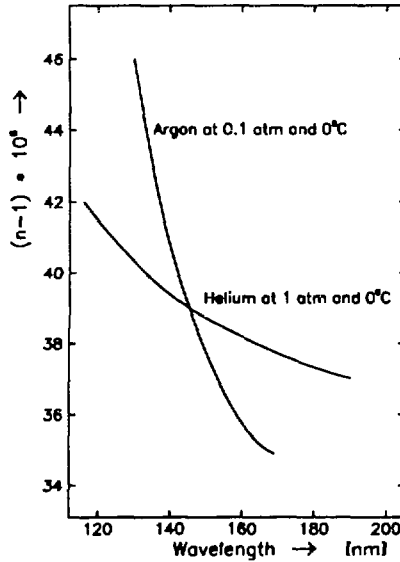
Figure 2.5: The refractive index as a function of the wavelength for argon and helium [12].

In addition to the advantage in the choice of the window materials, another advantage of shifting the wavelength interval of the detected photons to higher values, is the observation that for higher wavelengths the dependence of the refractive index on the wavelength is less. This is illustrated in figure 2.5 for argon and helium.

In order to have an efficient detection of the single electrons an high gas amplification is essential ($>10^5$). Since it was initially considered impossible to achieve such gains in a multi wire proportional chamber (MWPC) two alternatives were developed.

The first, proposed by Séguinot and Ypsilantis [6], implied the use of small cells with a needle in the centre of each of them. The needles have the same function as the anode wires in a MWPC. A photo-electron drifts towards a needle and initiates an avalanche in the high field around the tip of the needle. Even when the cells are operated at high gains (Geiger mode) the gas amplification occurs on the sharp tip only, thus offering the

possibility of big signals with a reasonable count rate. A disadvantage is the exorbitant amount of needles that have to be read out individually. With a needle spacing of 2 mm one would get $2.5 \cdot 10^5$ channels/m^2.
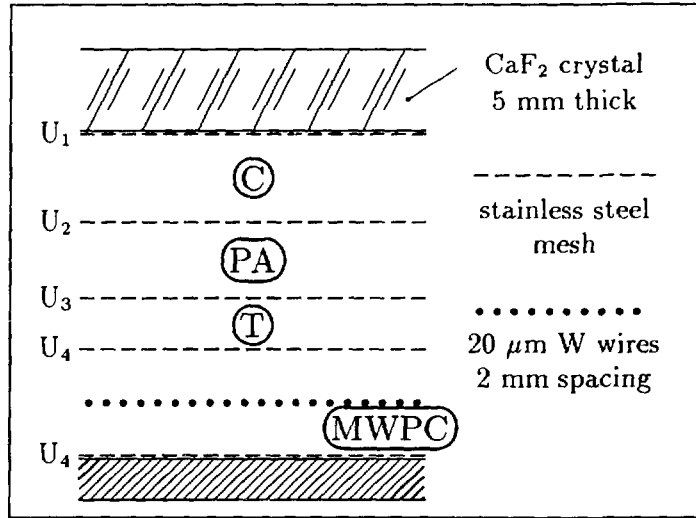
Figure 2.6: Layout of a multistep avalanche chamber [14].

The second alternative implies the use of multistep avalanche chambers (MSC), a device originally developed by Charpak and Sauli [13] to allow gated operation of proportional chambers. A MSC consists of three parallel gaps and a MWPC as illustrated in figure 2.6. In the convertion gap (C) the light transmitted through the entrance window is converted. In a low electric field the photo-electrons drift to the preamplification region (PA). This region incorporates a high field in which by avalanche amplification the amount of electrons increases with a factor 10^3-10^4. After drifting through the transfer gap (T) the electrons are detected in the MWPC, were another amplification of $\approx 10^3$ is obtained. With this device Séguinot et al.[10] demonstrated that single electrons can be detected efficiently in an argon-TEA gas filling. Operating the detector with a methane-TEA mixture it was found that an efficient detection could be obtained even without preamplification [14].

What remains after omitting the preamplification region is a conventional wire chamber were one coordinate is given by the wires and the second by cathode strip read-out. If instead of a wire chamber a drift chamber is used as shown in figure 2.7, the photo-convertion points are determined by the drift time and the wire address, leaving the possibility of measuring the third coordinate, the absorption depth, with cathode strips.

Barrelet et al.[15] demonstrated the possibility of drifting single electrons without loss over distances up to 14 cm under the condition that all dielectric walls around the drift volume are provided with field shaping conductive electrodes both on the inside and the outside.
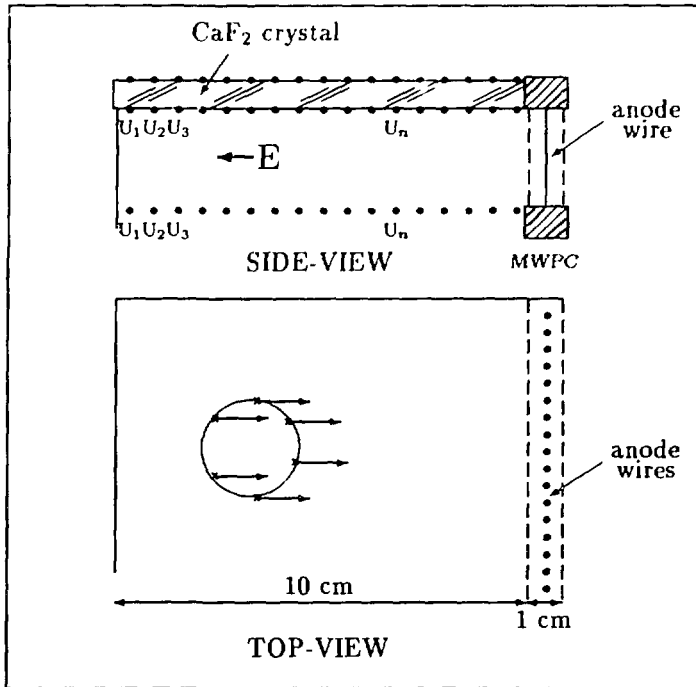
Figure 2.7: Schematic view of a drift chamber for the detection of Čerenkov ring images [14].

After solving the main technical problems, RICH detectors have been incorporated in several fixed target experiments. Examples are the EMC, NA3 and Omega experiments at CERN, and the E605 experiment at Fermilab. The first "big scale" applications in collider experiments are going to be the DELPHI experiment at CERN and the SLD experiment at SLAC.

To build a spherical detector like the one shown in figure 2.3 for an experiment that also incorporates other detectors is practically impossible. The RICH detector in the DELPHI experiment therefore is divided into three parts: two endcap ('forward') parts and a central ('barrel') part. The latter forms the main subject of this thesis. The spherical symmetry of the original principle has been adapted to the cylindrical symmetry of the barrel RICH, respecting the basic ideas of figure 2.3. For instance the task of the spherical mirror is now accomplished by smaller mirrors, arranged in rows parallel to the axis of the cylinder, together guaranteeing full angular coverage. They focus the Čerenkov light into 1.5 m long drift tubes again oriented parallel to the barrel axis. This in turn creates the possibility to equip the barrel RICH with a cylindrical liquid radiator. All this is illustrated in figure 4.1 of chapter 4 and will be discussed there in full detail.
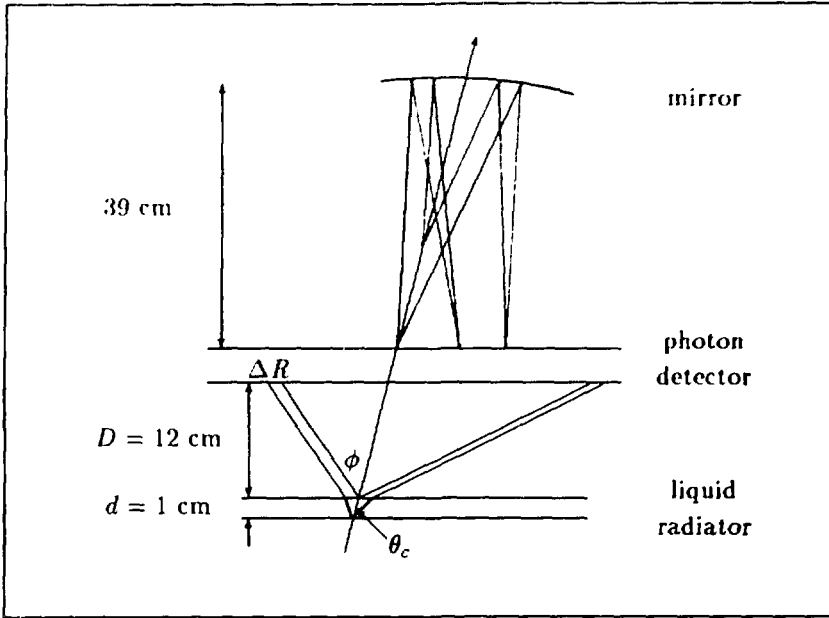
Figure 2.8: The principle of Čerenkov ring imaging in the DELPHI barrel RICH detector.

2.5.2   Applying the RICH technique: the DELPHI barrel RICH

An extensive description of the DELPHI barrel RICH detector is given in chapter 4. In this section the technique of Čerenkov ring imaging is emphasized and the particle identification that can be obtained with it. The essential features of the barrel RICH detector are shown in figure 2.8. Two radiators are combined with one photon detector. The photon detector is a drift tube, entirely constructed from quartz plates and filled with a gas mixture to which TMAE vapour is added as a photoconvertor. The reason for using two types of radiators is to extend the energy region over which particles can be identified. The Čerenkov light from the liquid radiator is projected directly onto the photon detector. This type of focussing, called proximity focussing, is only possible for thin radiators. For the Čerenkov light generated along the relatively long path in the gaseous radiator mirrors are used to focus this light as rings onto the photon detector.

One of the main conditions to be fulfilled when choosing a radiator is that it is transparent for the radiation to be detected. The energy region in which the photon detector is sensitive, is from 5.6 eV to 7.5 eV, as determined by the TMAE quantum efficiency and the quartz windows. The transparancy condition is satisfied by the noble gases, the lighter hydrocarbons and the fluorocarbons. Table 2.1 lists some candidates for the gaseous radiator with some of their relevant properties.

Radiator gas	boiling temperature	$(n-1)\cdot 10^6$ at 7 eV	$\frac{\Delta n}{n-1}$ 6.5-7.5 eV	γ_{th}	$\theta_{c,max}$ [$^\circ$]	$\frac{dN}{dL}$ photons/cm
He	-269	33	2.4%	123	0.47	0.0054
Ne	-246	64	2.5%	88	0.65	0.010
Ar	-186	300	7.0%	41	1.40	0.048
CH_4	-164	510	9.6%	31	1.83	0.082
C_2H_6	-89	898	10.0%	24	2.43	0.14
C_4H_{10}	-0.5	1500	10.7%	18	3.14	0.24
C_5H_{12}	36	1950	9.6%	16	3.58	0.31
CF_4	-128	488	2.0%	32	1.79	0.078
C_2F_6	-78	793	2.9%	25	2.28	0.13
C_4F_{10}	-8	1510	3.5%	18	3.15	0.24
C_5F_{12}	30	1750	2.9%	17	3.39	0.28
C_6F_{14}	57	1950	3.0%	16	3.58	0.31

Table 2.1: Twelve radiator gases with their relevant properties: boiling temperature [$^\circ$C], index of refraction n at 7 eV (177 nm); the full-width chromatic dispersion in the range 6.5-7.5 eV; the threshold Lorentz factor; the maximal Čerenkov angle ($\beta=1$) and the number of detected photons per unit radiation length for $\theta_c = \theta_{c,max}$ and $N_0=80$ cm^{-1} (data C_5H_{12} from [16]; all others [17]).

The ultimate angular resolution that can be obtained with a ring imaging Čerenkov detector is determined by the dispersion of the refractive index and the number of detected photons per Čerenkov ring. The variation of n in a 1 eV energy interval around 7 eV is listed in table 2.1, as well as the number of detected photons per unit of path in the radiator dN/dL. Both conditions are best satisfied by the heavy fluorocarbons. The higher boiling temperature of C_6F_{14} leads to the choice of C_5F_{12} as gaseous radiator.

The candidates for the liquid radiator are in principle the same as for the gaseous radiator. The noble gases are unattractive because of their low boiling temperature; the hydrocarbons because of their high dispersion. This leads the choice again to the heavy fluorocarbons. Since C_5F_{12} is used as gaseous radiator, C_6F_{14} is selected as liquid radiator. At a photon energy of 7 eV the index of refraction n is 1.28 whereas the dispersion is 3.4% in a 1 eV energy interval around 7 eV.

The operating temperature of the detector, 40°C, is chosen in between the boiling temperatures of C_5F_{12} and C_6F_{14}. The separation power of the barrel RICH detector will be discussed in section 2.5.5.

As neither technical nor layout dependent arguments have been used for the choice of

the radiators it is not surprising that for the CRID detector at SLAC the same radiators have been chosen [18].

The number of detected electrons N can be derived from equation 2.6 and the detection efficiency of the photon detector:

$$N = N_0 \cdot L \cdot \sin^2 \theta_c \tag{2.7}$$

where $\sin^2 \theta_c$ is averaged over the photon frequency range to which the detector is sensitive, L is the path of the particle through the radiator and N_0 is a quality factor defined as:

$$N_0 = \frac{e^2 \mu_0}{4 \pi \hbar} \int \varepsilon(\omega) d\omega \tag{2.8}$$

$\varepsilon(\omega)$ is the efficiency for detecting a photon of frequency ω that is emitted in the radiator. It contains the tranmission of windows, the mirror reflectivity, the TMAE quantum efficiency, the electron attenuation length in the drift tubes and the single electron detection efficiency of the wire chamber.

Typical values for N_0, measured in comparable experimental setups are for the gaseous radiator 80 cm^{-1} and for the liquid radiator 60 cm^{-1} [19].

2.5.3   The angular resolution with the gaseous radiator

The mean number of photons produced in the gaseous radiator (C_5F_{12}) and detected in the photon detector can be calculated with equation 2.7. Using a radiator length of 39 cm, N_0=80 cm^{-1} and $\theta_c = \theta_{c,max}$=3.39° we find: N=10.9. For a focal length of 40 cm the maximal radius of the Čerenkov rings is: $R_{max} = f \tan \theta_{c,max}$=2.4 cm.

Chromatic aberration

As was pointed out before the index of refraction depends on the frequency. Since the photon detector is sensitive for a certain bandwidth this variation in n leads to a spread in the Čerenkov angle, called chromatic aberration. For a gaseous radiator the relation between the relative spread in θ_c and in n is [17]:

$$\frac{\Delta \theta_c}{\theta_c} = \frac{\Delta n}{2(n-1)} \tag{2.9}$$

The relative spread in $(n-1)$ for C_5F_{12} is 2.9% for the energy region 6.5-7.5 eV (table 2.1). The region of sensitivity of the TMAE filled photon detector is 5.6-7.5 eV. This gives $\Delta \theta_c / \theta_c$=2.8%.

Supposing an uniform detection yield over this sensitivity region we find for the variance σ_θ of the Čerenkov angle distribution:

$$\frac{\sigma_\theta}{\theta_c} = \frac{2.8}{\sqrt{12}} = 0.81\% \tag{2.10}$$

The position resolution

The ultimate resolution that can be obtained is determined by the chromatic error. Thus the requirement for the other error contributions is that they should possibly be of the same order of magnitude or smaller. For the position resolution of a photon in a ring of radius R this means: $\sigma_R/R < 0.81\%$. As a consequence the position resolution has to be better than 0.2 mm. This requirement is technically not possible. A more realistic estimation of the position resolution of the photon detector, that includes diffusion and the resolution of the wire chamber is 1.5 mm (chapter 7) making:

$$\frac{\sigma_\theta}{\theta_{c,max}} = 6.3\% \tag{2.11}$$

The magnetic field

The DELPHI barrel RICH is placed in a magnetic field of 1.2 T along the beam axis. As a consequence the Čerenkov light is emitted in the radiator along a curved particle track. This causes a shift in the Čerenkov angle, that is equal to the change of direction of the particle:

$$\Delta\theta_c = \frac{LeB}{p_t} \tag{2.12}$$

where L is the path, B is the magnetic field, p_t is the component of the momentum perpendicular to the magnetic field; $\Delta\theta_c$ is expressed in radian. The shift is uniform in one direction, i.e. the variance averaged around the ring is a factor $2/\pi\sqrt{12}$ smaller. As an example we find for $p_t = 10$ GeV/c:

$$\frac{\sigma_\theta}{\theta_{c,max}} = 4.4\% \tag{2.13}$$

Other error sources

Multiple scattering of the particles in the radiator changes their direction and causes an additional spread. Its contribution is negligible compared to the errors mentioned before [20]. The same holds for the error caused by the change in velocity due to the energy loss of the particles.

2.5.4   The angular resolution with the liquid radiator

The mean number of photons produced in the liquid radiator (C_6F_{14}; $\Delta n/(n-1)$=3.4%; n=1.28) that are detected in the photon detector can be calculated with equation 2.7. Using a radiator length of 1 cm, N_0=60 cm^{-1} and $\theta_c = \theta_{c,max}$=38.6° one finds: N=23.4.

The angle ϕ indicated in figure 2.8 is different from the Čerenkov angle θ_c due to refraction. For a particle perpendicular to the liquid radiator the relation between ϕ and θ_c is (Snell's law):

$$\sin \phi = n \sin \theta_c \tag{2.14}$$

thus ϕ is 53.0° for β=1. With a distance between the liquid radiator and the photon detector of 12 cm the maximal ring radius is 15.9 cm for particles of normal incidence with respect to the liquid radiator.

An estimation of the angular resolution with the liquid radiator is considerably more complicated as with the gaseous radiator due to the much larger Čerenkov angle. Generally the image on the photon detector is not a ring but, depending on the angle of incidence of the track on the radiator, an ellipse or an hyperbola. The angular resolution per detected photon depends on the azimuthal angle around the particle track [19]. Due to reflection on the surface of the liquid radiator also the photon yield depends on the azimuthal angle. The evaluation of the angular resolution with the liquid radiator presented in this section will be restricted to particles of normal incidence.

Chromatic aberration

The ultimate angular resolution for the liquid radiator is limited, as for the gaseous radiator, by the chromatic dispersion of the refractive index. Knowing the variation in the refractive index, for a 1 eV energy range around 7 eV, the relative spread in the ring radius can be calculated [17]:

$$\frac{\Delta R}{R} = 5.0\% \tag{2.15}$$

The energy region for photon detection with the liquid radiator is 5.6-7.1 eV. Supposing an uniform detection yield over the sensitivity region, the variance in R is:

$$\frac{\sigma_R}{R} = 2.2\% \tag{2.16}$$

The geometrical error

The finite width d of the liquid radiator gives an uncertainty ΔR in the radius R of the Čerenkov rings projected on the photon detector at the distance D (figure 2.8). This is

called the geometrical error. For particles of normal incidence it can be evaluated as:

$$\frac{\Delta R}{R} = \frac{d}{D} \frac{\tan \theta_c}{\tan \phi} \qquad (2.17)$$

Substituting $d=1$ cm, $D=12$ cm, $\theta_c=\theta_{c,max}=38.6°$ and $\phi=53.0°$ ($\beta = 1$) gives for the variance:

$$\frac{\sigma_R}{R_{max}} = 1.4\% \qquad (2.18)$$

For smaller Čerenkov angles the error is slightly bigger; for instance for $\theta_c=\frac{1}{2}\theta_{c,max}$ the relative variance is 1.8%.

The position resolution

Due to the larger radius of the Čerenkov rings from the liquid radiator as compared to those of the gaseous radiator, the resolution of the photon detector is less important. Using again a resolution of 1.5 mm (including diffusion) we find for $R = R_{max}$:

$$\frac{\sigma_R}{R_{max}} = 1.0\% \qquad (2.19)$$

Other error sources

The influence of the magnetic field is negligible due to the thinness of the liquid radiator. All other error sources like multiple scattering and energy loss can be shown to be irrelevant.

2.5.5   Particle identification

To evaluate the power for particle identification in the DELPHI barrel RICH detector the errors quoted in section 2.5.3 and 2.5.4 will be used. Adding the errors quadratically gives:

$$\begin{aligned} \text{gaseous radiator} \quad \frac{\sigma_R}{R_{max}} &= \frac{\sigma_\theta}{\theta_{c,max}} = 7.7\% \\ \text{liquid radiator} \quad \frac{\sigma_R}{R_{max}} &= 2.8\% \end{aligned}$$

The maximal Lorentz factor γ_{max} for which particle identification is still reasonably accurate is determined by the radius R for which:

$$\Delta R = R_{max} - R \qquad (2.20)$$

where ΔR is the uncertainty on the mean radius of a ring. If the image from the liquid radiator is not a ring but an ellipse or an hyperbola, equation 2.20 has to be formulated differently. Requiring a 90% confidence level (2.5σ) and using the mean number of photons per liquid and per gaseous ring, the maximal Lorentz factors can be calculated for both

particle	mass [MeV/c^2]	liquid radiator		gaseous radiator	
		E_{min} [GeV]	E_{max} [GeV]	E_{min} [GeV]	E_{max} [GeV]
e^+, e^-	0.511	0.0009	0.0057	0.010	0.026
μ^+, μ^-	105.7	0.18	1.2	2.1	5.3
π^+, π^-	139.6	0.24	1.6	2.8	7.0
K^+, K^-	493.7	0.84	5.5	9.8	24.8
$p, \bar{p}$	938.3	1.6	10.5	18.7	47.2

Table 2.2: An indication of the energy intervals in which particle identification can be obtained with the DELPHI barrel RICH detector.

radiators: $\gamma_{l,max}$=11.2 and $\gamma_{g,max}$=50.3. These have been used to calculate the maximal energies E_{max} for several particles, listed in table 2.2.

Just above the threshold for Čerenkov radiation the photon yield is low. The number of photons per ring is distributed according to Poisson statistics. If a percentage δ=5.0% of wrongly identified particles is accepted the minimal value for the mean number of detected photons per ring: $N = -\ln\delta$=3.0 can be used to calculate the minimal Lorentz factor for both radiators: $\gamma_{l,min}$=1.7 and $\gamma_{g,min}$=19.9. These have been used to calculate the minimal energies E_{min} listed in table 2.2.

The intervals for which particle identification is possible are shown in table 2.2. The π/K separation is obtained from 0.24 GeV to 5.5 GeV with the liquid radiator and from 2.8 GeV to 24.8 GeV with the gaseous radiator. Pions in the interval from 7.0 GeV to 9.8 GeV radiate at nearly maximal Čerenkov angles whereas kaons are below threshold; the separation is obtained by using the gaseous radiator as a threshold Čerenkov counter.

The K/p separation is obtained from 0.84 GeV to 10.5 GeV with the liquid radiator and from 9.8 GeV to 47.2 GeV with the gaseous radiator. There is some overlap between the energy regions of both radiators, making the K/p separation for particles that are perpendicular to the liquid radiator reasonable. The situation is different for particles with non-perpendicular incidence on the liquid radiator. For these particles the error on the Čerenkov angle for the liquid radiator is bigger which reduces E_{max} for the liquid radiator. As a result the K/p separation is less efficient from 8 GeV to 11 GeV.

To improve the K/p separation the barrel RICH will be operated at an overpressure of 0.3 bar. The change of the refractive index is given by the Lorentz-Lorenz law [5]:

$$\frac{n^2 - 1}{n^2 + 2} = \frac{R \cdot \rho}{M} \qquad (2.21)$$

where R is the molecular refractivity, M is the molecular weight and ρ is the gas density.

For normal pressures equation 2.21 can be approximated to high accuracy by:

$$(n-1) = (n_0 - 1)\frac{p}{p_0} \tag{2.22}$$

where n_0 is the index of refraction at the pressure p_0. Using the refractive index quoted in table 2.1 for 1 bar, the value for 1.3 bar is 1.002275. As a result the minimum energy for particle identification in the gaseous radiator is lowered with 16%.

Chapter 3

Drift properties of electrons in gases

3.1 Introduction to wire and drift chambers

Multi Wire Proportional Chambers (MWPC) are widely used in high energy physics for the detection of charged particles. Their main properties are: high rate capability, good position and time resolution. Hardly any disturbance is given to passing particles because the active volume of a MWPC consists of gas. The first MWPC was constructed and operated 20 years ago by Charpak and his collaborators [21]. Since then an enormous evolution occurred and nowadays MWPC's exist in many sizes and shapes. Their applications are not limited to high energy physics. Other fields are nuclear medicine, biology, X-ray spectroscopy and nuclear physics [22].

A MWPC generally consists of a plane of thin anode wires sandwiched between two cathode planes (fig. 3.1a). A charged particle passing through the gas volume will ionize the gas along its track (electromagnetic interaction). Because the anodes have a positive potential relative to the cathodes, the electrons drift to the anode wires. Close to the anode wire the field is high enough to increase the energy of the electron such that they are able to ionize the molecules of the gas. In this way new free electrons are created which will ionize as well, etc. By this avalanche mechanism the original number of electrons is multiplied by a factor of order 10^3–10^5, giving rise to pulses that can be detected electronically. For an extensive treatment of MWPC's we refer to Sauli [23].

With a MWPC one coordinate of the track (the x-coordinate in fig. 3.1a) is measured with an accuracy that is equal to the distance between the anode wires. Its inventors [21] already realized that the position accuracy could be improved if also the drift time of the electrons is measured. The detector is then called a drift chamber.

In fig. 3.1b a drift chamber with a different layout is shown. Here the drift time gives the z-coordinate. The electrons drift in a homogeneous field that is created by field shaping wires.

Combining the design of the wire chamber in fig. 3.1a with that of the drift chamber in fig. 3.1b leads to a design like fig. 3.1c which is the design of the DELPHI barrel-RICH drift chambers. An array of wires is used to detect the drifting electrons and determines the
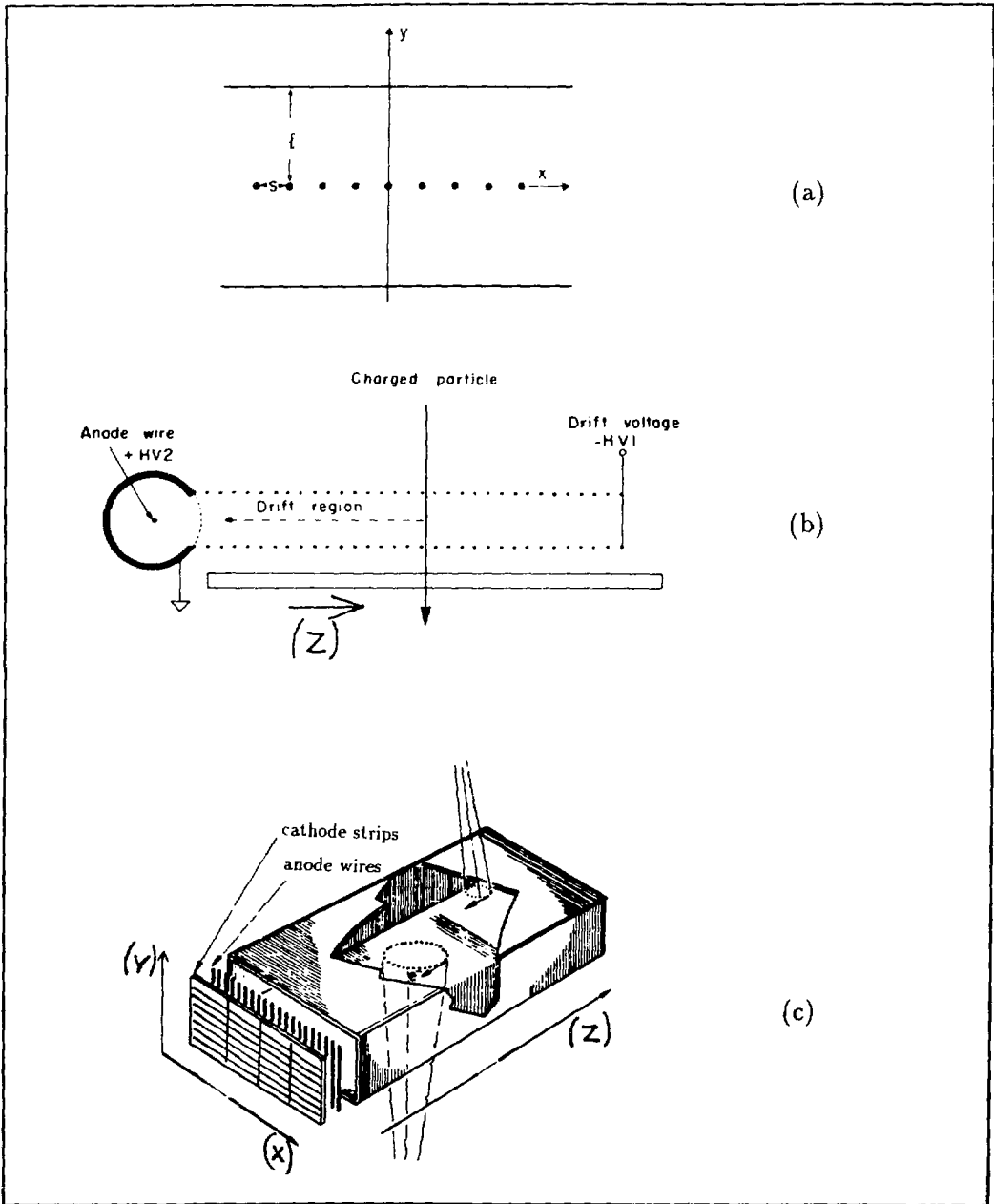
Figure 3.1: Schematic layout of: (a) a classical MWPC, (b) a drift chamber with a single wire and (c) a multi wire drift chamber as it is used for the barrel RICH.

x-coordinate. The drift time gives the z-coordinate. There is a cathode plane behind the anode wires subdivided into strips. The induced signals on the strips give the y-coordinate. Thus it is possible to make a 3-dimensional reconstruction of the creation point of every detected electron. In the chapters 4-7 a more extensive description of the detector will be given. The remaining part of this chapter is dedicated to a description of the drift gas properties that crucially influence the quality of the detector and to the theory that is behind these properties.

3.2 Introduction to drift gases and their properties.

In the absence of an electric field free electrons in a gas move randomly. Their energy distribution is Maxwellian with a mean value of $\frac{3}{2}kT$ (≈ 0.04 eV at 20°C). In the presence of an electric field $\vec{E}$ free electrons move against the direction of the field quickly reaching a constant drift velocity $\vec{w}$. The mean electron energy will increase substantially to ≈ 1 eV for typical field strengths used for drifting.

An electron with an energy ϵ of 1 eV has a random velocity $|\vec{v}|$ of $5.9 \cdot 10^5$ m/s. The drift velocity depends on the gas composition and the applied field $\vec{E}$; for not to high fields ($E < 3$ kV/cm) it is less then $5 \cdot 10^4$ m/s. The difference between the random velocity and the drift velocity is one order of magnitude. This shows that free electrons in a gas move randomly with a high velocity, undergoing many collisions with the gas molecules but move only slowly against the direction of the electric field.

The fact that the electrons reach a constant drift velocity indicates that besides gaining energy from the field, the electrons loose energy in the frequent collisions with the gas molecules. We can distinguish between elastic and inelestic collisions. In inelastic collisions energy is lost due to excitation of electronic, rotational and vibrational levels or ionization.

An electron (mass m) that is scattered in an *elastic collision* with a molecule (mass M) over an angle θ will loose a fraction of its energy ($\epsilon = \frac{1}{2}mv^2$):

$$\frac{\Delta \epsilon}{\epsilon} = 2\frac{\Delta v}{v} = 2\frac{n_i}{M}(1 - \cos\theta) \tag{3.1}$$

Assuming an isotropic angular distribution we can calculate the mean fractional energy loss per collision, Λ, for elastic collisions only,

$$\Lambda = <\frac{\Delta \epsilon}{\epsilon}> = 2\frac{m}{M} \tag{3.2}$$

Though this fraction is smaller than 10^{-3}, elastic collisions contribute substantially to the energy loss because of the high collision rate of drifting electrons.

The mean free path l is defined as the mean distance an electron travels between two

collisions. Then:

$$l = \frac{1}{n\sigma_i} \tag{3.3}$$

where n is the gas concentration and σ_i is the cross section for the interaction concerned. Several different mean free paths can be defined like a momentum transfer mean free path and a mean free path for ionization.

The electron mobility μ is defined as:

$$\mu = \frac{\vec{w}}{\vec{E}} \tag{3.4}$$

Since the drift velocity is proportional to the field in a limited region only, the mobility will generally depend on the electric field: $\mu = \mu(\vec{E})$.

An infinitely small cloud of electrons that starts to drift will slowly increase in size due to the random motion of the electrons. This effect is called diffusion. The diffusion coefficient D is defined by the diffusion equation [24]:

$$\frac{\partial}{\partial t}\rho = D\nabla^2\rho \tag{3.5}$$

where ρ is the normalized spatial density of the electrons. Formally equation 3.5 is only valid in the absence of a drift field. A solution of equation 3.5 is:

$$\rho(x,y,z) = \frac{1}{(4\pi Dt)^{\frac{3}{2}}}\exp-\frac{(x^2+y^2+z^2)}{4Dt} \tag{3.6}$$

which is a Gaussian distribution with standard deviation σ:

$$\sigma^2 = <x^2> = <y^2> = <z^2> = 2Dt \tag{3.7}$$

as a measure of its width.

The characteristic energy ϵ_k is defined as:

$$\epsilon_k = \frac{eD}{\mu} \tag{3.8}$$

This parameter occurs in older diffusion studies ([35]-[34]) where the spread of an electron cloud was measured for a fixed diffusion length L as a function of the electric field:

$$\sigma = \sqrt{\frac{2DL}{w}} = \sqrt{\frac{2L}{E}\frac{D}{\mu}} = \sqrt{\frac{2L}{eE}\epsilon_k} \tag{3.9}$$

where equation 3.4, 3.7 and 3.8 have been used. It should be noted that μ and D/μ (or ϵ_k) are the experimentally observed quantities in these studies, not D itself.

A notation one often encounters is: $\sigma = \sigma_{ol}\sqrt{L}$, which can be understood from equation 3.9. In the literature σ_{ol} is sometimes called the diffusion coefficient as well. We distinguish between a longitudinal diffusion coefficient σ_{ol} and a transverse diffusion coefficient σ_{ot}. Note the difference in units: D [m²/s] and σ_{ol} [m$^{\frac{1}{2}}$].

3.3 A simplified theory of electron drift in gases

In this section a simplified theory of electron drift in gases will be presented in a form as it was developed by Palladino and Sadoulet [35, 36]. The prize for its simplicity is that it is only valid in a limited region of field strength. Their simplifying assumptions are:

1. The change in between collisions of the random velocity caused by the electric field is small ($\frac{\Delta v}{v} \ll 1$).

2. The electron energy is high enough compared to $\frac{3}{2}kT$ to allow all temperature effects to be neglected.

3. The cross section for electron molecule scattering is isotropic.

3.3.1 The drift velocity

Consider an electron with charge e, mass m at position $\vec{r} = (x, y, z)$ and with velocity $\vec{v} = (v_x, v_y, v_z)$ which is moving in a gas in the presence of an electric field $\vec{E}$ along the x direction. Suppose that the electron had a collision with a gas molecule at time $t = 0$ and that it emerged at an angle θ_0 with the field direction and with the velocity v_0. Then:

$$x = \frac{1}{2}\frac{eE}{m}t^2 + v_0 \cos\theta_0 t \tag{3.10}$$

$$v_x = \frac{eE}{m}t + v_0 \cos\theta_0 \tag{3.11}$$

$$v_y^2 + v_z^2 = v_0^2 \sin^2\theta_0 \tag{3.12}$$

The path s of the electron as a function of time can be found by solving the equation:

$$(\frac{ds}{dt})^2 = v_x^2 + v_y^2 + v_z^2 \tag{3.13}$$

Using 3.11 and 3.12 results in:

$$(\frac{ds}{dt})^2 = v_0^2 + 2\frac{eE}{m}v_0 t \cos\theta_0 + (\frac{eEt}{m})^2 \tag{3.14}$$

Using the assumption that the change in the drift velocity is small, i.e. $eEt/m \ll v_0$, the second term in 3.14 is small compared to the first one and the third term can be neglected. After expanding the resulting expression in a Taylor series and integration one finds:

$$s(t) = v_0 t (1 + \frac{eEt}{2mv_0}\cos\theta_0) \tag{3.15}$$

$$t(s) = \frac{s}{v_0}(1 - \frac{eE}{2mv_0}\cos\theta_0 \frac{s}{v_0}) \tag{3.16}$$

$$v(s) = v_0(1 + \frac{eE}{mv_0}\cos\theta_0 \frac{s}{v_0}) \tag{3.17}$$

If the mean free path $l(v)$ is defined as the mean distance an electron travels between two collisions and $\tau(v)$ as the mean time between collisions, then:

$$\tau(v) = \frac{l(v)}{v} \tag{3.18}$$

If now $g(s)$ is the probability for a collision per unit path length, then the probability of a collision between s and $s + ds$ is:

$$g(s)ds = \frac{ds}{l(s)} \exp\left[-\int_0^s \frac{ds'}{l(s')}\right] \tag{3.19}$$

where the exponential term gives the fraction of electrons that reach s and $ds/l(s)$ is the fraction of the remaining electrons that collide between s and $s + ds$. Equation 3.17 enables us to express l as a function of the velocity v or of the path s. Expanding $[l(v)]^{-1}$ and the exponential factor around v_0, where again terms of second order and higher are neglected, one arrives at $(l_0 = l(v_0))$:

$$g(s)ds = \left[\frac{1}{l_0} - \frac{eE}{mv_0}\cos\theta_0\frac{dl}{dv}\left(\frac{s}{l_0^2} - \frac{s^2}{2l_0^3}\right)\right]\exp\frac{-s}{l_0}ds \tag{3.20}$$

The mean path between collisions in the direction of the field is:

$$< x > = \int_0^\infty x g(s)ds \tag{3.21}$$

Using 3.10, 3.20 and 3.16 and taking the average over $\cos\theta_0$, one finds:

$$< x > = \frac{2}{3}\frac{eE}{m}\frac{l_0^2}{v_0^2} + \frac{1}{3}\frac{eE}{m}\frac{l_0}{v_0}\frac{dl}{dv}\Big|_{v=v_0} \tag{3.22}$$

Since $< x > = w\tau = wl_0/v_0$ we obtain for the drift velocity:

$$w = \frac{2}{3}\frac{eE}{m}\frac{l_0}{v_0} + \frac{1}{3}\frac{eE}{m}\frac{dl}{dv}\Big|_{v=v_0} \tag{3.23}$$

This would be the drift velocity if all electrons had the same energy. Normally this is not the case and thus:

$$w = \frac{2}{3}\frac{eE}{m}< \frac{l}{v} > + \frac{1}{3}\frac{eE}{m}< \frac{dl}{dv} > \tag{3.24}$$

where the averages are taken over the energy distribution of the electrons.

3.3.2   Diffusion

To calculate the diffusion coefficient D we start from equation 3.10. Taking the square of this equation, neglecting higher order terms, one finds after integration over θ_0:

$$\frac{d < x^2 >}{dt} = \frac{2}{3}v_0^2 t \tag{3.25}$$

If the average is taken over time and equation 3.7 and 3.18 are substituted one finds for the diffusion coefficient:

$$D = \frac{<lv>}{3} \qquad (3.26)$$

where again the average is taken over the energy distribution.

3.3.3   Energy conservation

Suppose the case of a narrow energy distribution. Then the mean free path l is independent of the velocity and the second term in equation 3.24 is zero. The energy loss per second is $\Lambda\epsilon/\tau = \Lambda\epsilon v/l$. As before Λ is the mean fractional energy loss per collision but now due to elastic *and* inelastic electron molecule collisions. After reaching a constant drift velocity the energy gained by the field is on average equal to the energy lost in collisions:

$$eEw = \frac{\Lambda\epsilon v}{l} \qquad (3.27)$$

This equation expresses v as a function of w and can be substituted in the equations derived above. This results in the following expressions for the drift velocity, diffusion coefficient, random velocity, mean energy and critical energy:

$$w = \frac{1}{3}\sqrt{2\sqrt{3\Lambda}\frac{eEl}{m}} \qquad (3.28)$$

$$D = \frac{1}{3}\sqrt{2\sqrt{\frac{1}{3\Lambda}}\frac{eEl^3}{m}} \qquad (3.29)$$

$$v = \sqrt{2\sqrt{\frac{1}{3\Lambda}}\frac{eEl}{m}} \qquad (3.30)$$

$$<\epsilon> = \sqrt{\frac{1}{3\Lambda}eEl} \qquad (3.31)$$

$$<\epsilon_k> = <\epsilon> \qquad (3.32)$$

The numerical factors in these formulas depend on the assumptions made and should be seen as approximations only.

The ratio between the drift velocity and the random velocity is $w/v = \sqrt{\Lambda/3}$. If elastic collisions dominate this ratio is small confirming what was stated in section 3.2.

If the mean fractional energy loss is small, it follows that the mean electron energy and random velocity are high. The drift velocity is then small whereas the diffusion is large. This is called a 'hot' gas. Examples of such gases are pure noble gases at low field (no ionization).

If the mean fractional energy loss is high the opposite will occur. The drift velocity is high and the diffusion small. This is called a 'cool' gas. A well known example is CO_2 for which the mean electron energy remains thermal in fields up till ≈ 1 kV/cm and thus the diffusion is the smallest possible.
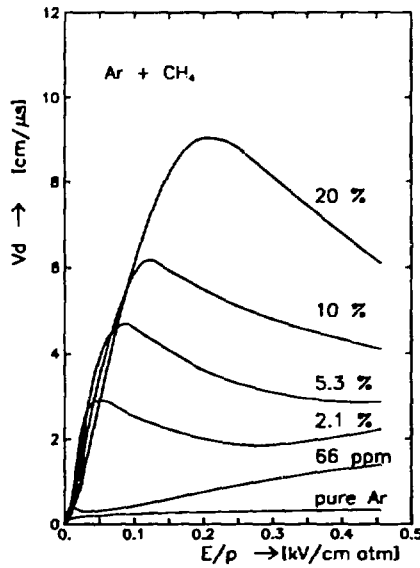

Figure 3.2: The drift velocity in several argon-methane mixtures versus the reduced electrical field; the methane percentages are indicated [25, 26].

Using the above formulas we can explain the increase in drift velocity when a small amount of a poly-atomic gas (CH_4, C_2H_6, CO_2) is added to a noble gas. This is illustrated in fig. 3.2. Since the concentration of the additive is low, the mean free path l is hardly changed but due to rotational and vibrational excitation the mean fractional energy loss Λ will increase substantially.

As a consequence of our assumptions the drift velocity and diffusion are proportional to $\sqrt{E}$. This appears not to be in accordance with experimental results at low field strengths, where the drift velocity is observed to be proportional to E (and the mobility is constant). The simple formulas derived above should be applied with caution.

3.4   The classical theory of electrons in gases

If the cross sections for elastic and inelastic collisions and ionization are known accurately it is possible with a good theory of electron drift in gases to calculate all drift properties.

Because of the many assumptions, the theory presented in section 3.3 is approximative only. An almost exact theory was derived by Palladino and Sadoulet [35, 36]. With this theory they, as well as several other authors ([29]-[33]), were able to describe the behaviour of some drift gases accurately. The only assumption they made is the independence of the energy distribution on the position in the cloud. About the time they formulated their theory it was realized that the diffusion in the direction of the field (longitudinal diffusion coefficient: D_l) is different from that perpendicular to the field (transverse diffusion coefficient: D_t) [34]. It is just the above mentioned assumption that has to be dropped to find two different diffusion coefficients. This was done by Parker and Lowke [27, 28] and will be discussed here.

Starting point is the electron energy distribution function $f(\vec{r}, \epsilon, t)$ which denotes the density of electrons at position $\vec{r}$ with energy ϵ at time t. This function has to fulfil the Boltzmann transport equation which is an equation of continuity in position and energy space. They showed that a cloud of drifting electrons can be described by:

$$f(\vec{r}, \epsilon, t) = (F_0 + F_1 \frac{\partial}{\partial z} + F_2 \frac{\partial^2}{\partial z^2} + \ldots) \frac{\exp(\frac{-(z-wt)^2}{4D_l t})}{\sqrt{4\pi D_l t}} \frac{\exp(\frac{-(x^2+y^2)}{4D_t t})}{4\pi D_t t} \quad (3.33)$$

The functions F_i are obtained by solving the appropriate form of the transport equation. In general this can only be done numerically. The transport coefficients are given by the following integrals:

$$w = -\frac{8\pi eE}{3m^2 n} \int_0^\infty \frac{\epsilon}{\sigma_m} \frac{\partial F_0}{\partial \epsilon} d\epsilon \quad (3.34)$$

$$D_t = \frac{8\pi}{3nm^2} \int_0^\infty \frac{\epsilon F_0}{\sigma_m} d\epsilon \quad (3.35)$$

$$D_l = D_t + \frac{8\pi eE}{3m^2 n} \int_0^\infty \frac{\epsilon}{\sigma_m} \frac{\partial F_1}{\partial \epsilon} d\epsilon + \frac{4\pi w}{m} \sqrt{\frac{2}{m}} \int_0^\infty \sqrt{\epsilon} F_1 d\epsilon \quad (3.36)$$

As before n is the gas concentration and σ_m is the cross section for elastic scattering (also called the momentum transfer cross section).

The calculations can be extended to gas mixtures by using the relation:

$$\sigma_m = \sum_i \delta_i \sigma_{mi} \quad (3.37)$$

where δ_i is the percentage of the ith gas in the mixture ($\sum_i \delta_i = 1$).

The theory is applied in the following way. The functions F_i can be calculated if the cross sections are known and from them the drift properties can be calculated. Since the cross sections are often not known accurately enough, measurements of transport coefficients in pure gases are used to adapt a model of the cross sections. These results are then used to predict gas properties of mixtures. This has been done by several groups. Some examples can be found in [37]-[40].
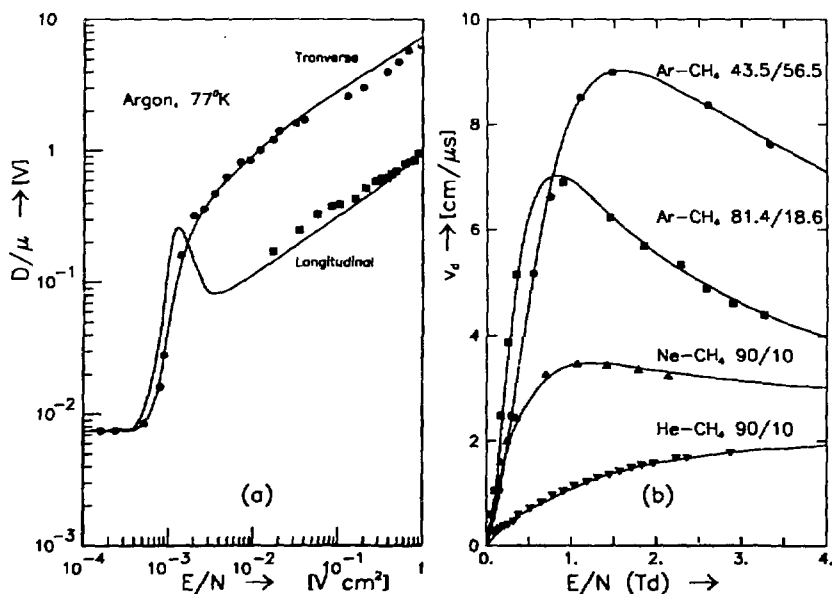
Figure 3.3: Comparison of calculations with experimental data: (a) diffusion coefficients for argon at 77° K [28]; (b) drift velocities in methane-noble gas mixtures [39].

Two applications of the theory will be discussed. The first is from Lowke and Parker [28]. In figure 3.3a they compare measurements of the transverse and longitudinal diffusion coefficients of argon with the results of their calculations. As input they used the momentum transfer cross section derived by Engelhardt and Phelps [30]. Argon is known for its large difference between the two diffusion coefficients. The ratio D_l/D_t can become as large as 7.

In figure 3.3b a comparison is made between calculated and measured drift velocities in methane-noble gas mixtures [39]. The cross sections were determined using measurements of the transport coefficients of the pure gases that make up the mixture. It should be noted that none of the measurements displayed was used to fix the parameters of the cross section, making the comparison a fair check of the accuracy of predictions that can be made using the theory presented above with good cross sections as input. From the figure it is also clear that relation 3.28 has barely any validity in this case.

3.5 Electron drift in a magnetic field

The path of a drifting electron with charge e and velocity $\vec{v}$ in the presence of an electric field $\vec{E}$ and a magnetic field $\vec{B}$ is determined by the sum of the Coulomb force and the

Lorentz force:

$$\vec{F} = e(\vec{E} + \vec{v} \times \vec{B}) \tag{3.38}$$

For the model presented in section 3.3 this means that the dynamical equation 3.10 has to be extended. In the case of an electric field along the x direction and a magnetic field along the z direction the dynamical equations are:

$$\frac{d^2x}{dt^2} = \frac{eE}{m} + \frac{eB}{m}\frac{dy}{dt} \tag{3.39}$$

$$\frac{d^2y}{dt^2} = -\frac{eB}{m}\frac{dx}{dt} \tag{3.40}$$

$$\frac{d^2z}{dt^2} = 0 \tag{3.41}$$

The solution of these equations is analogous to that presented in section 3.3.1. Here only the results are presented:

$$w_x = \frac{2}{3}\frac{eE}{m} < \frac{l/v}{1+\omega^2l^2/v^2} > + \frac{1}{3}\frac{eE}{m} < \frac{1}{1+\omega^2l^2/v^2}\frac{dl}{dv} > \tag{3.42}$$

$$w_y = -\frac{1}{3}\frac{eE\omega}{m} < \frac{l^2/v^2}{1+\omega^2l^2/v^2} > - \frac{2}{3}\frac{eE\omega}{m} < \frac{l/v}{1+\omega^2l^2/v^2}\frac{dl}{dv} > \tag{3.43}$$

$$D_l = \frac{1}{3} < lv > \tag{3.44}$$

$$D_t = \frac{1}{3} < \frac{lv}{1+\omega^2l^2/v^2} > \tag{3.45}$$

The averages have to be taken over the energy distribution of the electrons. The cyclotron frequency $\omega = eB/m$ has been used in the equations. The drift velocity in the direction of the electric field is reduced by the factor $1 + \omega^2l^2/v^2$. The magnetic field causes the drift velocity to develop a component in the y direction. The angle between the drift direction with and without magnetic field is called the Lorentz angle α_l:

$$\tan \alpha_l = \frac{|w_y|}{|w_x|} \tag{3.46}$$

The diffusion in the presence of a magnetic field is described by two diffusion coefficients. In the direction along the magnetic field the diffusion coefficient D_l is not influenced by the magnetic field whereas in the transverse direction the diffusion coefficient D_t is reduced. This reduction stems from the fact that an electron moving with constant velocity in a magnetic field describes a spiral with the axis along the direction of the magnetic field. Any net displacement perpendicular to this direction is thus limited.

In examples illustrating the behaviour of electrons drifting in a magnetic field one often uses the simplifying assumption: $l/v = \tau$ =constant. The drift velocity in the absence of a magnetic field is then:

$$w = \frac{eE}{m}\tau \tag{3.47}$$

which means for the electron mobility:

$$\mu = \frac{e}{m}\tau \tag{3.48}$$

In the presence of a magnetic field we find for the drift velocity:

$$w_x = \frac{1}{1 + \omega^2\tau^2}\mu E \tag{3.49}$$

$$w_y = -\frac{\omega\tau}{1 + \omega^2\tau^2}\mu E \tag{3.50}$$

Here $\omega\tau$ can be interpreted as the number of spiral turns a drifting electron makes during the mean drift time τ between two collisions. Using the above equations one finds for the Lorentz angle:

$$\tan\alpha_l = \omega\tau \tag{3.51}$$

A more general expression for the drift velocity, independent of the direction of the electric and magnetic field, is [41]:

$$\vec{w} = \frac{\mu}{1 + \omega^2\tau^2}[\vec{E} + \mu(\vec{E} \times \vec{B}) + \mu^2(\vec{E} \cdot \vec{B})\vec{B}] \tag{3.52}$$

In the drift tubes of the DELPHI barrel RICH the magnetic field is parallel to the electric field. Thus neither the drift velocity nor the longitudinal diffusion are affected by the magnetic field. The transverse diffusion is however reduced by a factor $1 + \omega^2\tau^2$, which improves the resolution of the detector.

3.6 The gas multiplication process

In the previous sections the theory of electron drift in gases was discussed for conditions in which the electron energy is too low to ionize the drift gas molecules. The ionization potential for these gases is typically between 10 and 15 eV. In high electric fields (> 5 kV) the mean electron energy can increase substantially, making the probability for ionization non-negligible.

A mean free path for ionization λ_i can be defined as being the average distance an electron travels against the direction of the field before being involved in an ionizing collision. One often uses the inverse of the mean free path, also called the first Townsend coefficient α, which represents the number of ions produced per unit length of electron drift.

The process of ionization is the basis of avalanche multiplication in wire chambers. A free electron in a uniform electric field travels on average a distance λ_i before causing an ionization and thus generating a second free electron. After gaining enough energy both electrons will create a new free electron, making a total of four, etc. By this mechanism

high gains up to $10^4 - 10^6$ can be obtained. The multiplication factor M as a function of the drift distance x is given by:

$$M = e^{\alpha x} \tag{3.53}$$

In a wire chamber the avalanche amplification process occurs close to the sense wire, in a region where the field is high and far from uniform. If the amplification starts at a distance r_c from the centre of a wire with radius a, equation 3.53 has to be rewritten:

$$M = e^{\int_a^{r_c} \alpha(r) dr} \tag{3.54}$$

It is thus possible to calculate the multiplication factor in a wire chamber if the dependence of the first Townsend coefficient on the field is known. Assuming an approximate dependence Sauli [23] arrives at an expression for M that for moderate gains is in good agreement with experimental data.

The multiplication factor M will show a distribution with a certain variance caused by statistical fluctuations, especially caused in the first amplification steps. In the situation where an avalanche is initiated by many (primary) electrons the average spread in the multiplication is small. If the avalanche is started by one electron only the variance can be considerable. Alkhazov [42] showed that in the non-uniform fields of multi wire proportional chambers the shape of the avalanche size distribution should be close to a Polya distribution:

$$P(q) = \frac{b^b}{\bar{q}\Gamma(b)}(\frac{q}{\bar{q}})^{b-1} \exp(-b\frac{q}{\bar{q}}) \tag{3.55}$$

with $\bar{q}$ as the mean of the charge distribution and b as a shape defining parameter. In fig. 3.4 the distribution is shown for 4 different values of b. For $b = 1$ the distribution is an exponential one. By preference the value of b is as high as possible. Values for the b parameter varying between 1.5 and 2.5 can be found in the literature [43, 44].

3.7   Electron attachment in gases

3.7.1   Introduction

Drifting electrons experience several types of interactions on the atomic or molecular level, like elastic and inelastic scattering and ionization. In this section electron attachment is discussed. This is the process in which an electron is attached to an atom or a molecule in a collision. The free electron is lost and an ion is formed. This process happens only when the negative ion has a lower potential energy than the neutral atom or molecule. The energy difference between the two states is known as the electron affinity. It is defined as positive when energy is emitted on attachment. Gases with large electron affinities are oxygen (0.45 eV), halogens ($\approx$3 eV) and various hydrocarbons [45]. The gases used in drift chambers normally hardly give rise to electron attachment but they can contain impurities
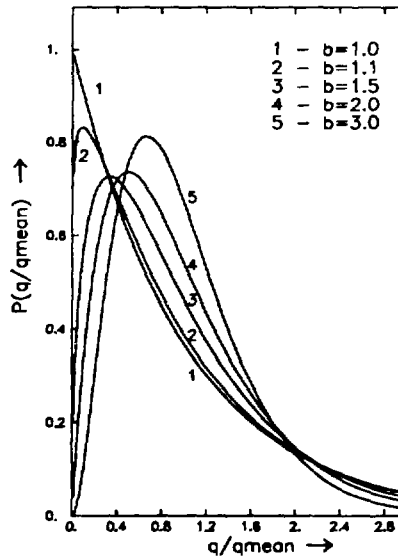
Figure 3.4: Polya distribution for different values of the parameter b.

that have positive electron affinity (or are said to be electronegative) like oxygen and water. A model for the process of electron attachment is presented in section 3.7.2.

Due to attachment the number of electrons $n(x)$ after a drift distance x will decrease:

$$n(x) = n(0) \exp(-\frac{x}{\lambda}) \tag{3.56}$$

where λ is the attenuation length. The electron loss can be parameterized as a function of the drift time in two ways:

$$n(t) = n(0) \exp(-\frac{t}{\tau}) = n(0) \exp(-At) \tag{3.57}$$

where τ is called the attenuation time and A the attachment rate. Obviously:

$$\lambda = w\tau = \frac{w}{A} \tag{3.58}$$

In contrast to drift chambers were electronegative impurities are unwanted, a few percents of an electronegative gas is sometimes added to gas mixtures used in wire chambers, to improve the stability of the chamber at high gains [23].

3.7.2   Three body attachment process with oxygen

Under typical conditions in drift chambers the electron energy distribution has a mean value around 1 eV or less. Consequently dissociation as a means of electron attachment

can be neglected. A good description of the attachment process under these conditions is given by the Bloch-Bradbury-Herzenberg model [46, 47]. Oxygen will be used as an example since it is the most important impurity in drift gases. In the BBH model the attachment is described by a two step process. In the first step the electron is attached to oxygen and a negative excited ion is formed:

$$O_2 + e^- \rightarrow O_2^{-*} \tag{3.59}$$

For the second step several possibilities exist. Huk et al. [48] showed that for low oxygen concentration and at atmospheric pressure the dominant second step leading to electron loss is:

$$O_2^{-*} + M \rightarrow O_2^- + M^* \tag{3.60}$$

where M is a molecule of the drift gas. This means that the electron loss is a three body process.

The BBH model predicts the following relation for the attachment rate A:

$$A = C_{O_2,M} \cdot n_{O_2} \cdot n_M \tag{3.61}$$

where n_{O_2} and n_M are the respective concentrations of oxygen and the drift gas; $C_{O_2,M}$ is the attachment coefficient. Huk et al. [48] proved that the attachment rate can be described this way by showing that $C_{O_2,M}$ is independent of both concentrations. A further

gas	$C_{O_2,M}$ $[10^{-30}cm^6s^{-1}]$	τ ($n_{O_2}=1$ppm) $[\mu s]$	λ ($n_{O_2}=1$ppm) $[m]$	$n_{O_2}(\lambda=10$ m$)$ $[ppm]$
He	0.05	$2.8 \cdot 10^4$	$14 \cdot 10^2$	140
Ne	0.023	$6.0 \cdot 10^4$	$30 \cdot 10^2$	300
Ar	0.05	$2.8 \cdot 10^4$	$14 \cdot 10^2$	140
Kr	0.05	$2.8 \cdot 10^4$	$14 \cdot 10^2$	140
Xe	0.085	$1.6 \cdot 10^4$	$8 \cdot 10^2$	80
O_2	2.2			
CH_4	0.34	$4.1 \cdot 10^3$	210	21
C_2H_6	1.5	$9.2 \cdot 10^2$	46	4.6
$n\text{-}C_4H_{10}$	4.2	$3.1 \cdot 10^2$	16	1.6
CO_2	3.2	$4.3 \cdot 10^2$	22	2.2
H_2O	14.5			

Table 3.1: Three body attachment coefficients $C_{O_2,M}$ for the relation $e^- + O_2 + M \rightarrow O_2^- + M^*$ at thermal energies [49]; the lifetime τ of an electron when the O_2 concentration is 1 ppm; the corresponding attenuation length λ (using $w = 5cm/\mu s$) and the maximum allowed O_2 concentration corresponding to $\lambda = 10$ m.

conformation of the BBH model was their experimental observation of the predicted inverse proportional dependence of the attachment on the mean electron energy.

In table 3.1 experimental values of the three body attachment coefficient are given for several drift gases, oxygen and water [49]. For the same table, with equation 3.61, the lifetime τ for a drifting electrons has been calculated for an oxygen concentration of 1 ppm. To calculate the corresponding attenuation length λ a drift velocity of 5 cm/μs has been used. For our application in the DELPHI barrel RICH we require a minimal attenuation length of 10 m. The last column indicates the maximal oxygen concentration allowed by this requirement.

It has to be emphasized that the values in able 3.1 can only be taken as indications. The measurements were done with thermal electrons and the drift velocity used in the calculation is just a typical value. It can be concluded however that the more complex the molecule the larger the three body cross section and that electrons hardly attach to noble gases.
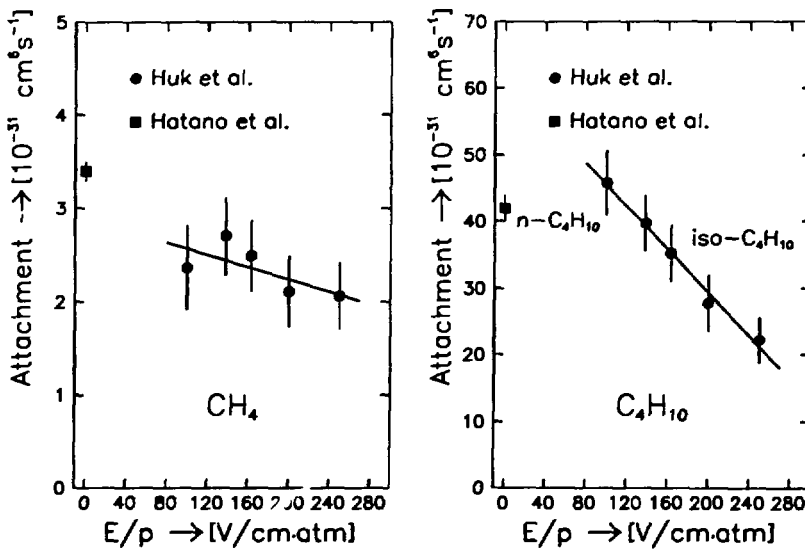

Figure 3.5: Three body attachment coefficient $C_{O_2,M}$ as a function of the reduced electric field for methane and butane. The data is taken from Huk *et al.*[48] and Hatano *et al.*[49]

The three body attachment coefficients of methane and isobutane measured by Huk et al. [48] as a function of the reduced field (E/p) are presented in figure 3.5a and 3.5b. The thermal data from table 3.1 are also shown (E/p = 0). If we take an extrapolated value for methane in higher fields of $2.0 \cdot 10^{-31}$ cm^{6}s^{-1}, then the constraint on the oxygen concentration in pure methane to achieve an attenuation length of 10 m is relaxed from

the 21 ppm in table 3.1 to 36 ppm. Under the assumption of a constant ratio between the attachment for methane and ethane as a function of the reduced field, the same constraint in pure ethane shifts from 4.6 ppm to 8 ppm.

3.7.3   Cross section for attachment

If we define a cross section for attachment $\sigma_a(v)$, then the probability per second for an electron with velocity v to be attached is $n_a \sigma_a v$ where n_a is the density of the considered molecule. The effective cross section for attachment is now defined as [50]:

$$\sigma_{a,eff} = \frac{\int_0^\infty f(\vec{v})\sigma(v)v d\vec{v}}{\int_0^\infty f(\vec{v})v d\vec{v}} \tag{3.62}$$

where $f(\vec{v})$ is the electron velocity distribution. We then find for the electron loss: $dn = n(t) \cdot n_a \cdot \sigma_{a,eff} \cdot < v >$. Integration gives the expected exponential electron loss from equation 3.57 with:

$$A = n_a < v > \sigma_{a,eff} \tag{3.63}$$

Comparison of equation 3.63 with 3.61 shows that the attachment cross section of oxygen depends on the gas composition and on the pressure. Nevertheless attachment is sometimes expressed as a cross section and then equation 3.63 has to be used.

Inserting equation 3.63 in equation 3.58 gives:

$$\lambda = \frac{w}{n_a < v > \sigma_{a,eff}} \tag{3.64}$$

Chapter 4

The DELPHI barrel RICH detector

4.1   Introduction

At the time when the DELPHI letter of intent was submitted (1982) the technique of Ring Imaging CHerenkov (RICH) counters was still in development. It was decided to built a prototype to study the feasibility and the performance of a big RICH system. The knowledge and experience from this work [19], combined with results from smaller and more specific test set-ups led to the design of the final barrel RICH (BRICH) [51].

The BRICH consists of two identical halves, each segmented azimuthally in sections of 15°. Each section contains a liquid radiator, a gaseous radiator volume, a drift tube with a wire chamber at its end and 6 mirrors (figure 4.1).

The BRICH is the most complicated and delicate component of the DELPHI detector. The main constraints for its design are:

- Though the thickness of the BRICH in terms of radiation lengths has to be as small as possible, the detector has to be mechanically rigid. Not only because of the detection accuracy of the BRICH itself but also since the TPC and outer detector are mounted on it.

- As a consequence of the use of C_5F_{12} as gaseous radiator the volume of the BRICH has to be heated to about 40°C. The outside has to be cooled since it is undesirable to radiate heat to other detectors in DELPHI.

- The BRICH will be operated at an overpressure of 0.3 bar.

- The detector was designed to have an electric field in the drift tubes up to 1 kV/cm giving a total high voltage on the mid-wall of -150 kV. This requires a good electrical isolation and demands great care to avoid corona.

- The drift field in the tubes has to be extremely homogeneous. To achieve this a frame is placed on top of each drift tube with wires and strips. Analogous electrodes are found on the liquid radiator and the inner cylinder.

- The vessel has to be leak tight to avoid air pollution in the gaseous radiator which would deteriorate the UV transparancy.
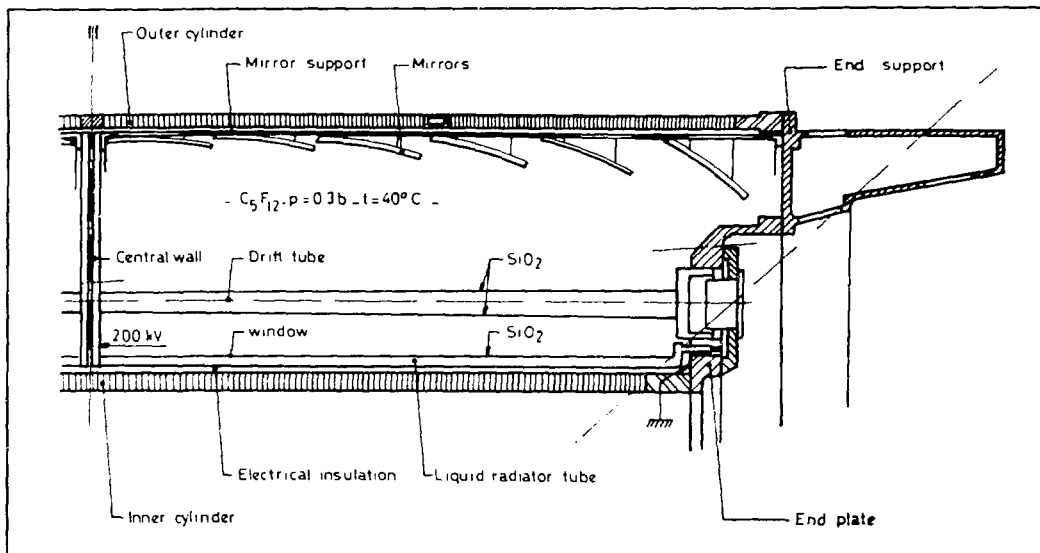
Figure 4.1: Longitudinal view of a quarter of the barrel RICH; the wire frame just above the drift tube is not shown.

- The drift tubes have to be extremely leak tight since the maximum allowed concentration of radiator gas inside the drift tubes is 0.2 ppm [52].

- The detector is only sensitive to a limited wavelength region of the Čerenkov light (165 - 200 nm). All losses in this region have to be minimized.

4.2   Global description of the operation

We recall from chapter 2 that a charged particle, crossing a medium with a velocity higher than the velocity of light in that medium, gives rise to Čerenkov light. The light is emitted under an angle θ_c with the particle track, azimuthally around the track. If the medium is thin we can speak of a "cone" of Čerenkov light.

The BRICH (figure 4.1) contains two types of radiators. The light of both of these is detected in the same drift tubes. The Čerenkov photons created in the liquid radiator (1 cm C_6F_{14}) reach the drift tubes directly on one side (proximity focussing). The gaseous radiator consists of 39 cm C_5F_{12}. The light created there is focussed with parabolic mirrors onto the drift tubes from the opposite side.

The drift tubes are constructed entirely from quartz plates. Small strips on the quartz gradate the potential and thus define an electric field inside the drift tubes. A gas mixture of methane, ethane and TMAE vapour (0.1%) is flushed through the drift tubes. The

TMAE acts as a photo-converter. The photo-electrons drift in the electric field towards a wire chamber were they are detected. The wire chamber has a two dimensional readout. Combined with the drift time a three dimensional reconstruction of all photo-conversion points is obtained. This enables us to reconstruct the interception of a Čerenkov cone with the drift tubes, and thus to determine the Čerenkov angle. Since the position of the track and the momentum of the particle are known accurately from other detectors in DELPHI, in practice one determines from these data the likelihood of the particle being an electron, muon, pion, kaon or proton.

4.3 Description of the BRICH components

4.3.1 The vessel

The vessel consists of the inner cylinder, the outer cylinder and two flanges. They are mounted together carefully with O-rings to guarantee leak tightness. The BRICH is mounted inside DELPHI with a support on the magnet coil. The outer detector chambers and the TPC are mounted on the BRICH. With all these accurate position measuring devices connected to it, it is clear that the vessel has to be mechanically stiff. In fact the flanges are the really rigid parts. The inner and outer cylinder keep the two flanges properly positioned with respect to each other.

The inner cylinder

The inner cylinder (diameter 2.60 m, length 2.10 m) has to resist the overpressure in the detector (0.3 bar) and to insulate the high voltage (up to 150 kV). The mechanical task is accomplished by a wall consisting of two skins of 1 mm thick aluminium sheets with 43 mm of aluminium honeycomb sandwiched in between. An insulating layer is fixed on the outside (i.e. RICH side) of this cylindrical wall. The insulator is made from helically wound layers of mylar foils (20 cm wide, 75μm thick) glued together with polyurethane glue. The winding pitch is such that a small gap is left between adjacent turns. Since the resistivity of mylar ($\geq 2\times10^{18}$ Ohm·cm) is much higher than that of the glue (3×10^{13} Ohm·cm) [53], a small current will only flow through the latter, resulting in a controlled potential degradation inside the insulator. The construction is optimized to make the path for the current as long as possible. From the total insulator thickness of 15 mm one calculates an expected lifetime of over 80 years at an operating voltage of -150 kV [54]. The same construction technique was used for the ALEPH TPC.

Kapton foils with copper strips (width 3 mm, pitch 6 mm) on both sides are glued onto the insulator as a top layer. The strips on the foil serve to degrade the voltage from the -150 kV at the centre of the cylinder to ≈0 V at the end flanges. A resistor bar mounted

on top of the kapton foils, is connected to all the copper strips.

During the mounting of the resistor bar an accident happened in which the kapton foil and partly the mylar insulator was cut. Though a reparation was carried out the life time of the insulator is probably strongly reduced. It has been decided to lower the working voltage of the BRICH initially to -80 kV instead of -150 kV as a measure of safety.

On the inside of the inner cylinder (and thus at the outside of the BRICH) the following layers are mounted:

- Two layers of polyester foil to insulate the wall electrically from the heating circuits.
- Four helically wound heating circuits.
- Again two layers of polyester foil.
- A thermal insulation consisting of 12 mm Rohacell.
- Metal tubes for water cooling.
- A protective skin consisting of 1 mm thick aluminium.

The outer cylinder

The outer cylinder has a diameter of 3.85 m and a length of 3.55 m. It consists of a sandwich of 30 mm aluminium honeycomb between sheets of 1 mm thick aluminium. Like for the inner cylinder, heating circuits, thermal insulation and a cooling circuit are mounted on the outside.

The flanges

The flanges constitute the mechanical reference and main support for the BRICH on which are fixed: the mirror cages, the drift tubes with the wire chambers and the liquid radiator tubes. In fact each flange consists of two parts, the end support and the end plate (figure 4.1). The flanges are made of aluminium. Heating circuits are glued on the exterior.

4.3.2   The mirrors

Every 15° section of the BRICH contains 6 paraboloidal mirrors, making a total of 6x24x2 = 288 mirrors. All mirrors in one section have different focal lengths.

The mirrors have been produced industrially from 6 mm thick glass blanks, using a specially developed slumping technique, followed by vacuum deposition of a 50 nm thick layer of Al and a 60 nm thick protective layer of MgF_2 [55]. The required reflectivity was 80% in the wavelength range 165-200 nm. In figure 4.7 the average reflectivity for all mirrors is shown, which is better than the requirement. No mirrors had to be rejected
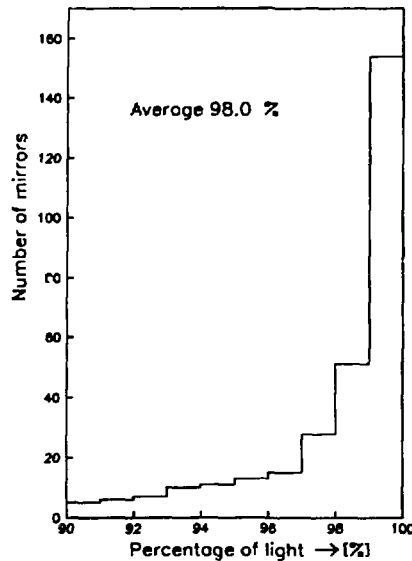
because of bad reflectivity.

Figure 4.2: The number of mirrors that have over 90% of parallel light focused in an area of 1.2 mm diameter.

Another requirement was that a parallel light beam, covering the whole mirror, should be focussed for at least 90% in a circular area of 1.2 mm diameter. In figure 4.2 the distribution of this percentage is given. The average is 98%. Nevertheless several mirrors had to be rejected.

The mirrors are mounted on the mirror cages, two stiff mechanical structures (one for each half of the BRICH) that are mounted on the flanges and carry the mid-wall.

4.3.3   The liquid radiator

The liquid radiator containers (length 150 cm, width 34 cm, internal height 1 cm) consists of trays constructed from composite material, closed by 4 mm thick quartz windows. The thermal expansion coefficient of the container matches that of the quartz. Small columns are glued between the container and the quartz to ensure resistance to pressure differences between inner and outer volume. Kapton foils with strips (pitch 6 mm) are glued on opaque parts of the containers. Conductive strips (200 μm wide; pitch 6 mm) are deposited on the quartz windows. Before installation pairs of containers are combined and equipped with a double resistor chain. The radiating medium is a 1 cm thick layer of C_6F_{14}. The index of refraction n is 1.28.

4.3.4   The gaseous radiator

The whole vessel is filled with the gaseous radiator. The Čerenkov light emitted between the drift tubes and the mirrors is focussed onto the drift tubes. The light that is emitted between the liquid radiators and the drift tubes is considered as background, as is the Čerenkov light emitted in the several layers of quartz.

The minimal path of a particle in the gas layer is 39 cm. The gas used, C_5F_{12} (n=1.002275 at 1.3 bar) has a boiling temperature of 30°C thus entailing the need of heating the whole BRICH to about 40°C.

4.3.5   The drift tubes

The BRICH contains a total of 48 (2x24) drift tubes. Two drift tubes with an end flange and a support structure called *boitier* are glued together to form a so called bitube.

In order to minimize distortions in the paths of the drifting electrons as much as possible it was required that radial field components are 4 orders of magnitude smaller than the longitudinal drift field: $E_t/E_l < 10^{-4}$. To achieve this the following measures had to be taken:

- Deposition of metal strips with a pitch of 3 mm on the inside and the outside of the drift tubes.
- Potential defining strips on the liquid radiator.
- A wire frame on top of each drift tube with potential defining electrodes.
- A linear potential degrader on the mid wall (from bitube to the outer cylinder).

In figure 4.3 the equipotential line distribution in the BRICH is shown. Note that the mirrors have zero potential and that they are in a region of low field which avoids corona on their edges.

Each drift tube is entirely constructed from 4 mm thick quartz plates. The length of the tubes is 155 cm, the width 34.5 cm, the height is 4.0 cm at the HV side and 6.0 cm at the boitier side. The top and bottom walls each consist of 4 quartz plates being glued side to side, while the side walls each consist of 3 plates. Conductive strips are deposited all around each of the quartz plates in a vacuum evaporation set-up. Each strip consists of 3 layers: 20 nm chromium, 200 nm copper and 20 nm chromium. The width of the strips on top and bottom wall is 0.1 mm whereas on the side walls the width is 0.5 mm. The pitch of the strips is 3 mm. After glueing a tube, corresponding strips on the joints are connected with conductive glue. As a result strips at both the inner and outer surface of the tubes form closed loops. Apart from shaping the drift field the strips also reduce the build up of surface charges.
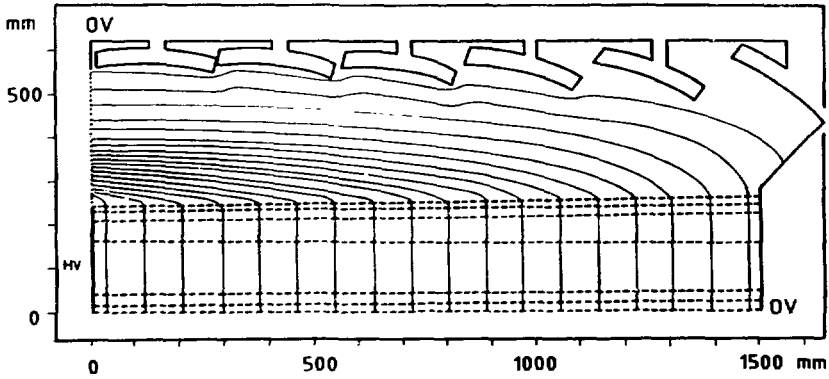
Figure 4.3: Artists view of the equipotential line distribution in the BRICH.
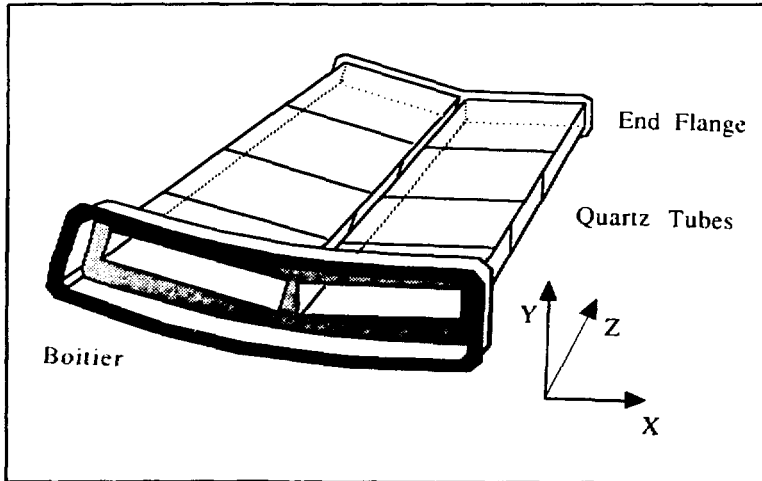

Figure 4.4: Schematic drawing of a bitube.

The end flange supports the drift tubes at the HV side. For each bitube it contains the gas connection from one tube to the other. The boitier supports the drift tubes on the BRICH side and houses the wire chamber. The boitier contains a flexible membrane to avoid mechanical stress in the quartz. It also contains the gas in- and outlet constructed such that the gas flow through the tubes is as uniform as possible. Also the gas connection in the end flange is optimized in this respect. Before installation in the BRICH each assembled bitube was checked carefully for leaks in a leak testing set-up.

Two wire frames are mounted above a bitube with a resistor bar in between. Thus the potentials on the strips of two drift tubes and two wire frames are defined by one resistor

bar. The resistors used are 6 MΩ of 1% accuracy. All resistor chains in the BRICH are doubled as a measure of safety.

In figure 4.4 our coordinate system is shown. It should be compared with the cylindrical coordinates that are more generally used in DELPHI. Our x, y and z coordinates approximately correspond to rϕ, r and z.
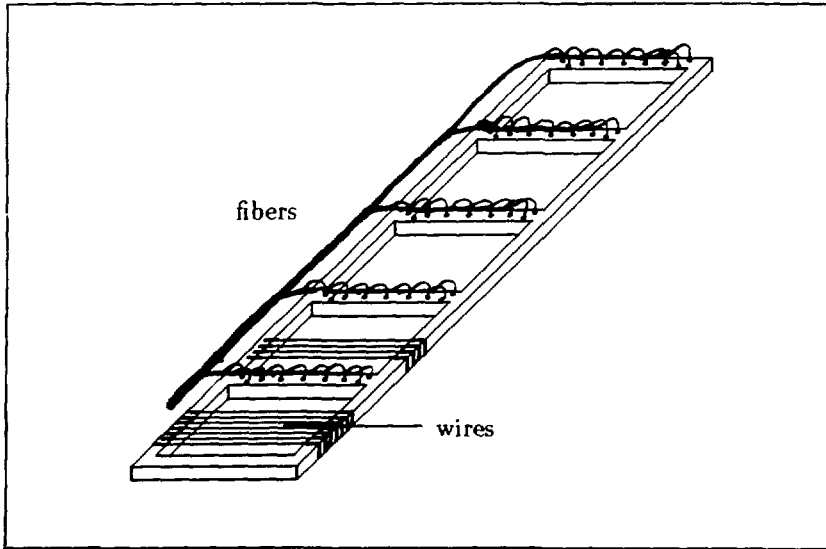

Figure 4.5: Layout of the wire frames and the calibration system.

4.3.6   The wire frames and the calibration system

In figure 4.5 the layout of a wire frame is shown. It is constructed from 10 mm thick stesalit on which kapton foils with copper strips (pitch 6 mm) are glued. The five open spaces are equipped with two layers of wires of 100 μm diameter, one layer at each side of the frame. The wires have a pitch of 6 mm. The distance between the drift tubes and the wire frames is 12.5 mm. Since the mirrors focus the UV light in the open spaces the frames introduce essentially no loss.

The calibration system consists of 5 rows of 9 fibers. The rows are mounted on the bars of the wire frame as indicated in figure 4.5. With the UV light spots created by the fibers we are able to calibrate the drift velocity and the distortions in the electron drift. To achieve an accuracy of 1 mm in the determination of the distortions the spread of the fibers over each row is accentuated on the regions close to the side walls, where the biggest distortions occur.

4.3.7 The gas and fluid system

The functioning of the BRICH depends on two gas systems and a fluid system (drift gas, C_5F_{12}, and C_6F_{14} respectively). The systems are mainly independent of each other, except for the pressure regulation. The pressure difference between drift gas and gaseous radiator is kept at 10 mbar and between liquid radiator and gaseous radiator at 50 mbar. To remain within these pressure tolerances, also in cases of electrical power cut and gas alarms, is one of the intricate parts of the system.

The drift gas, consisting of methane and ethane is thoroughly cleaned before contact with TMAE. The oxygen concentration has to be below 0.4 ppm. Only stainless steel is used for the tubing of the gas system because of its low outgassing. The gas system has to be leak tight down to 10^{-9} mbar/s. To avoid TMAE condensation the tubing is kept at a temperature of 40°C.

On average every 5 hours the volume of the gaseous radiator, C_5F_{12}, is recirculated. In a cleaning system all impurities are taken away. The liquid radiators are recirculated every 4 hours.
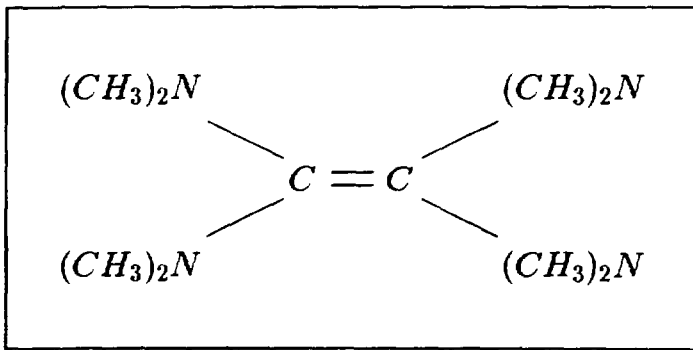

Figure 4.6: The TMAE molecule.

4.4 TMAE

As a photoconverter in the drift gas we use a substance called tetrakis(dimethylamino)-ethylene (TMAE). It is known for its low ionization potential (5.4 eV). The strong electron donor property is due to the presence of the four amino groups with a free electron pair each that partially transfer to the two central carbon atoms (figure 4.6).

The quantum efficiency of the conversion process of UV photons to free electrons is shown in figure 4.7 [7]. Also indicated are the transparancies of quartz, methane, ethane, C_5F_{12} and C_6F_{14} [9]. One concludes that the BRICH is suitable for measuring Čerenkov
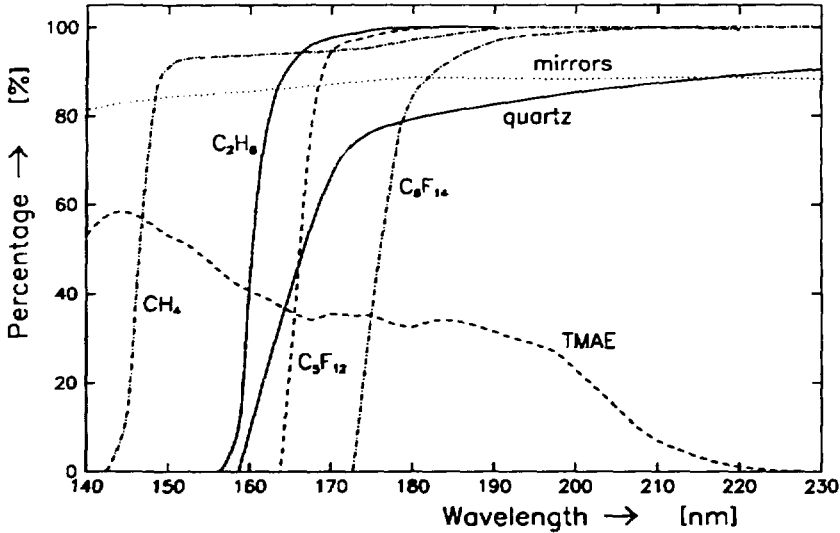
Figure 4.7: As a function of wavelength the following properties are shown: the average reflectivity of the mirrors [55], the TMAE quantum efficiency [7] and the transparancies of several substances [9]. For methane,ethane and C_5F_{12} the absorption was measured in a 10 cm cel; for C_6F_{14} a liquid layer of 1 cm thickness was used; the quartz transparency was measured with a 4 mm thick window.

light from the liquid radiator in the range 173-220 nm (7.1-5.6 eV) and from the gaseous radiator in the range 165-220 nm (7.5-5.6 eV).

At room temperature TMAE is a liquid (freezing point -4°C, boiling point 177°C). The highest concentration achievable in the drift tubes is the vapour pressure corresponding to the temperature of the liquid. The liquid is kept in a bubbler, optimized to obtain good contact between the TMAE and the drift gas that flows through [56]. As a result the TMAE vapour pressure in the gas after the bubbler corresponds to the temperature of the bubbler. The operating temperature of the bubbler is 30°C; the BRICH is kept at 40°C.

In the situation of equilibrium between the liquid and the vapour phase of a substance, the vapour pressure p as a function of the temperature T is given by the Clausius-Clapeyron relation [57]:

$$\frac{d(\ln p)}{d(1/T)} = -\frac{\Delta_e h}{R} \tag{4.1}$$

where $\Delta_e h$ is the molar heat of evaporation and R is the molar gas constant. In deriving equation 4.1 it is supposed that we deal with an ideal gas. Rewriting equation 4.1 in a

form which is more appropriate we get:

$$p(T) = p_0 \exp A(\frac{1}{300} - \frac{1}{T})$$ (4.2)

where p_0 is the TMAE vapour pressure at 300 K and A is a constant.

The photon absorption at wavelength λ after passing a distance x in TMAE vapour is written as:

$$N(x, \lambda, T) = N_0 \exp - \frac{x}{l_a(\lambda, T)}$$ (4.3)

where $l_a(\lambda, T)$ is the absorption length for light with wavelength λ in TMAE vapour that is in equilibrium with TMAE liquid of temperature T.

We can define a cross section for the absorption of UV light $\sigma_a(\lambda)$ (independent of the TMAE temperature T). In analogy to equation 3.3 we have:

$$l_a(\lambda, T) = \frac{1}{n(T)\sigma_a(\lambda)}$$ (4.4)

The TMAE concentration $n(T)$ is proportional to the TMAE vapour pressure (again supposing we deal with an ideal gas):

$$n(T) = \frac{p(T)N_A}{RT}$$ (4.5)

where R is the molar gas constant and N_A is Avogadro's constant. Substituting equation 4.2 and 4.5 in 4.4 we find:

$$l_a(\lambda, T) = l_0(\lambda) \cdot T \exp A(\frac{1}{T} - \frac{1}{300})$$ (4.6)

with

$$l_0(\lambda) = \frac{R}{N_A \sigma_a(\lambda) p_0}$$ (4.7)

Strictly speaking equation 4.5 is not valid in the drift tubes because the gas temperature in the tubes (T_d) is different from the temperature of the TMAE liquid (T_l). As long as the temperature of the tubing and the drift tubes exceeds that of the liquid, no condensation will occur when the gas flows from the bubbler to the drift tubes and the TMAE concentration remains constant (though the pressure of the vapour will increase slightly). That means that $p(T_l)/T_l = p(T_d)/T_d$ so substituting the appropriate temperature would make no difference. This result differs from that of Arnold et al. [19].

The TMAE vapour pressure has been measured as a function of temperature by Anderson [11] and Giomataris et al. [58]. In table 4.1 we summarize their results. In the same table results of two absorption length measurements are given. Anderson [11] measured the absorption in TMAE with xenon scintillation light (wavelength region from 170 to

195 nm). Arnold *et al.* [19] used light with a wavelength of 200 nm. The results of both absorption length measurements have been adjusted to the parametrization of equation 4.6.

The dependence of the absorption length $l_a(\lambda, T)$ on the wavelength is more complicated. In figure 4.8 two independent measurements are shown that differ quantitatively a bit. Both measurements have been normalized to a TMAE vapour pressure of 1 torr. For a TMAE temperature of 30°C the TMAE vapour pressure is 0.71 torr and the absorption length for Čerenkov light around 180 nm is 1.4 cm.

	TMAE pressure		absorption length	
	p_0 [torr]	A [K]	l_0 [cm/K]	A [K]
Anderson	0.577	6454	$4.73 \cdot 10^{-3}$	6510
Giomataris	0.571	6285		
Arnold *et al.*			$6.19 \cdot 10^{-3}$	5614

Table 4.1: Experimental results of TMAE vapour pressure measurements by Anderson [11] and Giomataris *et al.*[58] as well as results of absorption length measurements by Anderson [11] (170-195 nm) and Arnold *et al.*[19] (200 nm). The authors do not give any error estimates for their results.

TMAE is chemically agressive. It reacts strongly with oxygen under emittance of green light (chemiluminescence). It also reacts with many materials commonly used in wire chambers like rubber O-rings and G10. The main reaction products are listed in table 4.2.

Because one needs an attenuation length for drifting electrons above 10 m in order to have a negligible loss of drifting electrons in the 1.5 m long drift tubes, electronegative gases have to be avoided. TMAE is not electronegative enough to cause any problem, but some of its reaction products are. Rewick *et al.* [60] showed that of these products TMO has an

Symbol	Name	Formula
DMA	Dimethylamine	$(CH_3)_2NH$
TMU	Tetramethylurea	$[(CH_3)_2N]_2 - C = O$
TMO	Tetramethyloxamide	$[(CH_3)_2N]_2 - (C = O)_2$
BMAM	Bis(dimethylamino)methane	$[(CH_3)_2N]_2 - CH_2$
TMH	Tetramethylhydrazine	$(CH_3)_2 - N - N(CH_3)_2$
DMF	Dimethylformamide	$H(C = O) - N(CH_3)_2$

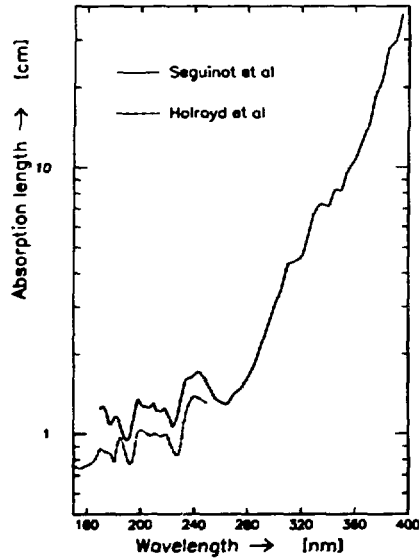Table 4.2: The most common impurities in TMAE.

Figure 4.8: TMAE absorption length versus wavelength as measured by Seguinot *et al.*[59] and Holroyd *et al.*[7]; TMAE vapour pressure *is 1 torr.*

electronegativity much stronger than that of oxygen, whereas TMU is comparable to oxygen in this respect. To minimize the occurence of these substances the following measures are taken: construction materials that are known to react with TMAE are avoided, the oxygen concentration in the gas system has to be below 1 ppm before TMAE is added to the drift gas and the TMAE liquid has to be cleaned thoroughly before use.

The following cleaning methods of TMAE can be found in literature:

1. Water washing [11] i.e. TMAE is shaken with water and separated afterwards. Oxidation products soluble in water are removed with the water (DMA, TMU and TMO).

2. Vacuum distillation [11].

3. Pumping off 10% of TMAE volume [11].

4. Flushing of the TMAE filled bubbler with clean gas [61].

5. Addition of alumina to the TMAE [11].

The cleaning procedure for the TMAE used in the BRICH will be water washing followed by distillation. The results of this method are presented in section 7.4.

Chapter 5

The BRICH wire chamber

5.1 Introduction

In the DELPHI barrel RICH detector the Čerenkov photon conversion points are measured in a wire chamber. Many wire chamber prototypes have been developed and tested before the final design was fixed. Prior to a discussion of three different prototypes and the final chamber, the criteria are presented that a wire chamber in the BRICH has to meet:

- A spatial resolution (rms) of 1 mm is required for the x and z-coordinate. This implies that the wire to wire distance should be less then 3.5 mm and that the time resolution should be better than 40 ns.

- A stable drift gas permitting a high gas amplification is required to boost the single electron detection efficiency to a high value. Methane and ethane are good candidates for the drift gas; iso-butane is also acceptable but possesses a rather high electron attachment coefficient (section 3.5).

- An efficient electron detection requires good field optics that focuses the electrons onto the anode wires without loss.

- UV photons, emitted from the avalanches, generate new photoelectrons in a medium that is per definition photosensitive. This phenomenon is called "photon feedback". An optical shielding between the anode wires is necessary to avoid spreading of the signal to adjacent wires by this mechanism.

- Apart from the x and z-coordinate also the y-coordinate has to be recorded. This can be done by strips on the cathode plane. A good coupling between anode wires and cathode plane is essential to achieve a high cathode detection efficiency. Another possibility for obtaining the y-coordinate is by using the technique of charge division, as is done in the wire chamber for the SLD detector at SLAC [44].

- The length of the cathode strips is a compromise between the number of channels to be read out and the occurence of spurious events, called "ghosts". The width of the strips determines the minimal resolution that can be obtained in the y-direction.

- Cross-talk due to capacitive coupling from anode to anode and from cathode to cathode has to be avoided.

- Positive ions, produced in the avalanches, drift into the drift volume, giving rise to a space charge that distorts the drift paths of the electrons. This effect is strongly reduced by gating the chamber, i.e. by opening it electro-statically for potentially interesting events only. An important benefit is also the slowing down of ageing of the wires.

- The chamber has to maintain full collection efficiency when operated in a magnetic field of 1.2 T and at a pressure of 1.3 bar absolute.

- The chamber has to be rigid enough to stand an overpressure from the inside of 0.3 bar.

In the next three sections various wire chamber prototypes will be discussed, followed by a section in which the chamber is described that was finally adopted.
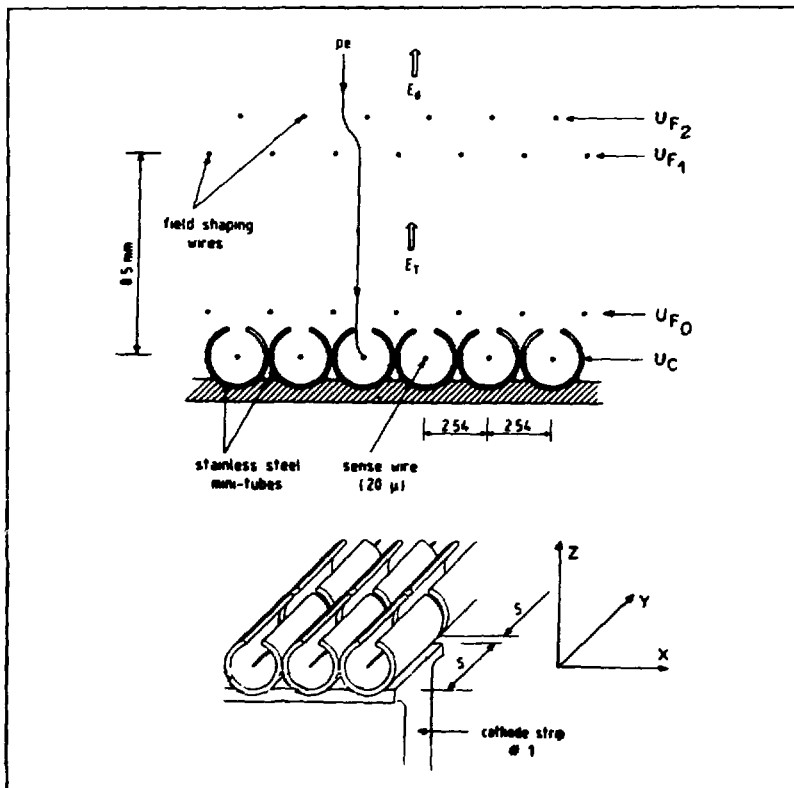

Figure 5.1: Structure of a minitube chamber.

5.2   The minitube chamber

In a "minitube" chamber the cathode is of cylindrical shape, surrounding the anode wire, thus giving an optimal anode-cathode coupling and a good shielding for photon feedback. In the DELPHI BRICH prototype [19] the 3 drift tubes were equipped with minitube chambers (figure 5.1).

Each chamber contains 71 stainless-steel cylindrical cathodes, 60 mm long, 2.0 mm inner and 2.5 mm outer diameter. After soldering the tubes side by side a slit of 0.8 mm width is cut in each of these, parallel to the tubes axis and over the full length. Next the assembled tubes are cut in the direction perpendicular to their axis to form cathode strips with a width of 5 mm. Finally the anode wires (20 μm diameter; gold plated tungsten) are centered in the tubes.

Two planes - F_1 and F_2 - with field shaping wires (50 μm diameter) focus the electrons through the slits. Electrostatic calculations show that the plane F_2 picks up about 12% of the electron flux, thus leading to a transfer efficiency of 88%. The two wire planes provide the possibility of gating the chamber. Decreasing the voltage on F_1 with 100 V and increasing the voltage on F_2 with the same amount reduces the positive ion current by more than 3 orders of magnitude. Baillon et al.[62] demonstrated that in a magnetic field of 1.2 T parallel to the drift field a third focussing plane F_0 has to be used to avoid an additional loss of 25%.

The prototype was operated with a drift gas consisting of 75% methane and 25% ethane with a small TMAE admixture. The anodes were DC grounded; the operating cathode voltage (U_c) was -1.63 kV. The anode and cathode signals were recorded with TDC's; if needed ADC's could be used as well.

A Monte-Carlo program has been written to simulate the data [19]. In figure 5.2a and 5.2b experimental values for the anode and cathode detection efficiency are compared with those of the simulation. At the operating voltage of -1.63 kV the anode efficiency is estimated to be 0.97, whereas the cathode efficiency is 0.92. The simulation shows that the difference between the two efficiencies can be explained by the ratio of cathode to anode pulseheight that was measured to be 77.5%.

Secondary photoelectrons created by the photons from an avalanche can create new avalanches not only on neighbouring wires but also on the primary wire itself. We may define α as the rate of secondary avalanches per femto-coulomb (fC) of charge in the primary avalanche. This rate is independent of the size of the avalanche. If $\bar{q}$ is the mean charge then the chamber is expected to become unstable when $\alpha\bar{q} \approx 1$.

The resolution in the y direction is limited by the width of the strips to $5.0/\sqrt{12} = 1.4$ mm. The measured resolution is worse due to cross-talk between strips as well as to secondary avalanches along the wires. In figure 5.2c the mean strip multiplicity per cluster is shown, where a cluster is defined as a group of adjacent strips with simultaneous signals.
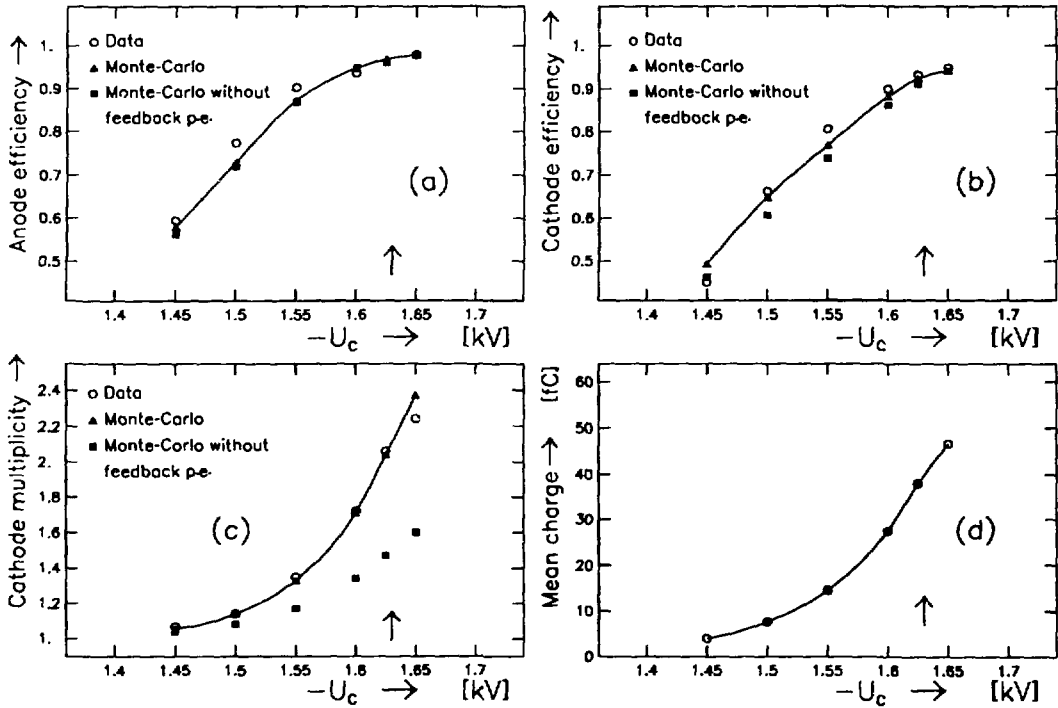
Figure 5.2:   Comparison of results in a minitube chamber with Monte-Carlo simulations with and without feedback photoelectrons [19]; the operating voltage is indicated by arrows; (a) mean anode detection efficiency (normalized on the Monte-Carlo; (b) mean cathode detection efficiency; (c) mean cathode multiplicity; (d) mean anode charge.

In the figure the experimental data are compared with simulation results with and without photon feedback. Clearly photon feedback gives an important contribution. The best fit was obtained with $\alpha = 0.02/\text{fC}$. In figure 5.2d the mean charge per avalanche $\bar{q}$ is shown as a function of the cathode voltage. At $U_c = -1.65$ kV the mean charge is 47 fC. Consequently at the highest obtainable voltage $\alpha\bar{q}$ is indeed approaching 1. At an operating voltage of -1.63 kV the mean charge is 38 fC, corresponding to an electron amplification of $2.4\cdot10^5$.

5.3   The flat cathode chamber

Figure 5.3 shows the layout of a wire chamber prototype with a flat cathode. The anodes are gold plated tungsten wires of 20 μm diameter. Below the anode plane, at a distance
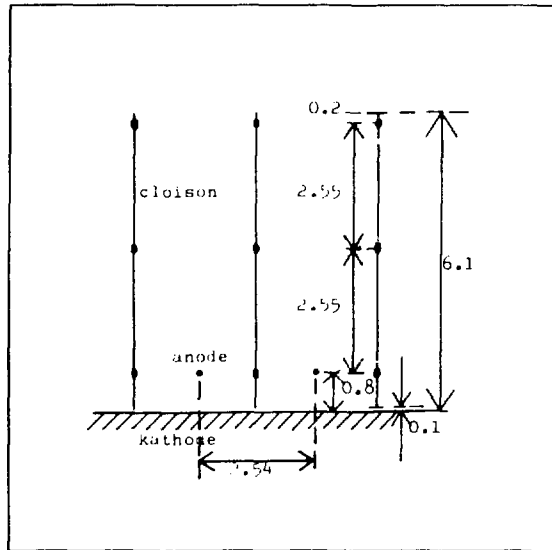
Figure 5.3: Structure of a chamber with a flat cathode plane.

of ≈ 1 mm, the cathode plane is mounted, subdivided into copper strips 5.4 mm wide, 0.2 mm apart and perpendicular to the anode wires. The strips were etched on a G10 printed circuit board. In this prototype we used metal pins, fed through the stesalit structure supporting the wires, to bring the signals outside the chamber. This choice led to an unacceptable amount of cross-talk as will be shown later (fig. 5.4).

Alumina shieldings, called "cloisons", are placed in between the anode wires. They are 6.0 mm high and 0.25 mm thick. Three potential strips on their surface serve to guide the drifting electrons to the anode wires without loss. It has been shown that the chamber remains fully efficient in a magnetic field parallel to the drift field up to 1.2 T [62].

Since the anodes are DC grounded, the size of the avalanches is determined by the voltage on the cathode plane (U_c) and on the lowest cloison strip (U_{S1}). A current setting is $U_c = U_{S1} = -1.80$ kV. The voltages on the other cloison strips are related to this value. The voltage differences between S_1-S_2 and S_2-S_3 are typically 700-1000 V.

A flat cathode chamber was tested in two different test setups. In the NIKHEF test setup a N_2-laser [63] was used to ionize gas molecules in a small drift volume. The wavelength of the laser (337 nm) is too high for direct or two step ionization of the methane/ethane drift gas itself. Signals are obtained nevertheless due to ionization of unknown impurities in the gas, possibly caused by outgassing from the chamber materials [64]. The concentration of these impurities is rather unstable which is a disadvantage of the method. Home made low noise preamplifiers were used in combination with LeCroy ADC's (2249W). A caviar micro-computer was used for CAMAC readout and on-line analysis.

The second setup was at CRN-Strasbourg. Here TMAE (4°C) was added to the drift gas to detect the UV light from a hydrogen filled flash tube. The preamps and TDC's used are described in section 5.5.2. A NORD 100 computer was used for readout and data recording on tapes. The data have been analysed off-line at NIKHEF.

The voltages gouverning the entrance optics of the chamber and the gas multiplication have to be chosen such that the detection of electrons, that are liberated in the drift volume and succeed in arriving near the wire chamber, is optimal. When the voltages approach their optimum values, an increasing number of electrons reach the anode and more avalanches occur above threshold until finally all electrons are detected. In that case the detection efficiency is at its maximum. This efficiency can not be measured directly. What can be measured is the number of hits per wire as a function of cathode and S_1 voltages. This curve is expected to have the same shape as the electron detection efficiency curve and should show a plateau when the efficiency is at its maximum.
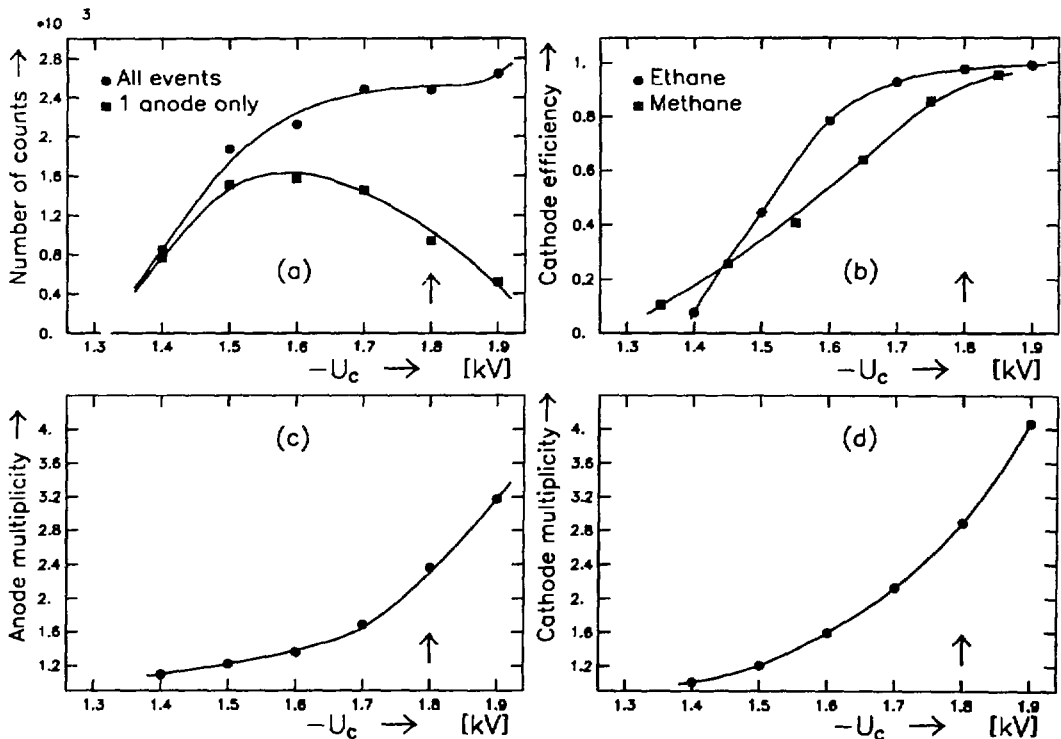

Figure 5.4: Behaviour of the flat cathode prototype chamber: (a) number of events with hits on anode wires and number of events with a single wire hit only; (b) mean cathode detection efficiency; (c) mean anode multiplicity per event; (d) mean cathode multiplicity per event.

In figure 5.4a the number of counts on the anode wires is shown as a function of the voltage on cathode plane and first cloison strip ($U_c = U_{S1}$). A plateau starts at $\approx$-1.7 kV. Figure 5.4b shows the cathode efficiency for two different gases. In both gases an efficiency better then 95% is reached, thus proving that with a flat cathode structure an efficient detection of the cathode signals can be obtained. In figure 5.4a the amount of events with only one wire hit is shown and indicates a strong cross-talk between anode wires. One observes indeed that the mean anode multiplicity (fig. 5.4c) increases strongly with the cathode voltage. The same is true for the mean cathode multiplicity (fig. 5.4d).

Cross-talk outside chamber

(a)

Cross-talk inside chamber
• to first neighbour
■ to second neighbour
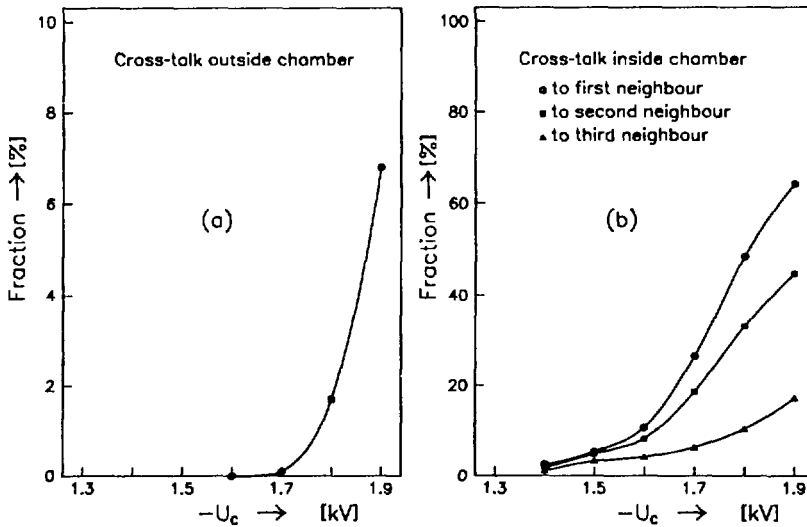▲ to third neighbour

(b)

Fraction → [%]

$-U_c$ → [kV]

Figure 5.5: Capacitive cross-talk outside (a) and inside (b) the prototype chamber with a flat cathode as a function of the cathode voltage ($U_c = U_{S1}$).

Three kinds of anode cross-talk can be distinguished:

- Cross-talk occurring *outside* the wire chamber, for instance in cables, preamps etc. This cross-talk can be measured by disconnecting one channel from the chamber. Results are displayed in figure 5.5a where the number of counts on a disconnected channel is given relative to the number of counts on one of its neighbours. A maximum of 6.8% has been found at -1.9 kV.

- Cross-talk occurring *inside* the chamber and originating from capacitive coupling between neighbouring wires. In figure 5.5b the percentage of signal observed on a first, second and third neighbour is displayed. From the strong dependence on the voltage it can be concluded that these signals are all parasitic. A maximum of 64% has been found at -1.9 kV.

- Cross-talk originating from *photon-feedback* into the drift region. It can be isolated from the other types of cross-talk because its signals are later in time. It was found to occur in less than 3.8% of the events at the highest voltages. To avoid secondary signals on the same wire a dead time of 300 ns is generated for the read out of each wire that receives a hit. In less then 4.2% of the events a secondary hit was detected after this dead-time interval.

Clearly the capacitive coupling inside the chamber is responsible for the high anode multiplicity. It could be reduced by avoiding materials with high dielectric constant between the anode wires and the connections with the preamplifiers (compare with figure 5.13c).
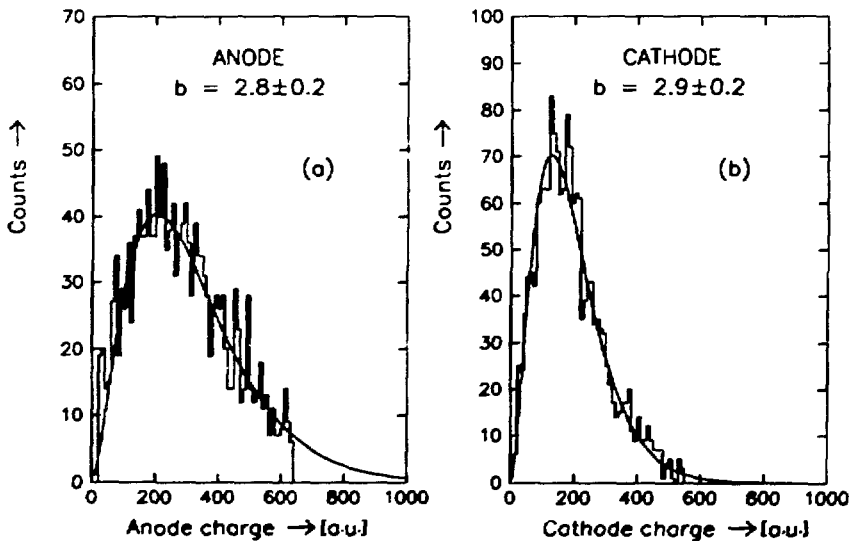

Figure 5.6: Pulseheight distribution measured in the prototype chamber with a flat cathode plane and the Polya-fit through the data (U_c = -1.80 kV; gas 75% methane + 25% ethane).

The ratio between the induced charge on the cathode and the anode charge was measured to be (35±4)%. Apparently this is sufficient to reach a good cathode efficiency. During these measurements the pulseheight distributions were recorded. Polya-curves, as defined in equation 3.55 have been fitted to the data. The data and the best fit are shown in figure 5.6a for anode wires and in figure 5.6b for cathode strips. The values for the b-parameter are indicated in the figures.
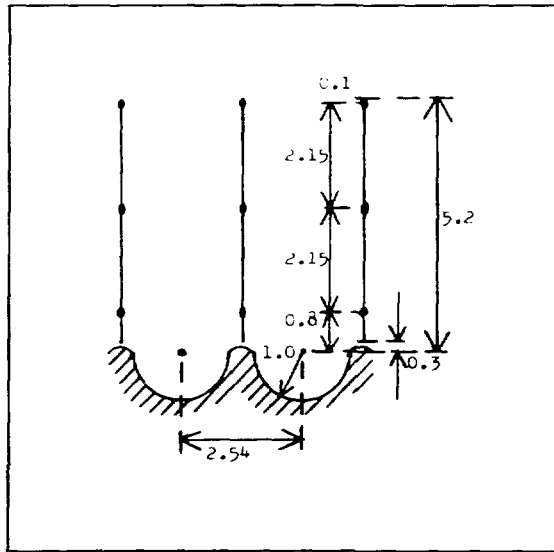
Figure 5.7: Structure of the U-shaped chamber.

5.4 The U-shaped cathode chamber

In order to combine the advantages of the minitube chamber and the flat cathode chamber, a chamber with U-shaped cathodes has been proposed. In figure 5.7 the layout is shown. The cathode plane consists of an insulating material (perspex) with cylindrical grooves at a 2.54 mm pitch (radius 1 mm). After deposition of a silver coating, strips are formed by cutting the base plate every 5.4 mm. Pins are connected to feed the signals through the perspex. Thus the strip to strip capacitance is lower than for the minitube chamber. The anode wires (20 μm diameter; gold plated tungsten) are centered as shown in the drawing.

Like for the flat cathode chamber also for the U-shaped cathode chamber cloisons are needed to avoid photon feedback to neighbouring wires. They are made of alumina (0.25 mm thick; 4.9 mm high) with 3 potential strips to guide the electrons.

With a U-shaped chamber built at NIKHEF the cathode-anode pulseheight ratio was measured to be (55±6)% (figure 5.8).

The choice of perspex as a base material appeared to be a bad one; its thermal expansion makes the silver layer crack. Further developments using another base material, as well as that of the minitube cathode structures, were discontinued, since it was demonstrated that good cathode efficiencies can be obtained with flat cathodes as well, and since flat cathode chambers are much simpler to produce.
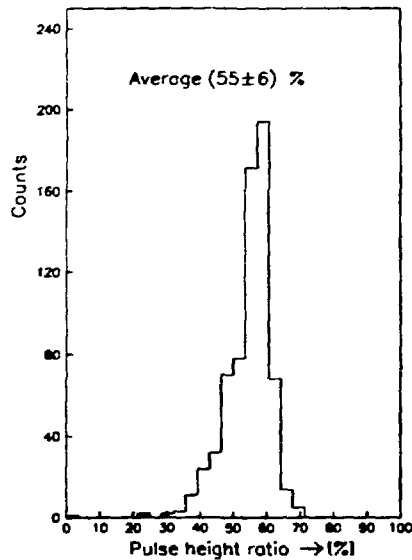
Figure 5.8: The ratio between cathode and anode pulseheights as measured in the chamber with U-shaped cathodes.

5.5   The final BRICH wire chamber

When the design of the wire chamber for the DELPHI barrel RICH was thought to be finalized (spring 1986) a chamber was built and tested in a beam setup. The results of the test, presented in section 5.5.3, led to some minor modifications to the chamber:

- The wire diameter was increased from 15 μm to 20 μm as a measure of safety against wire fracture.

- The distance between the lower edge of the cloison and the first potential strip on the cloison (S1) was modified from 0.5 mm to 1.0 mm.

- A thin strip was added in between cathode blocks to eliminate cross-talk from block to block.

In section 5.5.1 the design of the final wire chamber is presented; 48 of these chambers have been built in a co-operation between NIKHEF-H and CRN-Strasbourg. In section 5.5.4 some test results with a final chamber are presented. It should be noted that due to the above mentioned modifications the operating voltages on the cathode plane, cloison strips and gating wires of the chamber used in the beam test are different from those of the final chambers.

5.5.1 The chamber layout

The layout of the final chamber for the DELPHI barrel RICH is shown in figure 5.9.
Each chamber contains 128 gold plated tungsten wires, 20 μm diameter, 70 mm long and
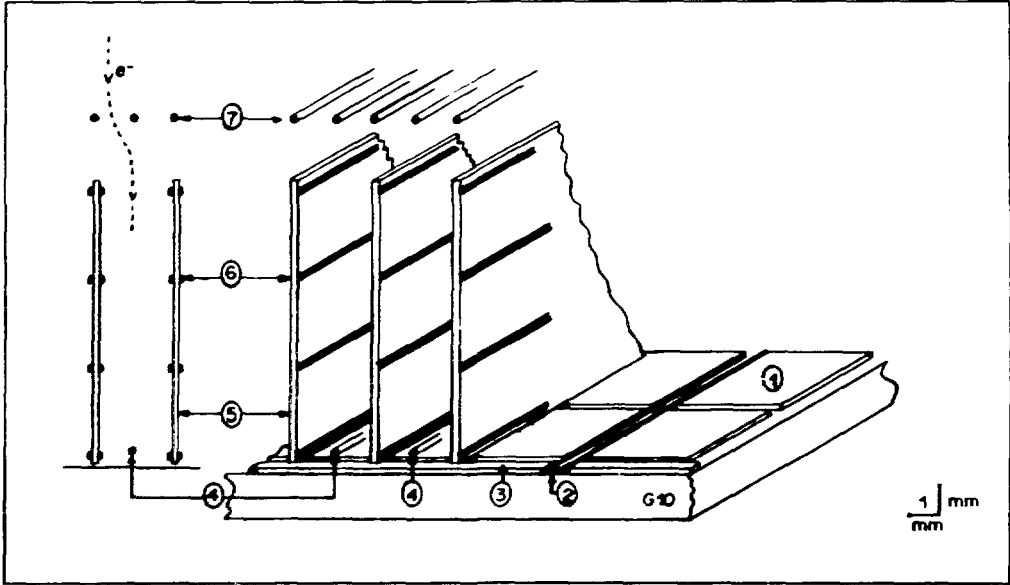

Figure 5.9: Layout of the final BRICH wire chamber; (1) cathode strips; (2)
guard strip between blocks; (3) outer guard strip; (4) anode wires; (5) alumina
cloisons; (6) cloison strips; (7) gating grid wires.

mounted with a pitch of 2.62 mm. The wires are soldered at each end onto a printed circuit
board. Thin wires connect the signals from there to the preamps at the backside of the
chamber. The construction has been optimized to reduce cross-talk between the wires by
avoiding material with a high dielectric constant between them. The anode wires are held
in position at 0.5 mm above the cathode plane by a precisely machined stesalit support.
This distance is one of the critical points in the chamber construction; it has to be kept
within 0.02 mm to ensure a homogeneous gain over the whole chamber.

The cathode plane consists of a 1.6 mm thick G10 printed circuit board subdivided
into 8 blocks. Each block consists of 16 gold plated copper strips 3.8 mm wide and 41.6
mm long at a pitch of 4.0 mm. In between cathode blocks a thin metal strip (0.2 mm),
held at the same potential as the cathode, decouples the blocks capacitively and efficiently
reduces cross-talk between cathode blocks. Each cathode block covers 16 anode wires; the
edge of the blocks and the additional decoupling strip is for all blocks situated below a
cloison. Via throughplated holes the cathode strips are connected to the backside of the
p.c. board, where each strip is connected to high voltage via a 3.3 MΩ resistor as well as

to a preamp via a 150 pF capacitor

The cloisons are laser cut from alumina sheets; they are 0.25 mm thick and 9.75 mm high, thus limiting the opening angle seen from the anode wire to 3% of the full solid angle. The cloisons are equipped with 4 equipotential strips, spaced at regular intervals over the height.

The gating grid consists of one layer of wires (40 μm) running parallel to the cloisons. The wires can be subdivided into two groups. The wires of group G_1 are positioned just above the cloisons, while the wires of group G_2 are positioned half-way between, i.e. just above the anode wires. The distance from the top of the cloisons to the gating grid is 3 mm. The voltages on both groups can be chosen independently, offering the possibility of gating the chamber. The gating system is the subject of the next chapter.

To reduce the number of HV-connections, a resistor bridge is mounted in each chamber, consisting of 4 resistors of 24 MΩ, one between each of the pairs S_1-S_2, S_2-S_3, S_3-S_4 and S_4-G_1. A typical voltage setting is: U_c=-1.50 kV, U_{S1}=-2.00 kV, U_{G1}=-3.90 kV and U_{G2}=-3.90 kV. If a measurement is made with varying cathode voltage the voltage differences with S_1, G_1 and G_2 are kept constant.
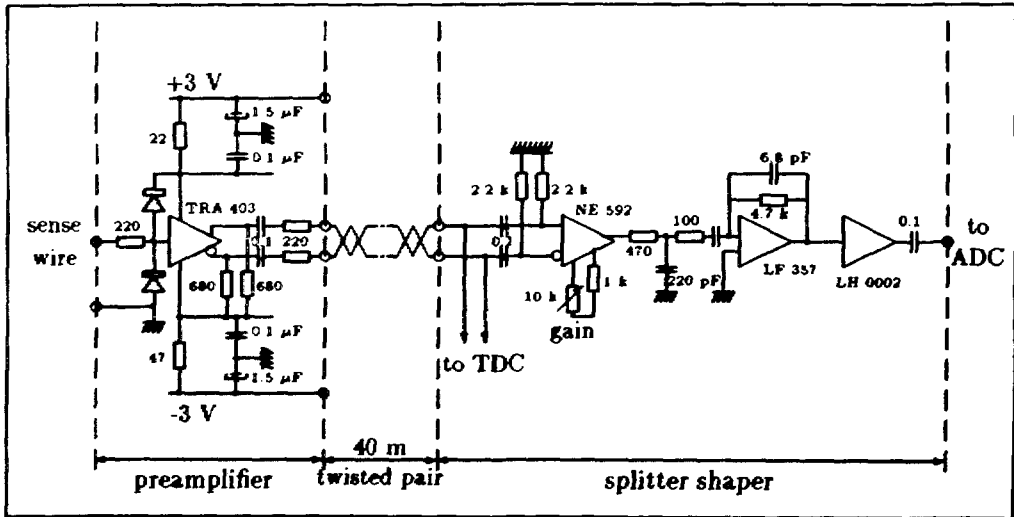

Figure 5.10: The analogue electronics chain.

5.5.2   Electronics and data acquisition

The 128 anode wires and 128 cathode strips are connected to 32 preamplifier cards with 8 channels each. The design of the preamplifiers (figure 5.10) is based on the LeCroy TRA403

chip [65]. The rise time is 6 ns; the gain amounts to ≈ 0.1 V/μA. The energy dissipation per channel is 55 mW.

In the test setups described hereafter the signals of two pairs of preamplifier cards are linked to a CAMAC TDC unit [66] by means of a 40 m long signal cable. Each TDC channel contains a shaper, a discriminator with adjustable threshold and a time digitizer (32 ns time buckets; 32 μs full range). After the recording of an event the TDC channel concerned is insensitive to new events during an adjustable dead time. The special TDC clock unit synchronizes the data taking and read-out of the TDC units.

The final BRICH data acquisition system uses FASTBUS discriminator units [67] followed by LTD units (Lep Time Digitizer) [68], containing 48 channels each. The time resolution of 8 ns can be improved to 2 ns by using interpolators. Threshold and dead-time are adjustable with a G64 slow control system.
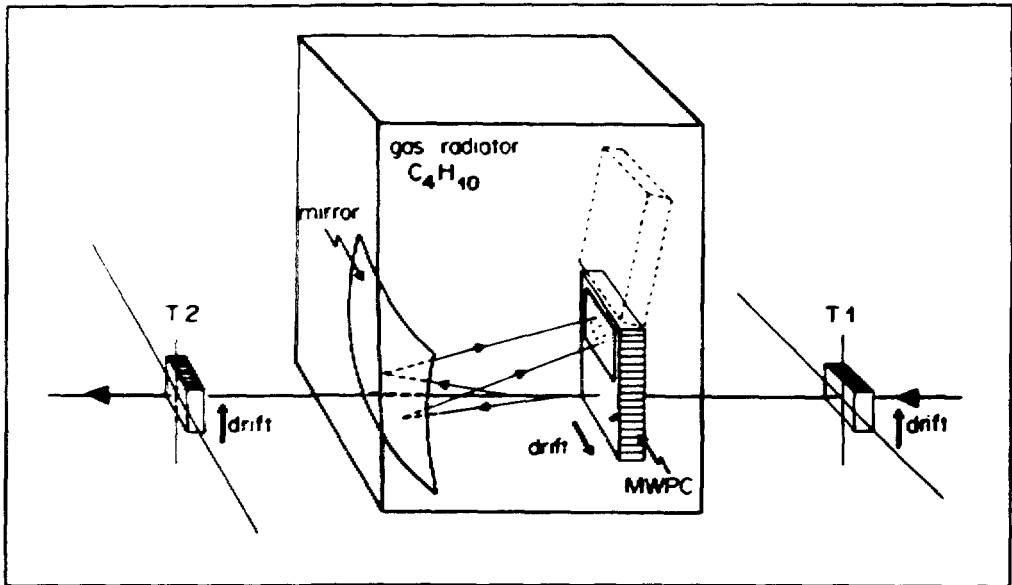

Figure 5.11: Chamber test setup in a 10 GeV/c π^- beam (T_1 and T_2: beam chambers).

5.5.3 The beam test

A beam test has been performed with a wire chamber that closely resembled the final chamber. The test was performed at CERN with a 10 GeV/c π^- beam. The test setup is shown in figure 5.11. The beam particles create Čerenkov photons in an isobutane gas radiator (STP) of 48.2 cm depth. A spherical mirror of 50 cm focal length focuses these

photons into a drift tube, filled with a 75% methane-25% ethane mixture and TMAE vapour (25°C). The drift tube is 16 cm long (along the drift direction), 34 cm wide and 6 cm deep. After crossing a 4 mm thick transparent quartz window the UV photons are absorbed by the TMAE and the photoelectrons produced drift 7 cm on average under a uniform electric field of 0.6 kV/cm. Two drift chambers T_1 and T_2 measure the position of the beam particles. A coincidence between four scintillators provides a trigger. The beam contained mainly pions; small admixtures of muons and electrons were identified as well (figure 2.2).
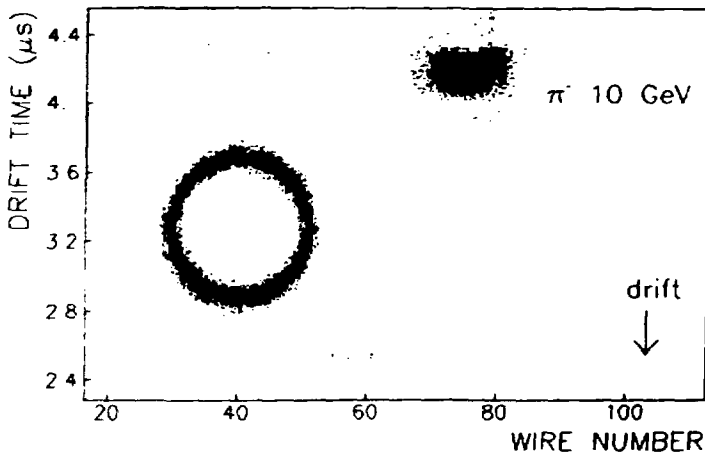

Figure 5.12: Cumulated images of 500 Čerenkov rings and π^- tracks measured with the BRICH final wire chamber (U_{S1}=-1.55 kV).

In figure 5.12 a scatterplot is shown of 500 cumulated events. The spot in the upper corner is due to ionization by beam particles passing through the drift volume.

Figure 5.13 summarizes the test result concerning the chamber parameters. In 5.13a the mean number of detected Čerenkov photons in a ring-shaped fiducial region with radii between 1.7 and 3.5 cm is shown versus the voltage on the lower cloison strip (U_{S1}). The voltage on the cathode strips is a fixed percentage of this: U_c=0.92·U_{S1}. The data was taken with a discrimination level of 5.1 mV for the anodes and 4.4 mV for the cathodes. The open circles in figure 5.13a represent the uncorrected data. After subtraction of the noise, the mean number of anode hits (full circles) reaches a plateau above U_{S1} = -1.52 kV at 13.4±0.2. The size of the plateau is sufficient to guarantee a stable chamber operation.

Three different sources of noise can be identified [69]:

- A uniform background of 1% per Čerenkov photoelectron due to rings generated by out of time pions.
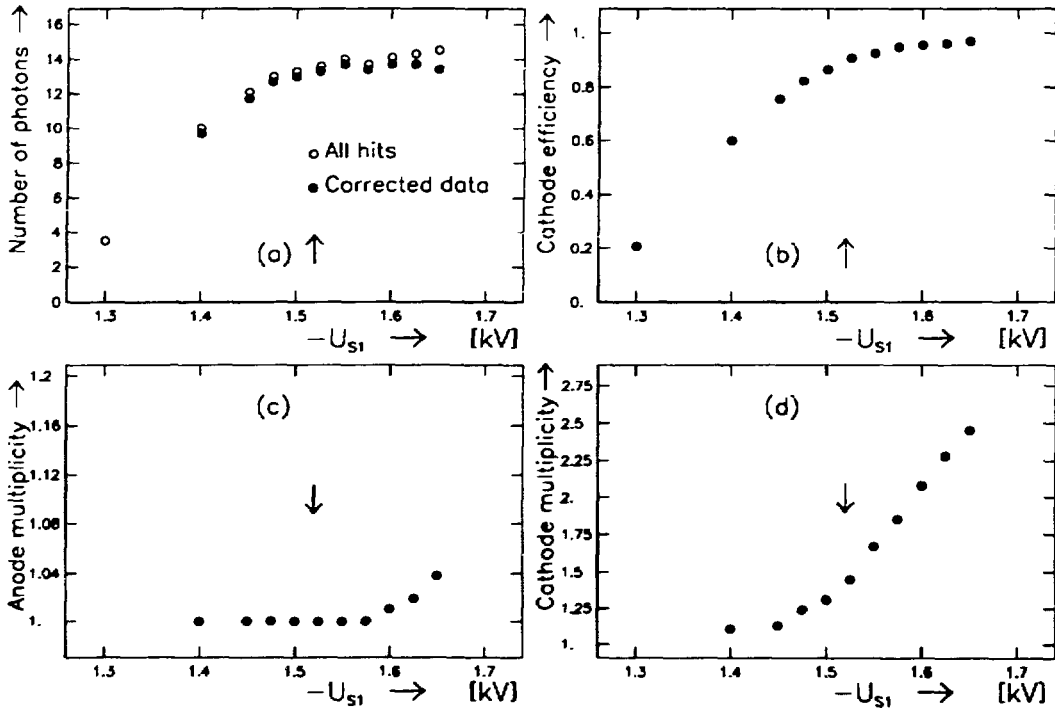
Figure 5.13: Behaviour of the final chamber ($U_c=0.92 \cdot U_{S1}$): (a) mean number of Čerenkov photons with and without corrections for noise; (b) mean cathode detection efficiency; (c) mean anode multiplicity; (d) mean cathode multiplicity.

- Secondary signals arriving after the dead time interval and originating from photon feedback increase the number of measured photons. The contribution of this effect is 5.0% at $U_c = -1.55$ kV. Because of its low level, photon feedback to adjacent wires could not be measured.

- Cross-talk between anodes giving an apparent increase of the number of simultaneous hits. The mean anode multiplicity curve in figure 5.13c shows a small increase starting at -1.60 kV. At -1.65 kV the cross-talk reaches 3.8%. This is a strong improvement compared to the test chamber (figure 5.5a and 5.5b) and justifies the new method of wire feedthrough.

The cathode efficiency and mean cathode multiplicity are shown in figure 5.13b and 5.13d. At -1.52 kV the cathode efficiency is 90%.

To eliminate block to block cross-talk a thin strip was added as a separation between

cathode blocks. This modification was adopted after measuring in the first beam tests a cross-talk between cathode blocks close to 100% for signals from beam particles. After the modification the cross-talk reduced to a level of 1.5%.
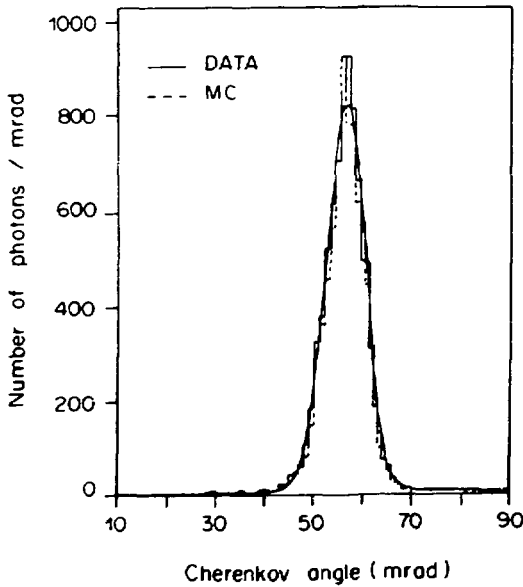

Figure 5.14: The Čerenkov angle distribution as calculated from observed single photons; a comparison is made with a Monte-Carlo simulation (U_{Si}=-1.55 kV; 10 GeV π^-; isobutane radiator).

For each Čerenkov photon the Čerenkov angle can be calculated from its measured coordinates and from the measured parameters of the beam particle track. The result is shown in figure 5.14. A gaussian fit gives a mean Čerenkov angle θ_c = 56.16±0.03 mrad and a resolution per photoelectron σ_c = 3.94±0.03 mrad. This result is in agreement with a Monte-Carlo simulation [70], from which can be concluded that with a perfectly defined beam and a better time resolution, the resolution per photoelectron would be 2.8 mrad.

From the mean number of detected Čerenkov photons, amounting to 13.4 on the plateau, the quality factor of the setup can be calculated and gives as a result: N_0=(89±2) cm^{-1}.
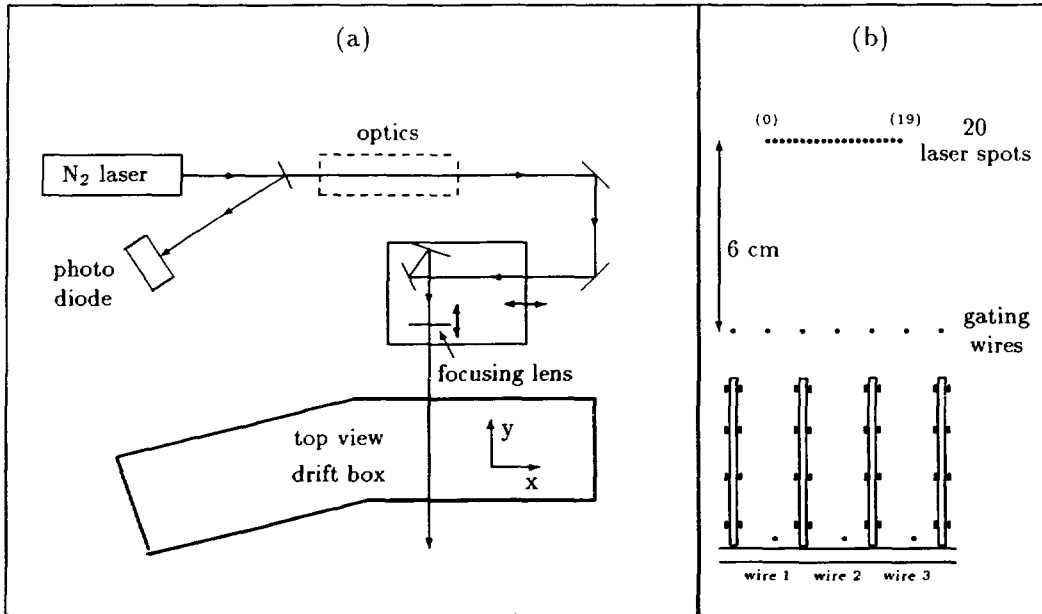
Figure 5.15: Layout of: (a) the NIKHEF-setup; (b) the scan perpendicular to the anode wires.

5.5.4   The tests at NIKHEF

Description of the setup

In the NIKHEF test setup a N_2-laser [63] is used to ionize the gas in a small drift volume (length 15 cm) enclosed in an aluminium test box. The box has quartz windows on all sides. It can contain two chambers mounted together on a 15°-flange. As indicated in figure 5.15a, part of the laser beam light is reflected and focused onto a photodiode. The diode signal is read out by an ADC and measures the laser intensity. It is also used as a trigger for the data acquisition. The optics in the laser beam, consisting of 4 lenses to make a parallel beam; 2 diaphragms and several filters to reduce the intensity, are omitted from the figure. One of the ways of using the laser is to focus its expanded and parallel beam by means of a large aperture astigmatic lens (f=20 mm) into the drift volume. Only at the focal point the energy density is sufficiently high to create photoelectrons via the two step ionization process. The spot size, defined as the region in which photoelectrons are created, has a length of 0.2 mm and a diameter of 20 μm. The spot can be precisely positioned and moved in the drift volume by means of a setup consisting of two translation stages, mounted on top of each other. On the first stage that can be moved in the x-direction a mirror pair is mounted, bending the beam over 90° towards the lens. This lens is mounted on the second stage, that can be moved in the y-direction. The stages are powered by

computer controlled stepping motors with an accuracy in the position of 2 μm. A more extensive description of the setup can be found elsewhere [71].
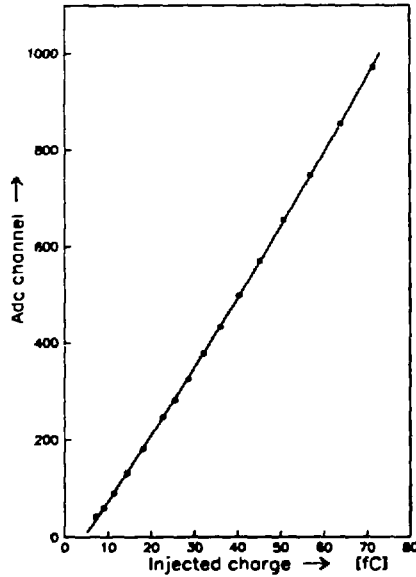

Figure 5.16: Calibration data of one preamplifier channel and the corresponding shaper channel. The line represents a quadratic fit.

The preamplifiers and TDC's are described in section 5.5.2. The possibility to measure pulseheights with an ADC (LeCroy 2259B) is included in the setup. Splitter-shaper units (figure 5.10) offer the possibility to send preamp signals to both the ADC and TDC's. A calibration was made for each combination of preamp channel and shaper channel. An example of the calibration data of such a combination together with a quadratic fit to the data is shown in figure 5.16.

U_c [kV]	PH-ratio	A	b-anode	b-cathode
1.55	51.5±4.2	$1.3 \cdot 10^5$	1.14±0.09	1.54±0.18
1.60	52.4±3.9	$2.7 \cdot 10^5$	1.13±0.12	1.59±0.16
1.65	52.2±3.8	$4.3 \cdot 10^5$	1.06±0.13	1.49±0.12

Table 5.1: The cathode to anode pulseheight ratio in %; the gas amplification A; the b-parameters from fits of a Polya-curve to the anode and cathode pulseheight distributions ($U_c = U_{S1}$).

Pulseheight measurements

The ratio between cathode and anode charge was measured for 3 different cathode voltages. The results are listed in table 5.1 together with the mean gas amplification. As expected the ratio is independent of the amplification. Figure 5.17 shows the ratio for U_c=-1.60 kV as well as the pulseheight distribution on anodes and cathodes. A Polya-distribution was fitted to these data. The results of the fits are listed in the same table.

To suppress the noise contribution to the ratio measurement, the software threshold for the ADC data was set rather high compared to the threshold as it is used in the TDC read out. The ADC threshold corresponded to an input charge of 9 fC as can be seen in the figures 5.17a and 5.17b. Consequently the loss below the threshold should not be interpreted as an inefficiency for a TDC measurement.
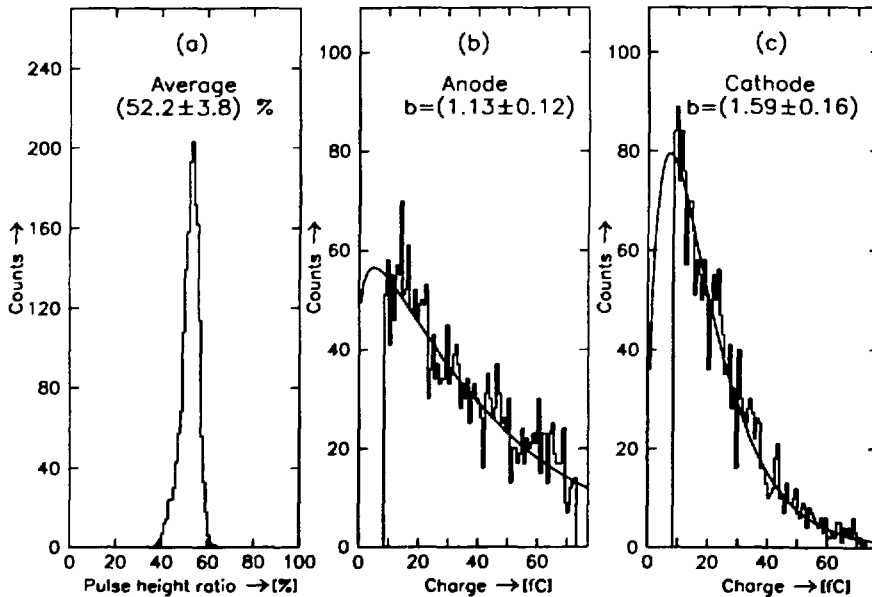
Figure 5.17: ADC-measurements in the final chamber (U_c=U_{S1}=-1.60 kV; 75% methane + 25% ethane): (a) cathode-anode pulseheight ratio; (b) anode pulseheight distribution with Polya-fit; (c) cathode pulseheight distribution with Polya-fit.

The anode efficiency

When a wire chamber is operated on its plateau the efficiency of the chamber is expected to be 100%. Due to the Polya-shape of the single electron pulseheight distribution, as defined by equation 3.55, this efficiency can never be achieved since a small percentage

of the pulses is unavoidably below threshold. For a fixed threshold the amount of signals below threshold depends on the cathode voltage. As a consequence the plateau will always show a slight slope. This is indeed observed. To minimize this inefficiency a high b-value is desirable and the preamplifier noise has to be as low as possible which in turn permits a low threshold setting.

The anode detection efficiency was measured for different cathode voltages by Dracos and Loukas [72] in a final chamber for a threshold corresponding to an input charge of 2.0 fC (=12700 e^-). They found anode efficiencies of 94.3%, 96.7%, 97.8% and 98.4% for cathode voltages of -1.40 kV, -1.45 kV, -1.50 kV and -1.55 kV, respectively.

The scan perpendicular to the anode wires

Apart from the loss discussed in the previous section one can expect another inefficiency: that caused by electron loss on the gating wires and/or on the top of the cloisons. Although simulations have shown that a 100% transfer efficiency can be achieved (section 6.2), this was never checked experimentally. To measure this a scan was made in the x-direction with a focused laser beam. Measurements were made at 20 different positions with a step size of 0.262 mm. The starting position is above wire 1, the last position is close to wire 3, as illustrated in figure 5.15b. Instead of making one scan with many laser shots on each position, several small scans were made with only a few hundred laser shots on each position to avoid systematic errors.

As an illustration of the expected results we show four different possible cases in figure 5.18. Figure 5.18a represents the number of TDC-counts on each wire at the 20 different positions in case the diffusion is small. Curves are drawn through the calculated points to guide the eye. The anode wires are situated at position 0, 10 and 20; the cloisons at position 5 and 15. At the first position all electrons drift to wire 1. If we move the spot to the right, there is a region around the cloison where the electrons are spread over 2 cells. If the scan is continued, only wire 2 receives electrons until the second cloison is reached and wire 3 starts to count. Also the sum of the distributions is shown; it is uniform.

Figure 5.18b displays the expected results with a more realistic diffusion. The regions around the cloisons were electrons are spread over two cells increase, but the sum is still flat. In figure 5.18c curves are shown for a small diffusion, assuming a 3% electron loss on gating group G_2 and in figure 5.18d for a more realistic diffusion, assuming a 3% electron loss on gating group G_1. Obviously the dip in the sum curve will be the more pronounced the less the diffusion. To minimize the diffusion the laser spot was brought as close to the gating grid as the setup allows i.e. at a distance of 6 cm.

During the measurements the laser intensity was adjusted such that the probability per laser shot for an event was $\approx 10\%$ entailing a probability for 2 or more electrons of $\approx 0.5\%$. Although this percentage is small, double events have a strong influence on the measurement. This is due to the fact that an event with 2 electrons is counted as one in
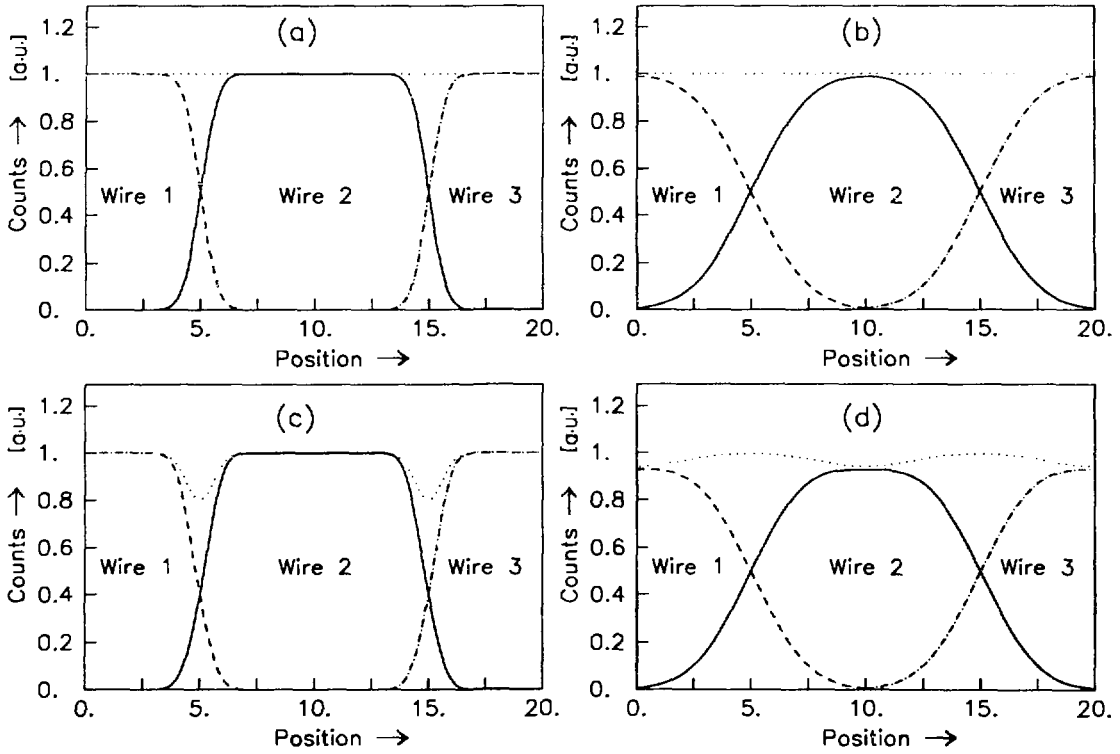
Figure 5.18: Illustration of the method of scanning perpendicular to the anode wires (located at position 0, 10 and 20), for 4 cases: (a) small diffusion, no loss; (b) realistic diffusion, no loss; (c) small diffusion, 3% loss on G_1; (d) realistic diffusion, 3% loss on G_2.

the case where both electrons arrive on the same wire, whereas it is counted as two events when each electron drifts to a different wire. Without a correction for this effect more hits would be counted when the spot is focused above a cloison then when it is focused above an anode. By measuring double events separately one can correct for this effect.

The data can be described by the following equation:

$$N_j(x_i) = K_j \left[\int_{c_j}^{c_{j+1}} \frac{1}{\sqrt{2\pi}\sigma} \exp\left(\frac{-(x - x_i)^2}{2\sigma^2}\right) dx - \sum_{k=j}^{j+1} \frac{L_0}{2} \frac{1}{\sqrt{2\pi}\sigma} \exp\left(\frac{-(c_k - x_i)^2}{2\sigma^2}\right) \right] \quad (5.1)$$

where N_j is the number of counts on wire j measured with the laser spot on position x_i. The cell containing wire j is bounded by cloison j on position c_j and cloison $j + 1$ on position c_{j+1}. The variance of the electron distribution σ is the diffusion after 6 cm of drift. L_0 is the mean percentage of electron loss on gating group G_1 (or the cloison). The second term in equation 5.1 is the loss term. It gives for wire i the electron fraction that

is lost on the cloisons at position c_j and c_{j+1} when the laser is at position x_i.
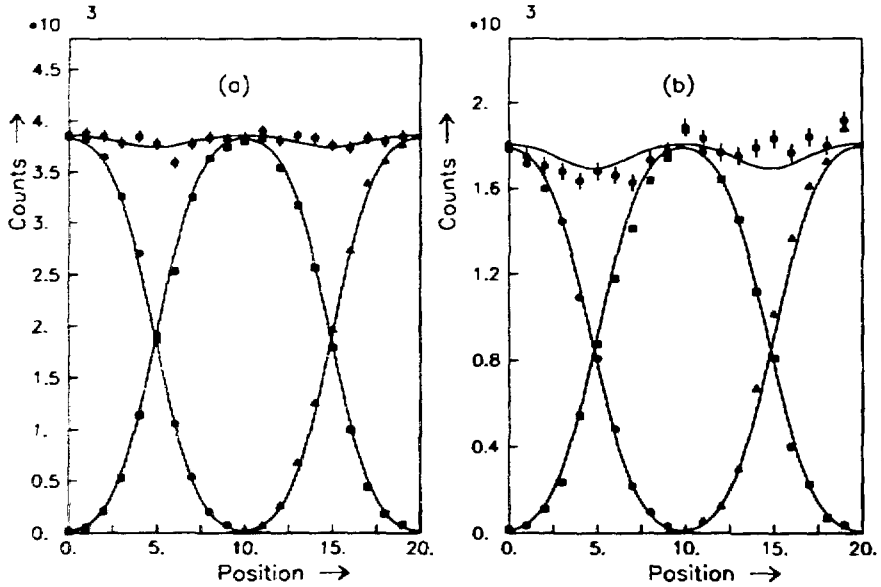

Figure 5.19: Number of counts on three adjacent wires and their sum. The upper curves represent the sum of the curves fitted through the data of the separate wires. (a) 100% ethane; (b) 75% methane and 25% ethane.

With the program MINUIT [76] the χ^2 fit of equation 5.1 to the data was minimized. Two measurements have been made, each with a different gas filling. The voltage setting was as given in section 5.5.1, i.e. $U_{G1} = U_{G2} = -4.20$ kV. The results are shown in figure 5.19. It should be noted that the fit was made to the data on the individual wires but not to the sum. Small losses around the cloisons are visible. In a first approximation the data were fitted with 4 parameters: K, a uniform normalization for all wires; σ the width of the electron distribution; L_0, the percentage of lost electrons and x_0, the starting position of the scan. The curves shown in figure 5.19 are the results of the fit. For the loss the following percentages were found:

100% ethane   : $L_0 =$ $(1.5 \pm 0.9)\%$
75% methane and 25% ethane : $L_0 =$ $(3.1 \pm 1.3)\%$
average   : $L_0 =$ $(2.3 \pm 0.8)\%$

In a second approach each wire was normalized separately, giving a total of 6 parameters to be fitted. The χ^2 improved considerably but the losses found were the same.

From static gating test results (figure 6.5) it is known that with $U_{G1} = U_{G2}$ the transfer efficiency is not 100%. A loss of $(4.5 \pm 0.8)\%$ is observed. If this is combined with the average result of the scans we find a maximum transfer efficiency of $(102.2 \pm 1.6)\%$. Hence it can

be concluded that the transfer of drifting electrons from the drift volume into the wire chamber cells has a maximum efficiency close to 100%.
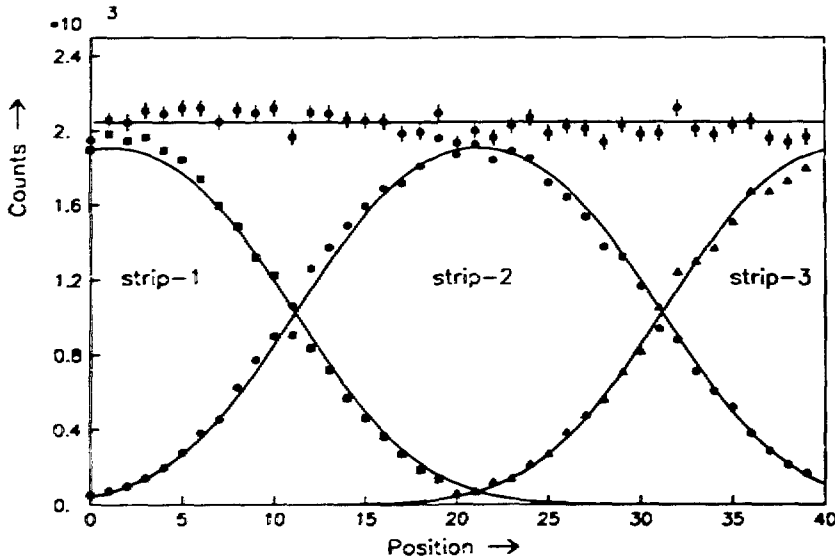

Figure 5.20: Number of counts on three adjacent cathode strips and their sum. The measurements were made at 40 different positions with a step-size of 0.2 mm positions. The result of the fit is indicated by solid lines.

Scan perpendicular to cathode strips

When an avalanche occurs on an anode wire a signal builds up both on the wire and on the cathode plane, caused by the moving cloud of ions. If the avalanche on the anode wire occurs just near the separation between cathode strips, the cathode signal is spread over two strips. One can expect this effect to decrease the cathode efficiency, since a small signal occurring on one strip might be just above threshold, whereas, if the same signal is spread over two strips, both signals might be below threshold. To measure this inefficiency a scan was made perpendicular to the cathode strips. The laser was shot into the drift box through a side window. The first position was above the middle of a strip. In 40 steps of 0.2 mm a total distance of 2 strips was scanned. A complication for the interpretation of the data is the strong cross-talk between cathode strips, increasing the number of events with hits on 2 or 3 strips. The data were corrected for this effect. In figure 5.20 the number of counts at each position is shown for the 3 strips separately, as well as the sum. No loss is observed in the sum curve. The fit result confirms this, giving a loss below 0.1% on positions between two strips.

From the data shown in figure 5.20 we can deduce the resolution of the wire chamber in the y-direction to be 1.7 mm. This is worse than the expected value of $4/\sqrt{12}=1.2$ mm; this diminution is due to cross-talk.

Another result from the scan is an estimation of the spread in the induced charge on the cathode plane. If we suppose that the charge is gaussian distributed the variance of the distribution is (0.7 ± 0.1) mm.

5.6   Ageing of the wire chambers

Ageing of wire chambers is the effect that after a certain period of operation the performance of a wire chamber diminishes. It manifests itself by an increase of the noise level and a reduction of the pulseheight. The effect has been observed by many workers in the field [73, 74]. The presence of ageing is connected to the deposition of complicated molecules on the anode wires and cathode planes (or wires).

Generally a 50% reduction of the pulseheight is found after an integrated charge of 0.1-1.0 C per centimetre of anode wire. Unfortunately ageing is about 3 orders of magnitude faster in gas mixtures containing TMAE vapour as was shown by Va'vra [75]. He found ageing, if expressed as an integrated charge per centimetre, to be dependent on the diameter of the anode wire and the gas composition but not on the gain, the temperature or the intensity of the Fe^{55} source. With a wire diameter of 20 μm and methane (with TMAE) a 50% pulseheight reduction was found after an integrated charge of $3\cdot10^{-4}$ C/cm. When pure ethane was used the same reduction was found after $9\cdot10^{-4}$ C/cm.

A beam test was performed with one of our final wire chambers to observe the ageing rate when particles are used instead of a Fe^{55} source (5.9 keV γ's). In a gas mixture consisting of 75% methane and 25% ethane a pulseheight reduction of 50% was found after an integrated charge of $(5\pm3)\cdot10^{-3}$ C/cm. Although due to experimental problems the uncertainty in our result is rather big, we conclude that it corresponds approximately to that of Va'vra quoted above.

Taking into account the expected particle flux in DELPHI and the background of cosmic rays a lifetime greater then 10 years is found for the wire chambers in the barrel RICH. If the detector would have been located at the surface the lifetime would have been about 3 years, due to the higher rate of cosmic rays.

5.7   Conclusion

A wire chamber for an efficient detection of single electrons in the DELPHI barrel RICH detector was designed, constructed and tested. The transfer of electrons from the drift

volume into the chamber cells shows no measurable loss. For cathode voltages below -1.50 kV the anode detection efficiency is above 98%, i.e. the amount of signal below threshold due to the Polya-shape of single electron pulseheight distributions is less than 2%. In the realistic situation of a beam test the cathode efficiency was measured to be better than 90%.

The spatial resolution in the x-direction is determined only by the wire spacing, i.e. 0.8 mm. The cross-talk between the anode wires is small. This in contrast to the spatial resolution of 1.7 mm in the y-direction that is dominated by cross-talk between cathode strips.

A possible inefficiency for avalanches occurring just between two cathode strips has been studied. To a level of 0.1% no loss was observed.

Chapter 6

The gating system

6.1 Introduction

Two arguments can be put forward for the addition of a wire plane just outside the wire chamber. Firstly one wants to obtain a fully efficient transfer of electrons from the drift volume into the wire chamber cells. Secondly this plane can be used for gating the chamber, i.e. electrostatically opening and closing the chamber by changing the voltages on the gating wires. When the chamber is closed, drifting electrons are prevented to travel from the drift volume into the wire chamber and ions, created in avalanches on the anode wires are prevented to drift into the drift volume. The benefit of gating is twofold. A reduction of
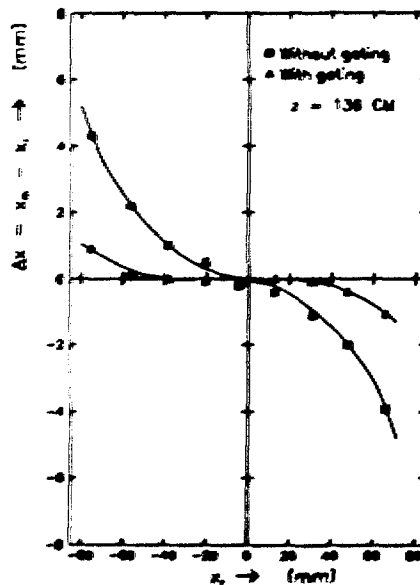

Figure 6.1: Deviation Δx between the measured x-coordinate x_m and the real x-coordinate x, as a function of x, with and without the use of the gating system. The drift distance is 136 cm; $E_d = 0.58$ kV. [19]

the space charge in the drift tubes is obtained since less ions drift through the gating grid into the drift volume, but also the ageing effects in the wire chamber are reduced since on average less electrons reach the anode wires.

The necessity to have a gating system has been demonstrated by Arnold *et al.*[19]. Imaging errors occur in the reconstruction of the photo-conversion points due to space charge in the drift volume. This is illustrated in figure 6.1 where the difference Δx between the measured x-coordinate x_m and the real x-coordinate x_r is plotted versus the real x-coordinate, for a drift distance of 136 cm. The measurements have been performed with the minitube chamber described in section 5.2, with and without the use of the gating system. The side walls of the drift tube are at x = -80 mm and at x = 80 mm. In the ungated mode the electrons experience a force causing an inward displacement up to 5 mm. The deviations are strongly reduced when the chamber is gated, which shows the importance of the gating system.

The arguments that led to the final design of the gating system are presented in the next section. In section 6.3, consisting of a reprint [77], test results with the final system are presented.
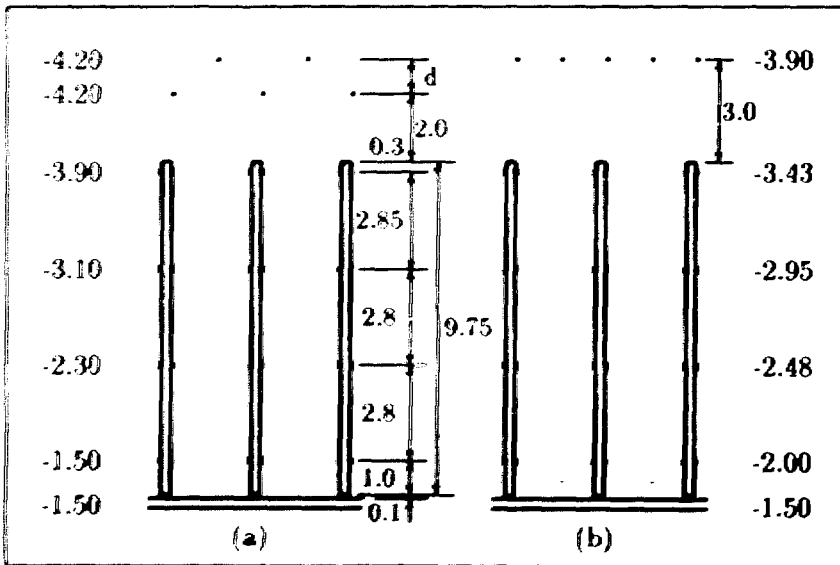

Figure 6.2: *Layout of the wire chamber with:* (a) *two planes with gating wires;* (b) *all gating wires in one plane. The voltages used on the cathode plane, cloison strips and gating wires are indicated.*

6.2   Modifications to the gating system

The original design of the gating system consisted of 2 wire planes, G_1 and G_2, 1 mm apart, as shown in figure 6.2a. The distance between the first gating plane (G_1) and the top of the cloisons was 2 mm. In figure 6.3 the transfer efficiency for drifting electrons is shown versus the voltage difference ΔU between gating plane G_1 and G_2: $\Delta U = U_{G1} - U_{G2}$. The setting of the voltages on cathode, cloison strips and gating wires are shown in figure 6.2a. At $\Delta U = 0$ V ($U_{G1} = U_{G2} = $ -4.20 kV) the transfer efficiency is 100% i.e. all drifting electrons reach the anode wires. When ΔU is set just below -100 V the transfer efficiency starts to drop since electrons are captured by the wires of gating plane G_2. Below -250 V all electrons are lost and the chamber is closed. When ΔU is increased above 100 V the efficiency starts to drop as well. In this situation the electrons are captured by the wires of grid G_1. Above 350 V all electrons are lost.
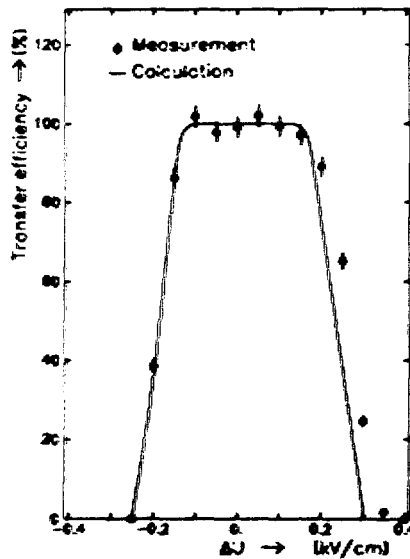
Figure 6.3: Measured and calculated transfer efficiency in a wire chamber as shown in figure 6.2a (E_{dr}=0.20 kV/cm; B=0 T).

To study the transfer efficiency in more detail a simulation has been made of the electrostatic configuration of the wire chamber with an extended version of the program POISSON [78]. In addition to the standard option for drawing equipotential lines, the extended version offers also the possibility to draw field lines [79]. In the calculations neither diffusion nor magnetic fields were taken into account. In figure 6.3 the calculated transfer efficiency curve for the geometry shown in figure 6.2a can be compared with the measured one. The agreement for $\Delta U < 0$ is satisfying, whereas for $\Delta U > 0$ there is some

difference.

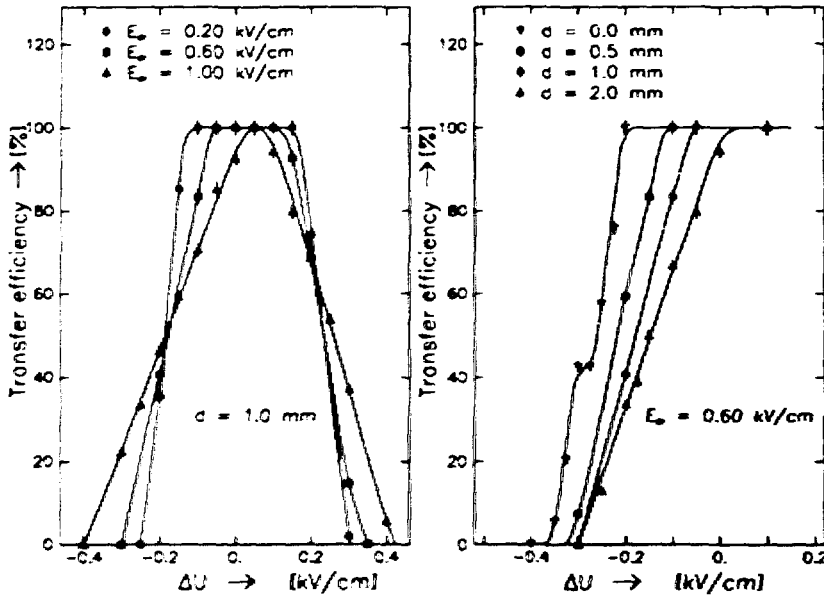Figure 6.4: Calculated transfer efficiency curves for the wire chamber shown in figure 6.2a: (a) for three field strengths (d=1mm); (b) for four distances between the gating planes (E_d=0.60 kV/cm).

When the chamber is gated two equal pulses of opposite polarity are applied to the wire planes G_1 and G_2 in order to switch the chamber from closed to open. To minimize the dead-time in the electronics due to pick-up of these signals, the size of the pulses has to be kept as low as possible. This makes the left side of the gating curve (ΔU <0) more advantageous for gating since it is steeper than the right side (ΔU >0). From figure 6.3 it can be concluded that on the left side the pulses necessary to switch are +75 V and -75 V whereas on the right side the pulses have to be: +125 V and -125V.

The data in figure 6.3 are valid for a drift field of 0.20 kV/cm only. In figure 6.4a three calculated gating curves are shown, demonstrating the influence of the field strength in the drift tube on the electron transfer efficiency. The voltages are again as shown in figure 6.2a. Increasing the drift field diminishes the size of the full transfer plateau and increases the size of the pulses necessary to switch the gating between open and closed. The values of these voltages are listed in table 6.1.

The BRICH will be operated with a drift field of about 0.60 kV/cm, requiring two pulses of +125 V and -125 V for a distance d between the two gating planes of 1 mm. In the presence of a magnetic field the pulses necessary to switch between open and closed are even bigger (see next section) motivating a search to minimize these pulses.

d	E_{dr} [kV/cm]		
[mm]	0.20	0.60	1.00
2.0		350	
1.0	150	250	470
0.5		225	
0		175	

Table 6.1: The voltage difference ΔU [V] necessary to switch the chamber between open and closed for different values of the drift field E_{dr} and the distance d between the gating planes (in absence of a magnetic field).
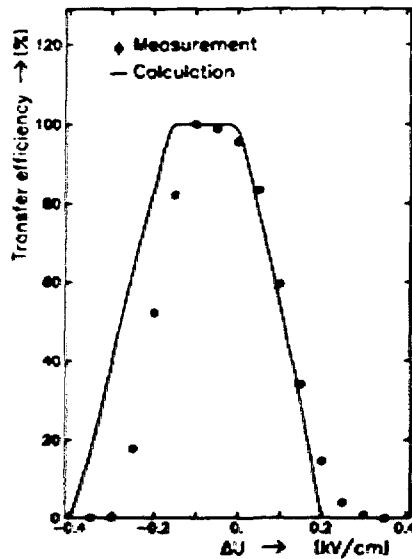
Figure 6.5: Measured and calculated transfer efficiency of the final configuration of the gating system (E_{dr}=0.60 kV/cm; B=0 T).

Figure 6.4b illustrates the influence of the distance d between the gating grids on the steepness of the gating curve. The position of grid G_1 was kept constant and that of G_2 was varied. Only the left sides of the curves are shown; they are calculated for a field strength of 0.60 kV/cm. The voltages necessary to switch from closed to open are indicated in table 6.1. Apparently the best solution is obtained when the two groups of gating wires are in one plane. This has been implemented in the final design shown in figure 6.2b, where the new setting of the voltages is indicated as well. A gating curve measured with this configuration is compared with a calculation in figure 6.5. At ΔU=0 V, the chamber is not

fully efficient; maximum transfer now occurs at ΔU=-100 V. The electron loss at ΔU =0 V is measured to be $(4.5\pm0.8)\%$.

6.3   Reprint: Gating the MWPC's of the DELPHI barrel RICH

GATING THE MWPCs OF THE DELPHI BARREL RICH

G. VAN APELDOORN, D. LANGERVELD and D.Z. TOET

NIKHEF-H, Amsterdam, The Netherlands

D. BLOCH, M. DRACOS, W. DULINSKI *, D. HUSSON, P. JUILLOT, D. LOUKAS,
M. SCHAEFFER, E. ARIA, J.D. BERST, E. CHRISTOPHEL, J.P. FROBERGER and N. MAYET

CRN and Université Louis Pasteur, Strasbourg, France

The gating system of the MWPCs of the DELPHI Barrel RICH is essentially a means to prevent positive ions originating from avalanches in the chambers to escape into the Barrel RICH drift tubes. These ions would otherwise seriously affect the imaging quality of the Barrel RICH. We describe the gating grid, the gating pulser and results of tests at pressures of 1 and 1.3 bar in a magnetic field of 1.2 T and without. In the ungated ("closed") mode, transfer of electrons and ions are 8% and 0% respectively, a farther reduction of electron transfer is limited by power dissipation of the pulsing circuit. The occupation time of the readout electronics after the gating pulse is less than 1 µs. The test results are compared with those of electrostatic simulations. A triggering scheme is proposed.

1. Introduction

One of the well-known and important characteristics of the DELPHI spectrometer is the use of the ring-imaging Cherenkov (RICH) technique to assist in particle recognition [1]. In a photosensitive gas the Cherenkov photons liberate electrons which are drifted towards an efficient, fine-grained, high-gain MWPC [2] in an electric field of high homogeneity such as not to distort their original configuration

The high gain of the chamber [(2–3) × 10^5] implies that each photo- or ionization-electron gives rise to a large amount of ions. Their drift is relatively slow and they represent a space charge, which has been shown to seriously affect the homogeneity of the drift field, thus causing large distortions of the Cherenkov ring images [3]

In order to reduce the ion space charge by as much as possible, we have provided our MWPCs with a gating system. This gives us control over the admittance of electrons to   and the escape of ions from   the chamber. Even when the chamber has been "open" for ~ 30 µs to collect all electrons arriving from up to 1.5 m distance from the chamber in the case of an "interesting" event (trigger), the earliest created ions will not have moved beyond the gating wire grid because of their low mobility, and will be largely absorbed by it after the chamber has be electrostatically "closed".

In this paper we discuss the performance and some mechanical and electronic features of the gating system

on our chambers. Test results will be reported and compared to those of electrostatic simulation.

2. The MWPC and the grating grid

We recall the main features of our MWPC, for a full description, we refer to [2]. Each MWPC contains 128 sense wires and 128 cathode strips (see fig. 1). Between the sense wires one finds blinds   equipped with HV strips   which serve to reduce cross-talk between wires due to photoelectrons created by secondary photons radiating from the avalanches. The opening of the drift tube at the chamber side is 5.25 mm above the gating wire plane. The gating grid is thus situated at the transition between the drift tube and the chamber and forms part of the chamber construction. It both terminates the drift-tubes' field-shaping system, governing the quality of the field in the transfer region, especially near the chamber boundaries [4,5], and controls the accessibility of the chamber for electrons.

The gating grid consists of two types of wires, situated a few millimeters away from the blinds. The wires just above the blinds (type G_1) are powered separately from those above the middle of the cells (type G_2). Depending on the choice of the voltages, electrons are either focalized into the cells (chamber "open") or onto the gating wires (G_1 or G_2 chamber "closed"). These situations are depicted in fig. 2.

We have tested the performance of several gating grid configurations [2,3]. Electrostatic simulation [4] using the program POISSON [6] extended with electron

* Visitor from INP, Cracow, Poland

tracking indicated the feasility of a grid with G_1 and G_2 in one plane. These results have been checked with a program incorporating magnetic field effects (see section 3). The above results, together with the requirement of construction simplicity, led to the choice of a flat gating grid. We have tested a flat gating grid consisting of 40 μm gold-plated tungsten wires at 3 mm above the cloisons (fig. 1) as will be described in the next sections.

3. Static gating

With "static gating" we designate the study of the transfer efficiency of electrons from the drift tube to the chamber as a function of the (static) voltage difference $\Delta V_G = |V_{G_2}| - |V_{G_1}| = V_{G_2} - V_{G_1}$, after having optimized the electron optical potentials at the entrance of the cells for maximal electron transfer in the open situation [4]. In the following tests and simulations the drift field strength corresponds to 0.60 kV/(cm bar), while the value of the magnetic field is 1.2 T, as planned for the experiment. Also tests at zero magnetic field have been done.

In the DELPHI spectrometer the B-field is parallel to the drift tube axis and consequently in the drift tubes the E-field is (anti-)parallel to the B-field. However, in certain regions like the transfer region between tube and chamber, near the gating and sense wires, the E-field develops components perpendicular to B, giving rise to a Lorentz force on drifting charged particles.
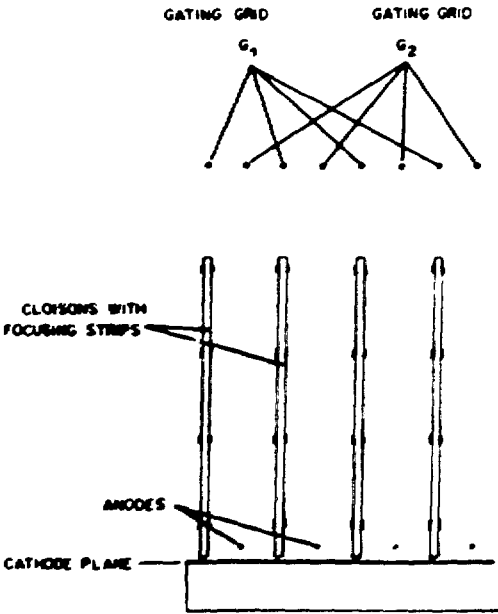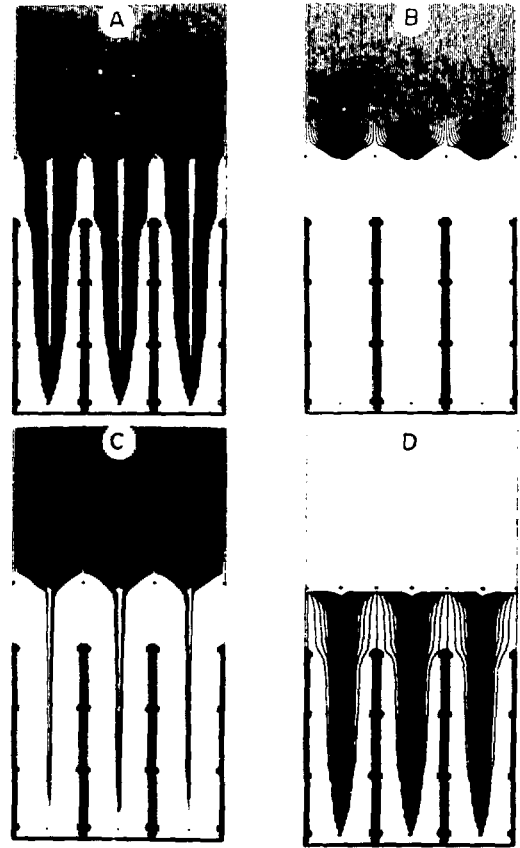

Fig. 2. Simulated electron and ion trajectories at some gating voltages and magnetic fields as a function of gating voltages and magnetic field: (A) $B = 0$ T, $\Delta V_G = -50$ V, chamber "open"; (B) $B = 0$ T, $\Delta V_G = -200$ V, chamber "closed"; (C) $B = 1.2$ T, $\Delta V_G = -200$ V; chamber "leaking" (electrons); (D) $B = 0$ T, $\Delta V_G = -200$ V, ion trajectories.

Fig. 1. The MWPC

The mobility of the ions (and consequently their drift velocity) is about four orders of magnitude smaller than that of electrons. For our gas mixture (75% CH_4 + 25% C_2H_6) the value of the electron mobility can be calculated from the drift speed quoted in ref. [3]: $v_d^e = 6.3$ cm/μs at 580 V/cm, giving $\mu^e = 1.09 \times 10^4$ cm^2/(V s). From ref. [7] we can infer a value of μ^{ion} around 2.0 cm^2/(V s).

The influence of the Lorentz force is consequently much less pronounced for ions than for electrons (see e.g. ref. [8]); ions are hardly affected by the magnetic field. The electrons however, at $B = 1.2$ T, are much less focused by an electric field component perpendicular to the magnetic field than at $B = 0$, thus showing a tendency to "better follow the B-direction". A stronger gating potential gradient is thus needed to close the chamber for electrons.

Table 1

Static gating test with the flat gating grid; chamber voltage settings for an electrostatically "open" chamber at $B = 1.2$ T for $P_{abs} = 1.3$ and 1.0 bar. $E_d = 0.6$ kV/(cm bar)

Absolute pressure [bar]	Chamber voltages [– kV] ($V_{anode} = 0$ V)							
	Cathode	Voltages on the blinds				Gating grid		
	V_{cath}	V_{S_1}	V_{S_2}	V_{S_3}	V_{S_4}	V_{G_1}	V_{G_2}	V_G
1.3	1.6	2.2	2.85	3.5	4.15	4.6	4.5	4.55
1.0	1.5	2.0	2.5	3.0	3.5	3.95	3.85	3.9

Table 2

Summary of static gating test results for the flat gating grid. $B = 1.2$ T and 0 T; $P_{abs} = 1.3$ and 1.0 bar. $E_d = 0.6$ kV/(cm bar)

Magnetic field [T]	Absolute pressure [bar]	Gating grid voltages			Required gating pulse × 2 [V]
		V_G [– V]	ΔV_G [V]		
			open for electrons	closed for electrons	
1.2	1.3	4550	– 100	– 530	430
1.2	1.0	3900	– 100	– 500	400
0.0	1.3	4550	– 50	– 360	310
0.0	1.0	3900	– 50	– 390	340

3.1. Static gating tests results, simulations, conclusions

To investigate the gating behaviour of the chamber in a magnetic field of 1.2 T at pressures of 1 and 1.3 bar, we inserted the chamber in a small "pressure-proof" volume, made in Strasbourg, with a drift space of 2 cm, equipped with quartz windows. We used a pencil beam from a nitrogen laser developed and built in Amsterdam [9] to create photoelectrons in the drift gas (two-photon process, $\lambda = 337$ nm). The volume was put between the poles of a conventional C-magnet.

Voltage settings on cathode, blinds and gating grid depend on the pressure; they can be found in table 1. With these settings one finds a 100% transfer plateau for ΔV_G values from – 100 V to + 50 V or beyond.

This is one of the results obtained by a study of the acceptance of the chamber as a function of ΔV_G, changing both voltages V_{G_1} and V_{G_2} with equal but opposite steps, thus keeping $V_G = (V_{G_1} + V_{G_2})/2$ constant. These results are presented in fig. 3; a summary of relevant static gating results can be found in table 2.

For the electrostatic simulation of the above test results we have used a program developed at Strasbourg [10], which incorporates the effects of the magnetic field. The sequence of fig. 2 illustrates the simulated change of the electron acceptance. The results are also given in fig. 3 where they can be compared with measurements. The agreement is excellent.

From the static gating results, one can determine the voltage differences that dynamic gating pulses have to bridge between "closed" and "open" in future experimental circumstances; this is an important datum for the design of the gating circuit. These voltage differences are given in table 2; they correspond in fact to twice the absolute value of each of the gating pulses on G_1 and G_2 to be delivered by the gating circuit.

It follows from section 3 that the curves measured for $B = 0$ (e.g. fig. 3b) can be regarded as representative for the behaviour of ions at $B = 1.2$ T. For gating
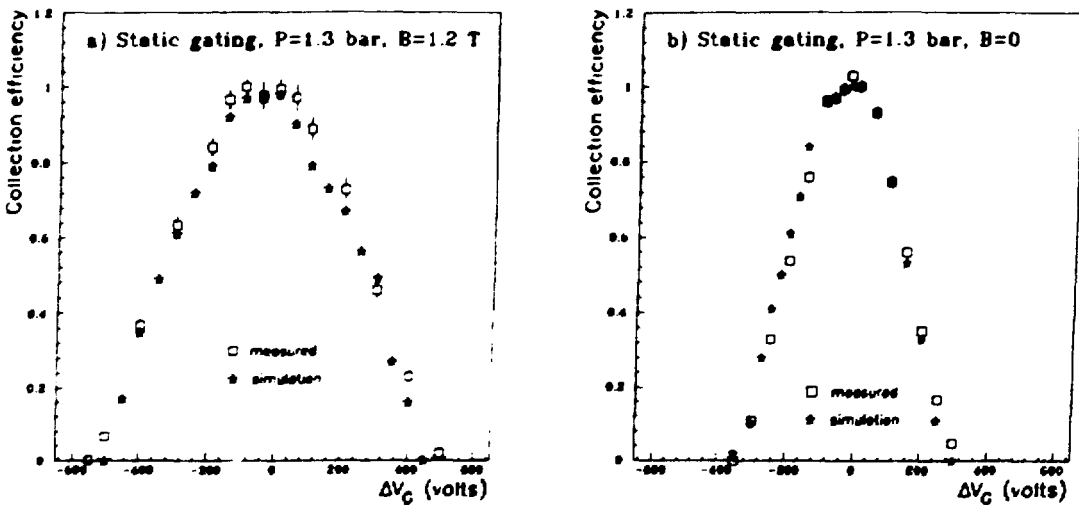

Fig. 3. Static gating with the flat grating grid ($P_{abs} = 1.3$ bar, $\Delta V_G = V_{G_1} - V_{G_2}$), see tables 1 and 2 for chamber voltages; (a) $B = 1.2$ T. (b) $B = 0$ T.

voltage differences where electrons begin to leak into
the chamber at $B = 1.2$ T, ions are still unable to escape
from the cells.

4. Dynamic gating

Under experimental circumstances, in the absence of
a trigger, our chambers are "closed" to avoid any
unnecessary production of ions. In this way one also
slows down the process of ageing [11]. When a trigger
arrives, the gating circuit opens the chamber long enough
to gather all relevant data (dynamic gating).

Dynamic gating has to meet the following criteria:

The chamber, when gated, should be fully accessible
for electrons during at least the maximal drift time
(~ 32 µs).

The effect of gating pulse switching (saturation of the
readout electronics) on data collection should be
minimized.

Gating should be able to keep up with the triggering
rate.

The gating circuit (fig. 4), developed and built at
Strasbourg, is coupled to the high-voltage input of each
wire plane G_1 and G_2 via a HV capacitor. This capaci-
tor is of special quality in order to avoid piezoelectric
effects. In the quiescent state these capacitors are
powered at the gating circuit side with -200 V and
$+200$ V respectively (250 V maximum). Upon arrival
and for the duration of the input pulse, which is de-
livered by a pulse generator when fired by the trigger,
both voltages are pulled down to zero by VMOS-tran-
sistors. At the end of the input pulse the circuit returns
to its quiescent state. This results in a positive and
negative pulse on G_1 and G_2 respectively, of 200 V
amplitude and with a length equal to that of the input
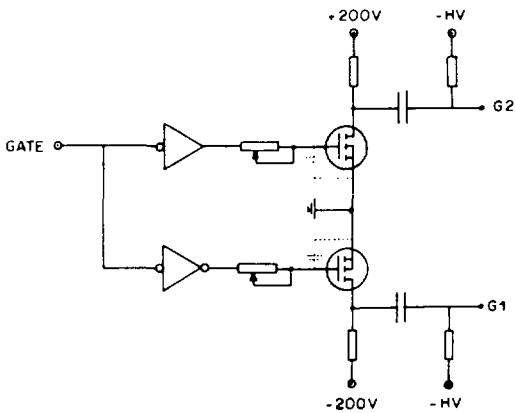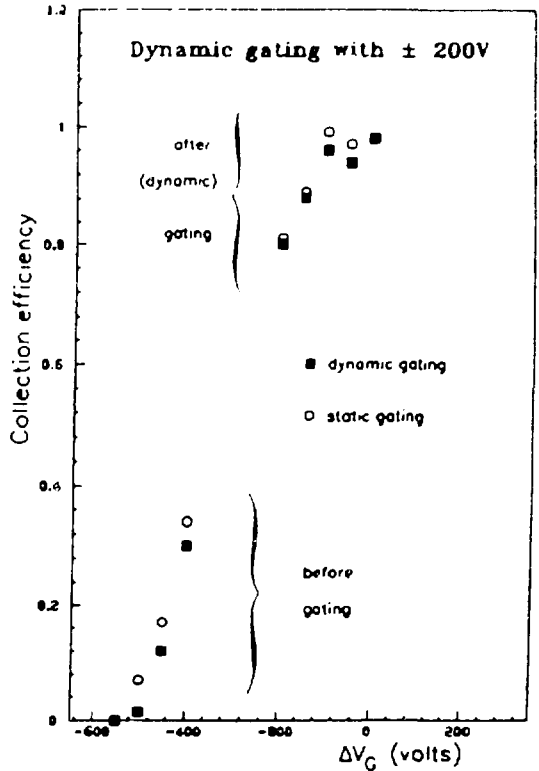pulse. The rise time of these pulses can be set between
100 ns and 1 µs.

Fig. 5. Dynamic gating results at $B = 1.2$ T, $P_{abs} = 1.3$ bar.
Transfer of electrons in the gated and ungated mode; the
results of static gating are given for comparison.

The readout electronics will be saturated at both
switching edges of the gating pulses. In order to mini-
mize this, the signals have to be symmetrized and oscil-
lations eliminated. Stray capacitances both in the cham-
ber and in the circuit play a role and for this reason
each chamber will be equipped with its own "individu-
ally adjustable" gating circuit. One arrives at saturation
times of ~ 1 µs ($\sim 6-7$ cm drift).

4.1. Dynamic gating tests results

Fig. 5 shows the effects of dynamic gating with
pulses of $+$ and -200 V for different starting (chamber
"closed") values of ΔV_G ($B = 1.2$ T and $P_{abs} = 1.3$ bar).
For comparison, static gating resuls are also represented
in these figures; the agreement is satisfactory. Concern-
ing the dependence of the (gated) transfer efficiency on
the delay between the gating trigger and the arrival of
the electrons, one finds that this efficiency is 100% for
delays of 1 µs or longer.

The above mentioned dynamic gating results at $B =$
1.2 T show that at $P = 1.3$ bar the chamber is "open" at

Fig. 4. The gating pulser, functional diagram.

ΔV_0 around -100 V in accordance with the static-gating result. If gating is done with ± 200 V pulses, the chamber should thus not be "closed" at ΔV_G values exceeding -500 V. Electron leaking at these values is around 8% or less, ions however are completely absorbed as one can conclude from fig. 3b.

5. Triggering

Waiting for an event trigger to "open" the chamber unavoidably leads to information loss (to which has to be added the loss due to the gating pulse saturation). The estimated gating frequency in this case would be around 1 kHz (asynchronous trigger).

The scheme adopted is to gate the chambers just before (~ 1 μs, to absorb the gating switch-on) each bunch crossing (synchronous trigger), i.e. at 44 kHz, and close them again if no event trigger arrives, i.e. some 2 μs after the bunch crossing. At this rate however, power dissipation in the gating circuit limits the amplitude of both pulses to around 200 V.

6. General conclusions

We have developed a dynamic gating system for the MWPCs of the RICH barrel and successfully tested it in a magnetic field of 1.2 T. When using synchronous triggering, the collection efficiency for useful photoelectrons is not affected by saturation of the readout during switching. Ions, however, are prevented from entering the drift volume, where they would otherwise affect the homogeneity of the electric field and give rise to serious Cherenkov ring image distortions. To avoid this was precisely the reason for developing the gating system.

Acknowledgments

References

[1] DELPHI Technical Proposal, CERN/LEPC/83-3 (1983); Barrel RICH Construction Group, The DELPHI Barrel RICH, Addendum to the Technical Proposal, CERN/LEPC/86-11 (1986).

[2] D. Bloch et al., Nucl. Instr. and Meth. A273 (1988) 847.

[3] R. Arnold et al., Nucl. Instr. and Meth. A270 (1988) 255. P. Baillon, H.J. Besch, E. Christophel, P. Pétroff, J. Séguinot, D. Toet and T. Ypsilantis RICH 10, DELPHI Report 85-99 (1986).

[4] D. Langerveld, Thesis, University of Amsterdam (1989) in preparation.

[5] P. Coyle and P. Rensing, Report SLAC Memo (November 1986).

[6] R.F. Holsinger and C. Iselin, CERN Long Write-Up T604 (1982, rev. 1984).

[7] F. Sauli, CERN Yellow Report 77-09 (1977); J. Fehlmann and G. Viertel, Compilation of Data for Drift Chamber Operation (ETH Zurich, 1983).

[8] J. Kent, LPC 84-17 (1984).

[9] F. Hartjes, J. Konijn and Y. Peng, Nucl. Instr. and Meth. A269 (1988) 544.

[10] D. Husson, Thèse, Université. Louis Pasteur, Strasbourg, CRN-HE 88-02 (1988).

[11] D. Langerveld, D.Z. Toet and W. Dulinski, Internal note Barrel RICH Construction Group (09/11/87); J. Va vra, SLAC-PUB-4116 (1986); J. Va'vra, CRID MEMO no. 36 (1987).

Chapter 7

Electron drift over long distances

7.1   Introduction

One of the exceptional ideas in the design of the barrel RICH detector is the drift of single electrons over distances up to 1.5 m and the collection of information about the coordinates of the photon conversion points by recording the coordinates of these electrons after such a long drift. Preferably the accuracy of the reconstruction should be ≈ 1 mm for each coordinate.

In this chapter a study is presented of the problems connected with electron drift in the long drift tubes of the BRICH. The study was performed in a setup called SYBIL, described in the next section. Parts of the results were published before [80].

The feasibility of electron drift over long distances has been shown by Barrelet et al. [15] and Arnold et al. [19], providing that all dielectric walls around the drift volume are covered with field shaping electrodes both on the inside and on the outside. In the BRICH drift tubes this is realized with thin metallic strips deposited with a pitch of 3 mm on all sides of the quartz plates that constitute these tubes.

Arnold et al. [19] extensively report on distortions in the electron drift, measured with and without the use of a gating system. Since distortions complicate the relation between real and measured coordinates of the photo-conversion points, they should be as small as possible. In section 7.5 it is shown that this can be achieved except for small regions close to the quartz walls. Each drift tube is equipped with a calibration system that offers the possibility of quantitatively monitoring these distortions, so they can be corrected for.

For the functioning of the BRICH it is of crucial importance that the electron loss over the long drift paths in the tubes is small. An attenuation length of at least 10 m is required; a mean electron loss of 7% would thus be considered acceptable. An attenuation length better than 10 m has been achieved by Arnold et al. [81]. In section 7.4 a systematic study of the attenuation length as a function of the TMAE temperature is presented. The temperature of the TMAE bubbler in the BRICH will be 30°C.

The SYBIL setup offers an excellent possibility of measuring drift velocities and diffusion. Because of the long drift distances this can be done with high accuracy. A special

advantage is the possibility of recording data for both the longitudinal and the transverse diffusion in the same measurements.
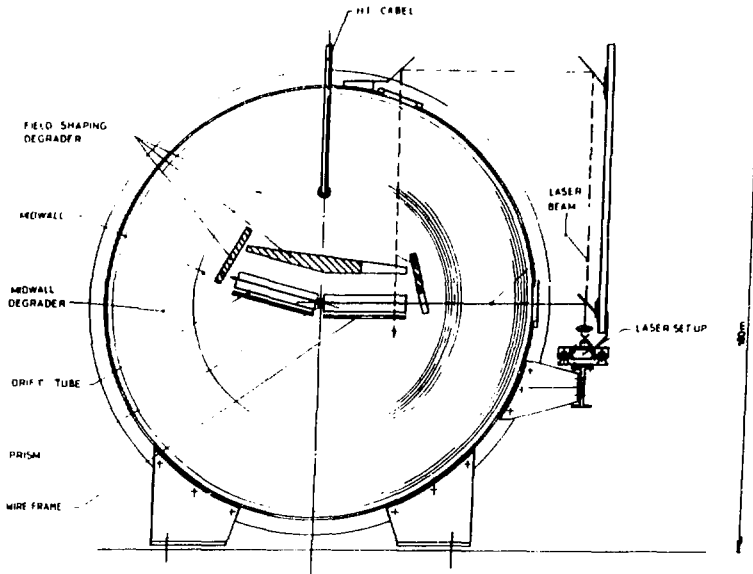

Figure 7.1: An overview of the SYBIL setup. The laser beam can be shot into the bitube both in the horizontal and in the vertical direction.

7.2   SYBIL, the experimental setup

SYBIL (SYstem for testing BItubes with Laser ionization) is a setup (figure 7.1) to test all bitubes before installation into the BRICH. It consists of an aluminium cylinder (length 3 m, diameter 1.8 m) at the centre of which a bitube can be placed. Perpendicular to the axis in the middle of the cylinder an electrically insulated aluminium plate is installed that supports the bitube at its end and connects it to high voltage. A circular degrader is integrated in the mid-wall to obtain a well defined potential gradient from the grounded vessel to the aluminium plate in the centre. The power supply (Heinzinger) can produce up to -150 kV. The bitubes are fixed to the front flange of SYBIL in exactly the same way as on the BRICH end flanges.

To simulate the electrostatical environment of the BRICH the bitube is surrounded by structures covered with electrodes. A dummy liquid radiator is positioned above the bitube. On the left and right side bars are mounted simulating the presence of adjacent bitubes. Two wire frames, mounted on the bitube, cover the bottom side; i.e. this is the side looking towards the mirrors in the BRICH. Distortions in the electric field are avoided

by applying on the electrodes and wires of all these structures the same voltages as on the corresponding strips of the drift tubes.

The drift gas consists of methane and ethane with a small TMAE admixture. Prior to entering the TMAE bubbler, the gas mixture flows through an absorber (Oxisorb, Messer Griesheim) that lowers both the oxygen and the water concentration below 0.1 ppm. The bubbler is immersed in a temperature controlled water bath; it can be bypassed as well. The gas system offers the possibility of selection which drift tube is input and which drift tube is output for the gas flow. The bitube can be bypassed if needed.

To avoid TMAE oxidation products several measures have been taken. Before use the TMAE is cleaned thoroughly. The input gas is cleaned from oxygen and water contaminations before contact with the TMAE. The tubing from the absorber via the bubbler to the drift tubes was originally made out of copper but later changed to stainless steel because this shows less outgassing. At the drift tube gas outlet the oxygen concentration is continuously monitored (Teledyne Analytical Instruments). TMAE was added to the drift gas only when the oxygen level was better than approximately 1 ppm.

The SYBIL cylinder wall has 5 windows on the side and 5 on the top, enabling measurements at different drift distances both with a horizontal and a vertical N_2 laser beam (figure 7.1). On corresponding positions holes were made in the side bar and the dummy liquid radiator to let the laser light through. The laser with its optics can be moved from window to window on a rail. This allows measurements at different drift distances without changing the optics itself and thus with identical power density in the laser beam. A computer controlled motor can displace one mirror in the optics over a distance of 7 cm with an accuracy of 2 μm, offering the option of making automatic scans.

The wire chamber is described in section 5.5.1. Unfortunately, due to lack of the appropriate electronics, the gating system could not be used. The electronics chain, consisting of preamps, shapers and TDC's is as described in section 5.5.2. The data acquisition is controlled from a MacIntosh Plus computer equipped with the MacPlinth Camac interface. The on-line software commands the firing of the laser, reads out the TDC's and stores the data either in histograms or directly onto the hard disk [82].

7.3 Drift velocity and diffusion measurements

The long drift distance and the high position resolution make the SYBIL setup a powerful tool for measuring drift velocities and diffusion coefficients. Here we report on measurements made in two methane-ethane gas mixtures (80% - 20% and 50% - 50%) for four field st.engths. During the measurements traces of TMAE were added to the drift gas (concentration $\approx$10 ppm) to increase ionization by the laser light. At that time it was impossible to work with higher TMAE concentrations due to corona. The photons of these discharges are converted by the TMAE, causing a disturbing background.

The measurements were performed with a vertical laser beam through the drift tube, i.e. the beam was in the y-direction along the anode wires. The laser intensity was adjusted such that only in about 15% of the laser triggers one or more free electrons were created. By recording the electron drift time distribution as a function of the drift distance z both the drift velocity and the longitudinal diffusion are obtained. By recording the distribution of the number of events over the wires the transverse diffusion is obtained.
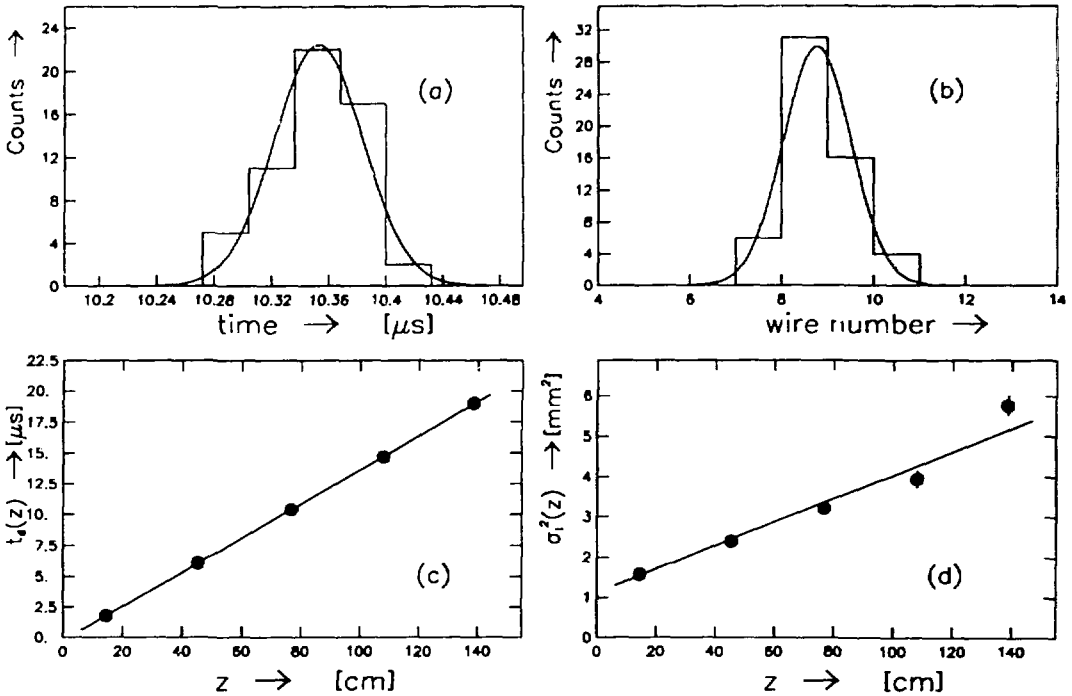
Figure 7.2: Four illustrations of drift velocity and diffusion measurements (U_{HV}=-80 kV; 80% methane and 20% ethane): (a) a time distribution measured for z=77 cm, with the gaussian fit through the data; (b) the wire distribution of the same measurement with its gaussian fit; (c) the drift time versus the z-coordinate; (d) the square of the longitudinal diffusion versus the z coordinate.

At each window we performed a set of measurements at 21 regularly spaced x-coordinates. This was done since the measurements were also meant to study distortions close to the side wall. Each measurement consisted of 500 laser shots. For each of the 21 measurements a least square fit was made of a gaussian distribution to each of the two registered distributions. As an example a time distribution is shown in figure 7.2a and a wire distribution in figure 7.2b together with the gaussian fits. The fits were calculated with the program

MINUIT [76].

The result of a fit through the drift time distribution of measurement i is the mean drift time $t_i(z)$ with its error Δt_i and the variance $\sigma_{d,i}(z)$ with its error $\Delta\sigma_{d,i}$. The subscript d is used since $\sigma_{d,i}(z)$ indicates the variance of the *drift time* distribution. In each set of 21 measurements some fits to data taken close to the side wall were obviously wrong: those were omitted. From the remaining results the drift time $t(z)$ with its error Δt and the variance in the drift time $\sigma_d(z)$ with its error $\Delta\sigma_d$ are calculated.

To the statistical error in the drift time calculated this way a systematic error of 0.3% is added to account for variations in the gas mixture, the room temperature and the atmospheric pressure.

After repeating this procedure for all windows the drift velocity w is obtained by making the fit:

$$t(z) = \frac{1}{w} \cdot z + t_0 \qquad (7.1)$$

where t_0 is a constant. An error on the position z of 1 mm has been supposed. An example of a fit is shown in figure 7.2c. In table 7.1 the drift velocities are listed with their errors.

methane-ethane concentration [%]	U_{HV} [kV]	E_{dr} [V/cm]	w [cm/μs]	σ_{0l} [μm/$\sqrt{cm}$]	σ_{0t} [μm/$\sqrt{cm}$]
80-20	-100	675	7.868±0.020	160±4	191±4
80-20	-80	535	7.239±0.018	170±4	205±3
80-20	-60	394	6.163±0.015	203±4	212±4
80-20	-40	254	4.416±0.011	291±6	234±4
50-50	-100	675	6.131±0.018	146±4	209±5
50-50	-80	535	5.720±0.017	157±5	210±5
50-50	-60	394	4.990±0.015	176±6	214±5
50-50	-40	254	3.831±0.011	247±7	236±6

Table 7.1: Drift velocity w, longitudinal diffusion coefficient σ_{0l} and transverse diffusion coefficient σ_{0t} measured for 2 methane-ethane gas mixtures and 4 values of the high voltage U_{HV}; also the corresponding field strengths E_{dr} are shown (T=20°C; p=1 bar).

The spatial variance $\sigma_l(z)$ is obtained by multiplying the variance in the drift time with the drift velocity:

$$\sigma_l(z) = w \cdot \sigma_d(z) \qquad (7.2)$$

$$\Delta\sigma_l = w \cdot \Delta\sigma_d \qquad (7.3)$$

The longitudinal diffusion coefficient σ_{0l} is obtained by making the fit (compare with equation 3.9 and proceeding text):

$$\sigma_l^2(z) = \sigma_{0l}^2 \cdot z + \sigma_0^2 \qquad (7.4)$$

where σ_0 is a constant that accounts for the width of the laser beam and the diffusion in the wire chamber. An example of such a fit is shown in figure 7.2d. The results are listed in table 7.1.

The transverse diffusion coefficient σ_{0t} is calculated from the wire distribution in an analogue way. The mean of each fitted distribution is the laser position (x-coordinate) as measured after the drift distance z; the variance of the distribution is a measure of the diffusion. After averaging over the 21 fits we obtain the variance $\sigma_t(z)$ with the error $\Delta\sigma_t$. Then the result of the fit:

$$\sigma_t^2(z) = \sigma_{0t}^2 \cdot z + \sigma_0^2 \qquad (7.5)$$

gives the transverse diffusion coefficient σ_{0t} with its error; σ_0 is a constant that accounts for the width of the laser beam and the resolution of the wire chamber. The results are listed in table 7.1.

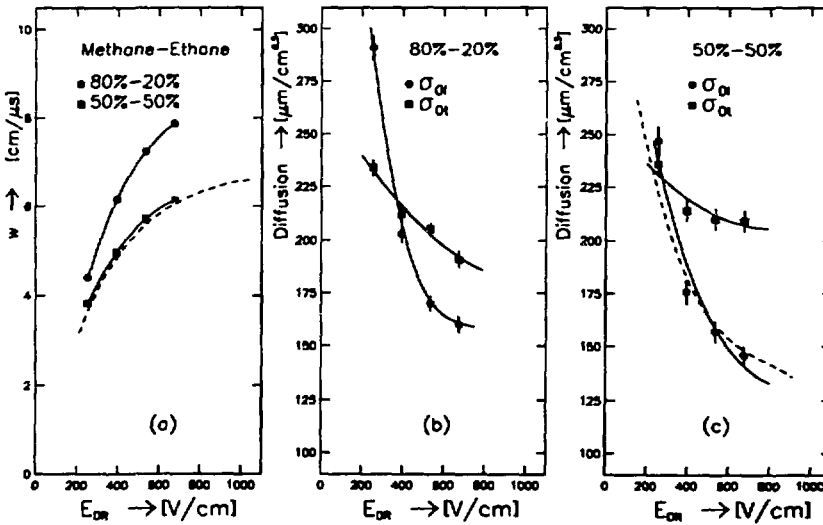The measurements have been performed with voltages U_{HV} on the end of the drift tube

Figure 7.3: As a function of the drift field are shown: (a) the drift velocity in two methane-ethane gas mixtures; (b) the longitudinal and the tranversal diffusion coefficient in the 80-20 gas mixture; (c) idem for the 50-50 mixture. The solid curves are drawn to guide the eye. The dashed curves are from Jansen [50].

of -100 kV, -80 kV, -60 kV and -40 kV. The corresponding field strengths listed in table 7.1 have been corrected for the voltage on the chamber, the pressure and the temperature.

The measured drift velocities are shown in figure 7.3a. The dashed curve is a measurement of the drift velocity in 50% methane - 50% ethane gas mixture by Jansen [50]. The small difference between our measurement and his is most likely due to an uncertainty in the composition of our gas mixtures. The methane and ethane gas flows are both measured with Vögtlin V100-300 flow meters. Although the meters have been calibrated we estimate the uncertainty in the composition of the 50-50 gas mixture to be 3%.

The two diffusion coefficients are shown for the 80-20 gas mixture in figure 7.3b and for the 50-50 gas mixture in figure 7.3c. Also the longitudinal diffusion coefficient measured by Jansen [50] for a 50-50 mixture is shown.

The fact that the longitudinal diffusion coefficient is bigger than the transverse diffusion coefficient for low fields but smaller for high field strengths has also been observed by Wong et al. [84] for argon-methane gas mixtures.

7.4   The electron attenuation length

The method used for measuring the electron attenuation length λ essentially consists of counting the number of events, with electrons recorded by the wire chamber, as a function of the drift distance z. The measurements are performed with a horizontal laser beam i.e. perpendicular to the anode wires. In order to avoid systematic errors a series of measurements is done, going from window to window in a certain order; for the next series this order is then inverted. At each window a short measurement is done, consisting of 500 laser shots. Finally at all 5 windows the same number of laser shots are recorded. In this way systematic variations in the conditions are in first order compensated. Examples of variations are: shifting of the laser power, changes in the temperature of the TMAE bubbler or the room temperature, etc.

An exponential curve is fitted to the number of counts as a function of the drift distance:

$$N(z) = N_0 \exp{-\frac{z}{\lambda}} \qquad (7.6)$$

$N(z)$ is the number of counts recorded when the laser is positioned at the drift distance z; N_0 is a constant. Two results are shown in figure 7.4. It shows that the setup is capable of measuring attenuation lengths of order of magnitude of 1 m with high accuracy; for attenuation lengths largely exceeding the length of the drift tube small systematic errors limit the accuracy. More statistics does not improve the result. Examples of these errors are differences in the transmission of the quartz windows and the positioning of the laser beam between the (opaque) electrodes on the drift tube.

The electron loss is proportional to the concentration of the electronegative impurities.
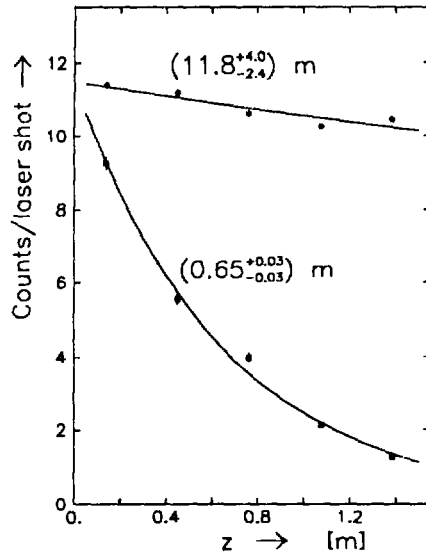
Figure 7.4: Two examples of electron attenuation length measurements in drift gases containing TMAE vapour; statistical errors indicated.

If the concentration of some of these impurities is proportional to the TMAE concentration, the relation between the measured attenuation length λ and the TMAE vapour pressure p_{TMAE} can be written as:

$$\frac{1}{\lambda} = c \cdot p_{TMAE} + \frac{1}{\lambda_0} \tag{7.7}$$

where λ_0 contains the contribution of those electronegative impurities that are independent of the TMAE vapour pressure; c is a constant.

A reason for the concentration of some impurities to be proportional to the TMAE vapour pressure could be that they are produced by reactions of TMAE with oxygen or construction materials; alternatively they could be present in the TMAE liquid.

	TMAE	TMU	TMO
uncleaned TMAE	97.47	1.22	0.27
distilled TMAE	99.74	0.19	0.04
water washed and distilled TMAE	99.96	0.03	0.01

Table 7.2: The percentages of TMAE, TMU and TMO concentrations in three TMAE samples [83].

Three differently cleaned TMAE samples have been used for attenuation length mea-

surements. The possible cleaning methods are listed in section 4.4. The concentrations
in the three samples of the two major oxidation products TMU and TMO are shown in
table 7.2. As mentioned in section 4.4 these two impurities are strongly electronegative.
With each sample the attenuation length has been measured for several TMAE bubbler
temperatures. The vapour pressure is calculated from the temperature with equation 4.2
using the values for the constants found by Giomataris *et al.* [58].

The first TMAE sample was not cleaned. Its attenuation length has been measured
for 4 temperatures. In figure 7.5a the inverse of the attenuation length is plotted against
the TMAE vapour pressure. As expected from equation 7.7 a linear relation is observed.
An extrapolation to a TMAE temperature of 30°C gives an attenuation length of 16 cm;
almost 2 orders of magnitude too low.
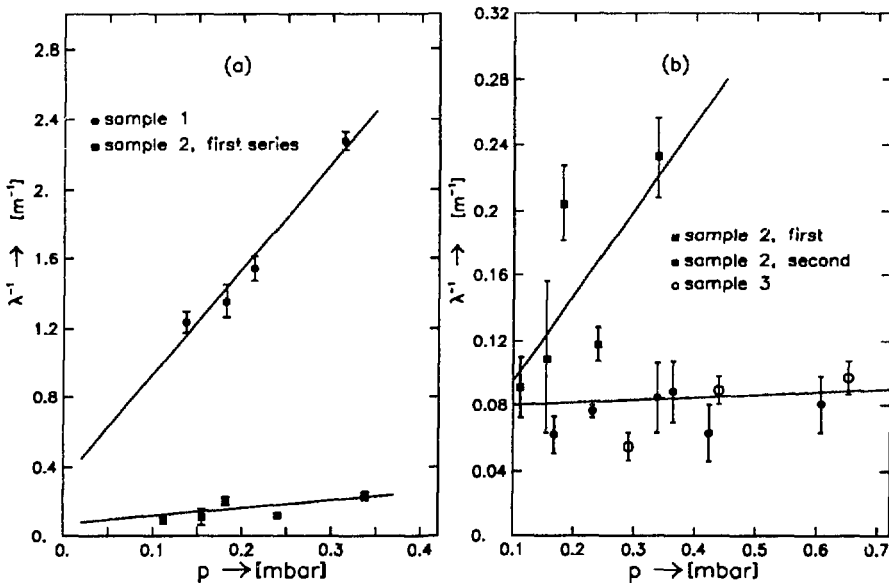
Figure 7.5: The inverse attenuation length as a function of the TMAE vapour
pressure for: (a) TMAE sample 1 and the first series of measurements with
TMAE sample 2; (b) TMAE sample 2 (two series) and sample 3.

The second TMAE sample has been cleaned by vacuum distillation. With this sample
two series of measurements have been performed. Both series are shown in figure 7.5b.
The first series shows again a linear relation between the TMAE vapour pressure and the
inverse of the attenuation length. Comparison with the first TMAE sample in figure 7.5a
shows the improvement due to the cleaning of the TMAE. The extrapolated attenuation
length at 30°C is 1.7 m.

Before the second series of measurements was started the gas system was modified.
All copper tubing was replaced by stainless steel and a small leak was found and repaired.

After these modifications clean gas was flushed through the TMAE bubbler during about a month. This might have improved the quality of the TMAE (cleaning method 4 mentioned in section 4.4).

The attenuation lengths found for the second series are practically independent of the TMAE vapour pressure. The extrapolated value for 30°C is 10 m.

The third TMAE sample has been cleaned by water washing and vacuum distillation. With this double cleaning procedure a further improvement of the TMAE purity is obtained (table 7.2). The electron attenuation length has been measured for 3 temperatures. The results, indicated in figure 7.5b, are slightly better then those obtained with the second TMAE sample.

A test with C_5F_{12}

The gas which is used for the gaseous radiator, C_5F_{12}, is known for its electronegativity. A concentration of 0.2 ppm inside the drift tube would reduce the electron attenuation length to 10 m [52]. Since the gaseous radiator surrounds the drift tubes in the BRICH, care has to be taken when glueing the drift tubes. Before mounting in the BRICH all drift tubes are tested with helium in a special leak testing setup.

With the SYBIL setup a direct test for leaks on one of the bitubes was done. About 1 litre of C_5F_{12} was poured inside the vessel. Since the room temperature was above 30°C the liquid evaporated quickly, filling the vessel with a concentration of about 10% of C_5F_{12}. No measurable influence on the attenuation length was observed.

7.5 Distortions in the electron drift

In order to have a good 3-dimensional reconstruction of the photon conversion points, the distortions in the paths of the drifting electrons should be small. The distortions in the drift tube can be separated from the distortions in the transfer region, which is a space of 5 mm between the drift tube and the gating plane of the wire chamber; the voltage across this region can be set separately. Unless otherwise stated the measurements described in the following sections have been performed in a gas mixture consisting of 80% methane and 20% ethane with an admixture of about 10 ppm TMAE. The measurements have been performed without the use of the gating system.

7.5.1 Distortions in the x-coordinate

The distortions in the x-coordinate are measured with the laser beam parallel to the y-coordinate. Generally a scan is made from the side window inwards over 7 cm. The

difference Δx between the measured x-coordinate x_m and the real x-coordinate x_r is:

$$\Delta x = x_m - x_r \qquad (7.8)$$

The transfer region

The distortions due to a mismatch of the voltage over the transfer region are independent of the distortions in the drift tube. This is illustrated in figure 7.6a, 7.6b and 7.6c where in each plot for a different drift distance the distortions are shown for three voltage differences over the transfer region. The measurements were performed with a field strength of $E_{dr} = 0.68$ kV/cm. At that time it was not possible to reach the side wall, $x_r=0$, with a vertical laser beam. Generally speaking the distortions over the transfer region are minimal when the field strength in the transfer region is equal to the fi. 'd strength in the drift tube. In the case illustrated, 340 V over the transfer region (5 mm) was considered to be optimum.

The drift tube

Figure 7.6a, 7.6b and 7.6c show that the distortions in the drift tube increase with the drift distance. The region where distortions are measured has a width of 40 mm. In figure 7.6d the distortions are shown for 4 different field strengths with the laser positioned at window 5 i.e. at the maximal drift distance. The distortions decrease with increasing field strength. This is also illustrated in figure 7.6e where the distortions are shown as a function of the drift distance for 4 different field strengths when the laser is positioned 5 mm away from the side wall. The distortions increase linearly with the drift distance, in accordance with a constant force acting on the drifting electrons caused by a positive ion space charge in the drift tube. The measurements were repeated with a gas mixture consisting of 50% methane and 50% ethane. No differences in the distortions were observed.

The calibration system

At the drift field foreseen for the BRICH (0.53 kV/cm) the maximal distortions for distances with respect to the side wall of 0 mm, 10 mm and 20 mm are 6.7 mm, 4.6 mm and 2.8 mm respectively. The errors introduced by these distortions are unacceptable. With the calibration system (described in section 4.3.6) that is mounted on every drift tube the distortions can be measured and corrected. To illustrate the possibilities a comparison is made in figure 7.6f between distortions measured with the laser beam and distortions measured with the calibration system. An accuracy of 1 mm seems to be feasible.
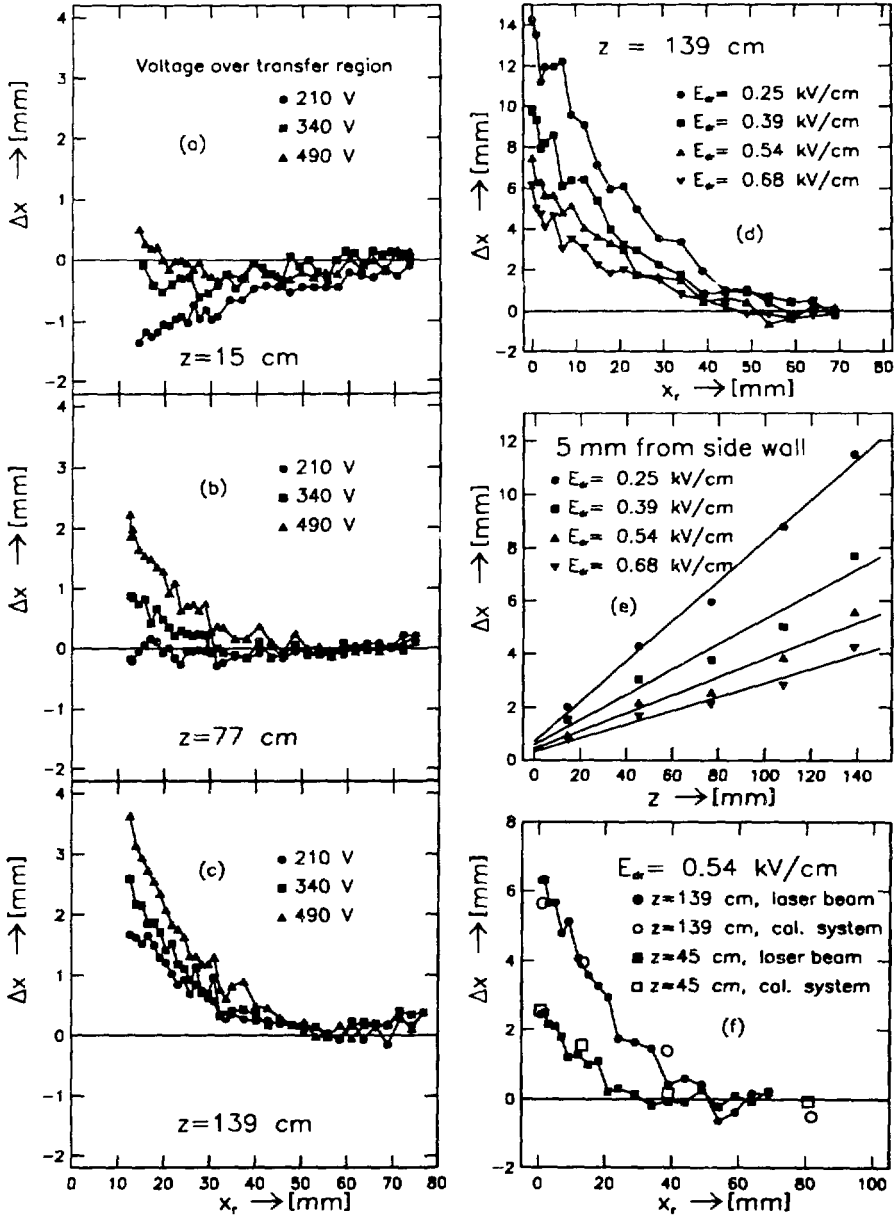
Figure 7.6: Various measurements of distortions in the x-direction; see text for explanation.

7.5.2 Distortions in the y-coordinate

The distortions in the y-coordinate are measured with a horizontal laser beam, i.e. parallel to the x-coordinate. At every window a scan can be made from top wall to bottom wall of the drift tube. The difference Δy between the measured y-coordinate y_m and the real y-coordinate y_r is:

$$\Delta y = y_m - y_r \tag{7.9}$$

The transfer region

The distortions in the y-coordinate are extremely sensitive to the value of the voltage over the transfer region. This is illustrated in figure 7.7a. It has been observed that the optimum transfer voltage is different for each combination of drift tube and wire chamber. After installation in the BRICH it should be adjusted for each bitube individually.

The drift tube

Two measurements of distortions in the y-coordinate for drift distances of 77 cm and 139 cm are shown in figure 7.7b and 7.7c. The positions of the walls are indicated by straight lines. When the transfer field is well adjusted the remaining distortions are small. This is a consequence of the trapezoidal shape of the drift tubes due to which the electrons effectively drift away from the walls. The effect of space charge is small in this direction.

7.5.3 Distortions in the z-coordinate

To measure a deviation of 1 mm on a drift distance of 1 m requires the drift velocity to be stable within 0.1%. Distortions in the z-coordinate have only been recorded in correlation with distortions in the y-coordinate. In figure 7.7d and 7.7e Δz is shown, expressed in mm, as a function of the y-coordinate. The distortions are comparable in size to those in the y-coordinate.

7.6   The absorption length for laser light in TMAE

If the laser beam is shot through the drift tube in the x-direction, the laser light is absorbed by the TMAE molecules in the drift tube according to:

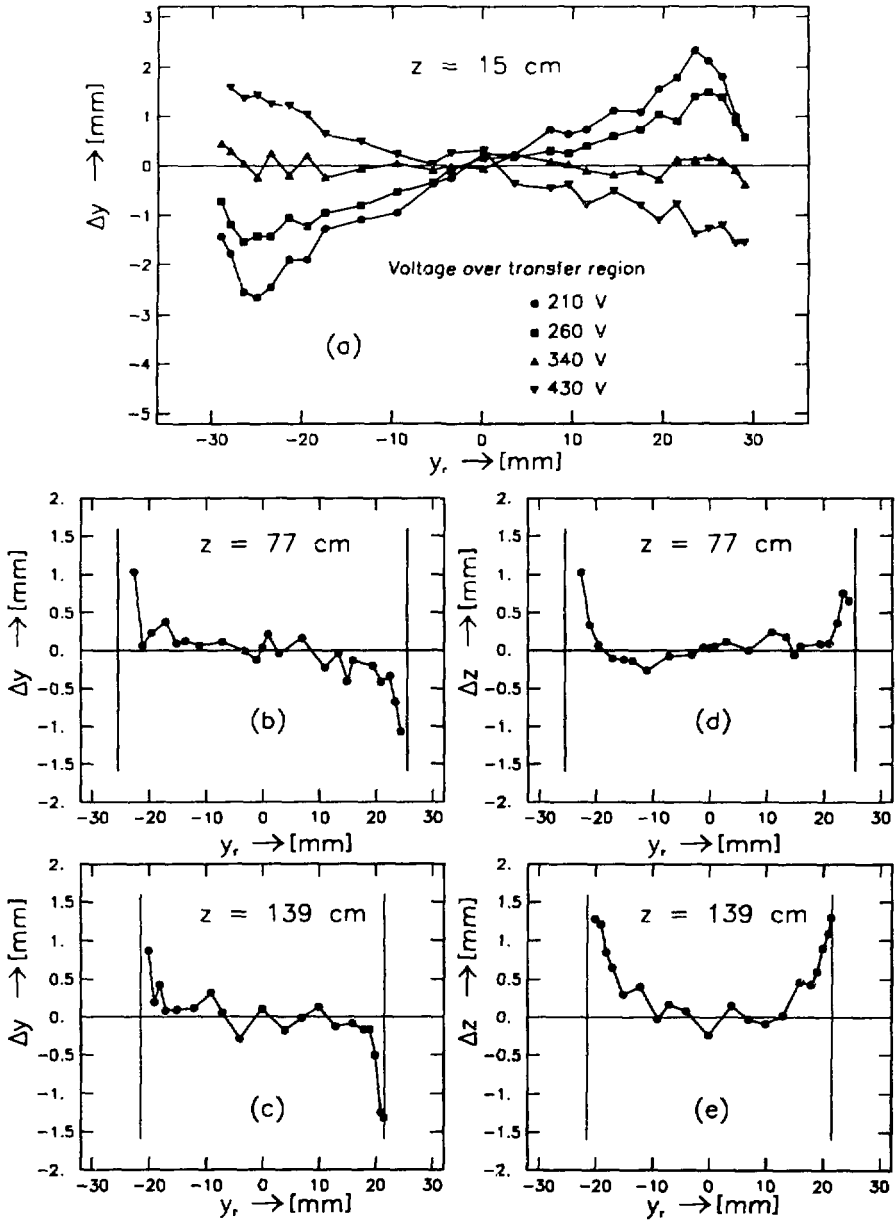$$N(x,T) = N_0 \cdot \exp -\frac{x}{l_l(T)} \tag{7.10}$$

Figure 7.7: Various measurements of distortions in the y and z-coordinate; see text for explanation.
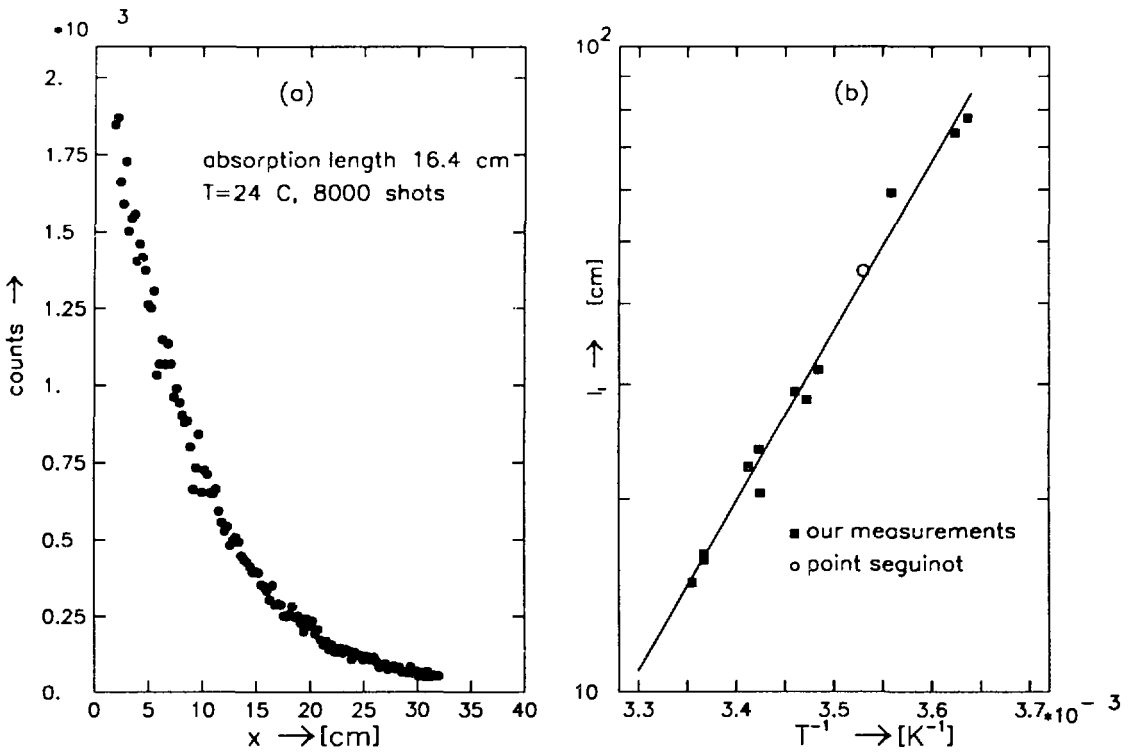
Figure 7.8: (a) Absorption length measurement with temperature of TMAE bubbler of 24°C; (b) measured absorption lengths as a function of the inverse TMAE temperature, with the best fit to the data.

where $l_l(T)$ is the absorption length for photons with a wavelength of 337 nm, T is the temperature of the TMAE bubbler and $N(x, T)$ is the intensity after a distance x. The parameter $l_l(T)$ is introduced to simplify the notation. A comparison between equation 4.3 and 7.10 shows that $l_l(T) = l_a(337nm, T)$.

Photons with a wavelength of 337 nm can ionize TMAE molecules only in a two step process. This means that the probability for ionization is proportionally to the square of the laser beam intensity. Consequently the attenuation length observed in the measured exponential distribution of the number of counts per wire is half of the real photon absorption length.

An example is shown in figure 7.8a; 8000 laser shots have been recorded at a TMAE temperature of 24°C. The wires close to the side walls ($x = 0$ mm and $x = 33.7$ mm) are not considered because of the distortions mentioned in section 7.5.1. An exponential fit to the distribution gives an attenuation length of 8.2 cm; thus the absorption length of laser light in TMAE vapour corresponding to a temperature of 24°C is: $l_l(24°C) = 16.4$ cm.

In figure 7.8b an overview is given of all measurements of the absorption length versus the inverse of the TMAE temperature. The best fit through the data:

$$l_i(T) = 44.0 \cdot 10^{-3} \cdot T \cdot \exp 6353(\frac{1}{T} - \frac{1}{300}) \quad [cm] \tag{7.11}$$

is shown in the figure. Also shown is the absorption length of 45 cm measured by Seguinot et al. [59] for a TMAE temperature of 10°C which is in excellent agreement with our results.
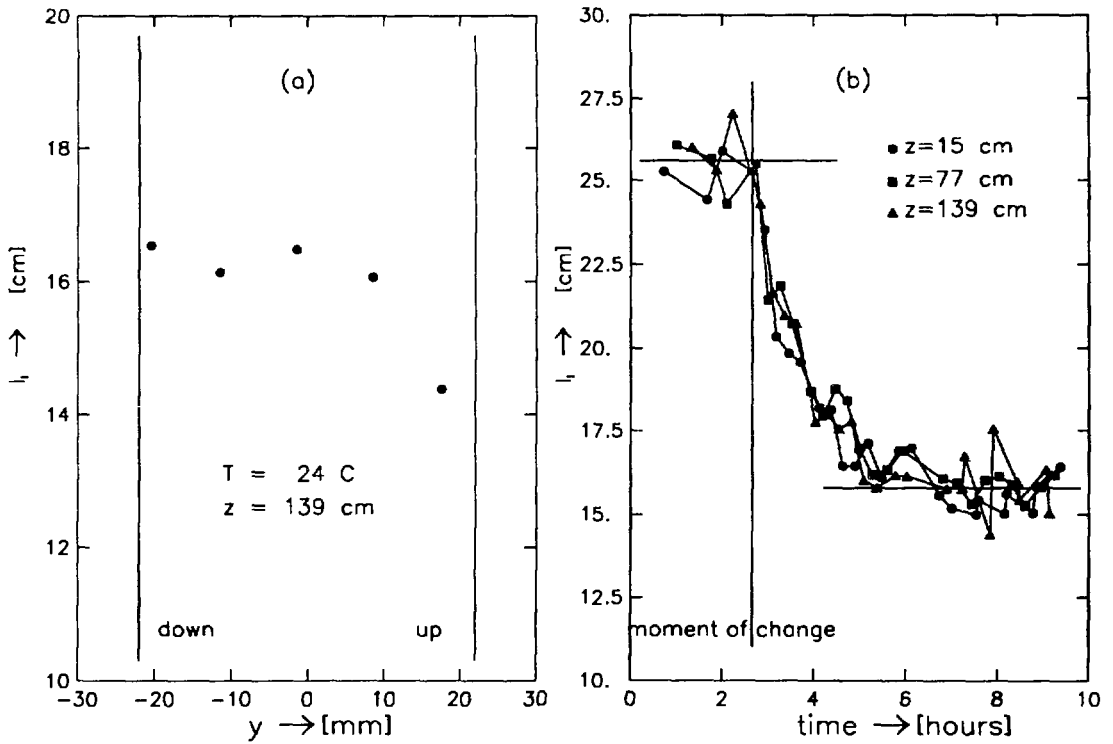
Figure 7.9: (a) The absorption length as a function of the height in the drift tube; (b) The absorption length on 3 different windows during a change of the TMAE temperature from 17°C to 24°C.

In figure 7.9a the absorption length is shown for 5 different heights in the drift tube. The data have been taken at the maximal drift distance. A small deviation is observed close to the upper quartz wall, corresponding to a *increase* of the TMAE concentration. Any stratification as expected by Arnold et al. [19] with the highest TMAE concentration at the bottom side has never been observed.

To study the mixing of the drift gas inside the drift tube the absorption length was monitored at 3 different drift distances during a change in the TMAE temperature (figure

7.9b). First some measurements have been made with a temperature of 17°C (l_l=25.6 cm). Then the temperature of the water bath, in which the bubbler is immersed, was quickly changed to 24°C and kept constant at that value. After about 4 hours the whole system was stable and the density of the TMAE vapour inside the tube was corresponding to the bubbler temperature of 24°C (l_l=15.8 cm). The absence of any difference between the measurements at the 3 different windows leads to the conclusion that the mixing of the gas inside the drift tube is good. The time constant observed -1 hour- is as expected on the basis of the gas flow and the volume of the drift tube.

7.7 Conclusions; implications for the BRICH

An electron attenuation length bigger than 10 m is feasible provided the TMAE is thoroughly cleaned and the gas system is constructed with care. The glueing in combination with the leak testing of the drift tubes guarantees a tightness to C_5F_{12} below a level of 0.2 ppm.

The mixing of the gas inside the drift tube is good. No stratification has been observed. The vapour pressure of the TMAE inside the drift tubes corresponds accurately to the temperature of the TMAE bubbler.

The initial working voltage of the BRICH will be -80 kV. In a gas mixture consisting of 80% methane and 20% ethane this means that the longitudinal diffusion coefficient is 170 $\mu m/\sqrt{cm}$ leading to an average longitudinal diffusion over the drift tube of 1.5 mm. The transverse diffusion is slightly bigger: 205 $\mu m/\sqrt{cm}$, but will be reduced by the presence of the magnetic field. The mean value of the factor $1 + \omega^2 l^2/v^2$ in equation 3.45 is about 4.0 for the gas mixture in a magnetic field of 1.2 T [85]. As a result the average transverse diffusion is 0.5 mm.

An increase of the ethane fraction in the gas mixture will slightly decrease the diffusion. With an ethane fraction of 50% the longitudinal diffusion coefficient is 157 $\mu m/\sqrt{cm}$ leading to an average diffusion over the drift tube of 1.4 mm. A further increase of the ethane fraction has hardly any influence on the longitudinal diffusion coefficient [50].

Even after an electron drift of 1.5 m the distortions in the y and z-coordinate are small. This is not the case for the distortions in the x-coordinate but those can be measured with the calibration system. The correction introduces an error of approximately 1 mm.

The spatial resolution in the x-coordinate is determined by the resolution of the wire chamber and the transverse diffusion, 0.8 mm and 0.5 mm respectively. This results in a total error of 0.9 mm. Close to the side walls the resolution increases to 1.4 mm due to the error introduced by the correction for the distortion.

The position resolution in the y-coordinate is dominated by the 1.7 mm resolution of the wire chamber. Due to the transverse diffusion the resolution will increase slightly to 1.8 mm.

The drift time is measured with an accuracy of 8 ns, introducing an error of 0.2 mm. This gives a negligible contribution to the position resolution in the z-coordinate that is dominated by the longitudinal diffusion: 1.5 mm. The error would reduce strongly if the barrel RICH could be operated at a higher voltage.

It can be concluded that the average resolution (rms) for the x, y and z-coordinates of the Čerenkov photon conversion points, in the DELPHI barrel RICH detector as it is presently operational, is 0.9, 1.8 and 1.5 mm respectively.

References

[1] The DELPHI collaboration, *The technical proposal*, DELPHI 83-66 (1983).

[2] The DELPHI collaboration, *The progress report*, DELPHI 84-60 (1984).

[3] J.V. Jelley, *Čerenkov radiation and its applications*, Pergamon Press (1958).

[4] V.P. Zrelov, *Čerenkov radiation in high-energy physics*, part 1 and 2, Israel Program for Scientific Translations (1970).

[5] J. Litt and R. Meunier, *Čerenkov counter technique in high-energy physics*, Ann. Rev. Nucl. Sci. 23 (1973) 1.

[6] J. Séguinot and T. Ypsilantis, *Photo-ionization and Čerenkov ring imaging*, Nucl. Instr. and Meth. 142 (1977) 377.

[7] R.A. Holroyd et al., *Measurement of the quantum efficiency of TMAE and TEA from threshold to 120 nm*, CRID memo 18, SLAC (1986); slightly modified published in Nucl. Instr. and Meth. A261 (1987) 440.

[8] G. Charpak, *Some recent steps in the evolution of gaseous detectors*, Physica Scripta T3 (1983) 7.

[9] G. Lenzen and J. Werner, *On the N_0 of the barrel and forward RICH counters*, DELPHI 87-94 RICH-29 (1987).

[10] J. Séguinot, J. Tocqueville and T. Ypsilantis, *Imaging Čerenkov detector: photo-ionization of tri-ethyl-amine*, Nucl. Instr. and Meth. 173 (1980) 283.

[11] D.F. Anderson, *A photoionization detector for the detection of xenon light*, IEEE TNS NS-28 (1981) 842.

[12] F. Sauli, *New developments in gaseous detectors*, CERN-EP 82-130 (1982).

[13] G. Charpak and F. Sauli, *The multistep avalanche chamber: a new high-rate, high-accuracy gaseous detector*, Physics Letters 78B (1978) 523.

[14] T. Ekelöf et al., *The Čerenkov ring imaging detector: recent progress and future development*, Physica Scripta 23 (1981) 718.

[15] E. Barrelet et al., *A two-dimensional, single-photoelectron drift detector for Čerenkov ring imaging*, Nucl. Instr. and Meth. 200 (1982) 219.

[16] Y. Giomataris, *A new candidate for the barrel RICH gas radiator*, DELPHI 86-72 RICH-19 (1986).

[17] T. Ekelöf, *The experimental method of ring-imaging Čerenkov (RICH) counters*, DELPHI 85-11 RICH-5 (1985).

[18] G. Hallewell *et al.*, *Progress report on the SLD Cerenkov ring imaging detector system*, SLAC-PUB-4405 (1987).

[19] R. Arnold *et al.*, *A ring imaging Cerenkov detector, the DELPHI barrel RICH prototype*, part A and B, Nucl. Instr. and Meth. A270 (1988) 255-318.

[20] T. Ypsilantis, *Cerenkov ring imaging*, Physica Scripta 23 (1981) 371.

[21] G. Charpak *et al.*, *The use of multiwire proportional counters to select and localize charged particles*, Nucl. Instr. and Meth. 62 (1968) 262.

[22] For overview articles we refer to the following proceedings of the Vienna Wire Chamber Conference, Nucl. Instr. and Meth. 176 (1980), Nucl. Instr. and Meth. 252 (1986), Nucl. Instr. and Meth. A283 (1989).

[23] F. Sauli, *Principles of operation of multiwire proportional and drift chambers*, CERN 77-09 (1977).

[24] L.G.H. Huxley and R.W. Crompton, *The diffusion and drift of electrons in gases*, John Wiley & Sons, (1974).

[25] W.N. English and G.C. Hanna, *Grid ionization chamber measurements of electron drift velocities in gas mixtures*, Can. J. Phys. 31 (1953) 768.

[26] L. G. Christophorou, *Atomic and molecular radiation physics*, John Wiley & sons, (1971).

[27] J.H. Parker and J.J. Lowke, *Theory of electron diffusion parallel to electric fields. I. Theory*, Phys. Rev. 181 (1969) 290.

[28] J.J. Lowke and J.H. Parker, *Theory of electron diffusion parallel to electric fields. II. Application to real gases*, Phys. Rev. 181 (1969) 302.

[29] L.S. Frost and A.V. Phelps, *Rotational and momentum transfer cross sections for electrons in H_2 and N_2 from transport coefficients*, Phys. Rev. 127 (1962) 1621.

[30] A.G. Engelhardt and A.V. Phelps, *Transport coefficients and cross sections in argon and hydrogen-argon mixtures*, Phys. Rev. 133 (1964) A375.

[31] A.G. Engelhardt, A.V. Phelps and C.G. Risk, *Determination of cross sections for electrons in N_2 using transport coefficients*, Phys. Rev. 135 (1964) A1566.

[32] L.S. Frost and A.V. Phelps, *Momentum-transfer cross sections for slow electrons in He, Ar, Kr and Xe from transport coefficients*, Phys. Rev. 136 (1964) A1538.

[33] R.D. Hake and A.V. Phelps, *Momentum-transfer and inelastic-collision cross sections for electrons in O_2, CO and CO_2*, Phys. Rev. 158 (1967) 70.

[34] E.B. Wagner, F.J. Davis and G.S. Hurst, *Time-of-flight investigations of electron transport in some atomic and molecular gases*, J. Chem. Phys. 47 (1967) 3138.

[35] V. Palladino and B. Sadoulet, *Application of the classical theory of electrons in gases to multiwire proportional and drift chambers*, LBL-3013 (1974).

[36] V. Palladino and B. Sadoulet, *Application of classical theory of electrons in gases to drift proportional chambers*, Nucl. Instr. and Meth. 128 (1975) 323.

[37] G. Schultz and J. Gresser, *A study of transport coefficients of electrons in some gases used in proportional and drift chambers*, Nucl. Instr. and Meth. 151 (1978) 413.

[38] E. Mathieson and N. El Hakeem, *Calculation of electron transport coefficients in counting gas mixtures*, Nucl. Instr. and Meth. 159 (1979) 489.

[39] B. Schmidt, *Drift properties of electrons in methane and methane noble gas mixtures*, Nucl. Instr. and Meth. A252 (1986) 579.

[40] S.F. Biagi, *A multi-term Boltzmann analysis of drift velocity, diffusion, gain and magnetic field effects in argon, methane and water vapour mixtures*, Nucl. Instr. and Meth. A283 (1989) 716.

[41] K. Kleinknecht, *Detektoren für Teilchenstrahlung*, Teubner (1984).

[42] G.D. Alkhazov *Statistics of electron avalanches and ultimate resolution of proportional counters*, Nucl. Instr. and Meth. 89 (1970) 155.

[43] R. Bouclier *et al.*, *Progress in Čerenkov ring imaging*, Nucl. Instr. and Meth. 205 (1983) 403.

[44] F. Bird *et al.*, *Charge division using carbon filaments for obtaining coordinate information from detection of single electrons*, IEEE NS-33 no1 (1986) 261.

[45] P. Coyle, *Electron attachment in drift gases: implications for CRID*, CRID memo 51, SLAC.

[46] F. Bloch and N.E. Bradbury, *On the mechanism of unimolecular electron capture*, Phys. Rev. 48 (1935) 689.

[47] A. Herzenberg, *Attachment of slow electrons to oxygen molecules*, J. Chem. Phys. 51 (1969) 4942.

[48] M. Huk, P. Igo-Kemenes and A. Wagner, *Electron attachment to oxygen, water and methanol in various drift chamber gas mixtures*, Nucl. Instr. and Meth. A267 (1988) 107.

[49] Y. Hatano and H. Shimamori, *Electron attachment in dense gases*, Pergamon Press (1981).

[50] H. Jansen, *Photon detection in ring imaging Cherenkov counters*, Thesis university of Leiden (1988).

[51] The barrel RICH construction group, *The DELPHI barrel RICH*, Addendum to the technical proposal, DELPHI 86-82 RICH-22 (1986).

[52] D. Fraissard *et al.*, *Electron attachment of C_5F_{12} to be used as a gas radiator in the barrel RICH detector of DELPHI*, Nucl. Instr. and Meth. A252 (1986) 524.

[53] G. Kalkanis and E. Rosso, *The inverse power law model for the life time of a mylar-polyurethane laminated DC HV insulating structure*, DELPHI 88-58 RICH 12 (1988).

[54] G. Kalkanis *et al.*, *Tests of the DELPHI barrel RICH electrical HV insulator*, Nucl. Instr. and Meth. A283 (1989) 37.

[55] P. Baillon *et al.*, *Production of 300 paraboloidal mirrors with high reflectivity for use in the BRICH*, Nucl. Instr. and Meth. A277 (1989) 338.

[56] M. Bosteels, Y. Giomataris and T. Ypsilantis, *Saturateur de vapeurs*, CERN IM/84-1 (1984).

[57] S. Flügge, *Prinzipien der Thermodynamik und Statistik*, Handbuch der physik, volume III/2, Springer-Verlag (1959).

[58] Y. Giomataris *et al.*, *Vapor pressure of TMAE*, DELPHI 86-17 RICH-15 (1986).

[59] J. Séguinot and T. Ypsilantis, private communications.

[60] R.T. Rewick *et al.*, *TMAE: analysis and compatibility with common laboratory materials*, SLAC-PUB 4115 (1986).

[61] R.J. Apsimon *et al.*, *The design of the optical components and gas control systems of the CERN omega ring imaging Čerenkov detector*, Nucl. Instr. and Meth. A241 (1985) 339.

[62] P. Baillon *et al.*, *Measurements of the efficiency of MWPC's in a magnetic field up to 1.2 Tesla*, DELPHI 85-99 RICH-10 (1986).

[63] F. Hartjes, J. Konijn and Y. Peng, *Straight line calibration in drift chambers over eight meters*, Nucl. Instr. and Meth. A269 (1988) 544.

[64] G. Hubricht *et al.*, *Ionization of counting gases and ionizable gaseous additives in proportional chambers by UV lasers*, Nucl. Instr. and Meth. 228 (1985) 327.

[65] E. Christophel, *Hybrid amplifiers for the barrel RICH*, DELPHI 84-28 ELEC-2 (1984).

[66] J.D. Berst, *TDC for the barrel RICH*, DELPHI 84-28 ELEC-2 (1984).

[67] E. Christophel, *FASTBUS discriminator board*, DELPHI 85-18 ELEC-17 (1986).

[68] G. Delavallade and J.P. Vanuxem, *The LTD: a FASTBUS time digitizer for LEP detectors*, Nucl. Instr. and Meth. A252 (1986) 596.

[69] D. Bloch *et al.*, *The multiwire proportional chambers of the DELPHI barrel RICH*, Nucl. Instr. and Meth. A273 (1988) 847.

[70] D. Bloch *et al.*, *Analysis of Čerenkov rings with the final chambers of the DELPHI barrel RICH*, DELPHI 87-61 RICH 26 (1987).

[71] M.A.E. Schyns, *Multiwire proportional chambers for the DELPHI barrel RICH; tests with single electrons*, doctoraal scriptie, University of Amsterdam (1989).

[72] M. Dracos and D. Loukas, *Experimental study of the single electron response of the DELPHI barrel RICH MWPC's*, CRN/HE 89-06 (1989).

[73] J. Va'vra, *Review of wire chamber aging*, SLAC-PUB-3882 (1986).

[74] F. Sauli, *When everything was clear*, CERN-EP 86-24 (1986).

[75] J. Va'vra, *Wire aging of hydrocarbon gases with TMAE additions*, SLAC-PUB-4116.

[76] F. James and M. Roos, *Function minimization and error analysis*, CERN program library D506 (1989).

[77] G. van Apeldoorn, D. Langerveld et al., *Gating the MWPC's of the DELPHI barrel RICH*, Nucl. Instr. and Meth. A283 (1989) 767.

[78] R.F. Holsinger and C. Iselin, *The CERN POISSON program package*, CERN program library T604 (1984).

[79] J.J.M. Timmermans, private communications.

[80] F. Hahn et al., *Long electron drift in TMAE-doped gas in the barrel RICH detector*, Nucl. Instr. and Meth. A283 (1989) 686.

[81] R. Arnold et al., *Photosensitive gas detectors for the ring-imaging Čerenkov (RICH) technique and the DELPHI barrel RICH prototype*, Nucl. Instr. and Meth. A252 (1986) 188.

[82] F. Hahn, *Untersuchungen zur Elektronendrift im Photondetektor des DELPHI Barrel RICH*, diplomarbeit University of Wuppertal (1989).

[83] G. Lenzen, private communications.

[84] L. Wong, J. Armitage and J. Waterhouse, *Measurements of the anisotropy ratio between longitudinal and transverse diffusion in argon based gas mixtures*, Nucl. Instr. and Meth. A273 (1988) 476.

[85] P. Coyle et al., *Lorentz angle studies for the SLD endcap Čerenkov ring imaging detector*, Nucl. Instr. and Meth. A273 (1988) 858; also A. Hallgren, private communications.

Summary

Charged particles with an energy between 2 GeV and 25 GeV can be identified in the DELPHI barrel RICH detector by using the technique of Čerenkov ring image detection. The method of identification is based on a determination of the Čerenkov angle by measuring the positions of the emitted Čerenkov photons to high precision in a photon detector. The resolution that can be obtained depends mainly on the chromatic dispersion in the radiators and on the resolution of the photon detector. One photon detector is used in the barrel RICH in combination with two radiators, a gaseous radiator C_5F_{12} and a liquid radiator C_6F_{14}. The choice of these two fluorocarbons necessitates that the barrel RICH be operated at a temperature of 40°C and at an overpressure of 0.3 bar. The latter is necessary to improve the separation between kaons and protons.

The photon detector consists of 48 drift tubes, constructed from quartz plates, each equipped with a wire chamber at its end. The tubes are filled with a drift gas consisting of 75% methane and 25% ethane with a small admixture of TMAE vapour. The Čerenkov photons can liberate electrons, called photoelectrons, from the TMAE molecules.

It is shown in this thesis that with the barrel RICH detector an efficient photon detection and an accurate localization of the photon conversion points is possible.

An attenuation length exceeding 10 m can be obtained for the drift of single electrons if the liquid TMAE is properly cleaned by water washing and vacuum distillation and care is taken with the choice of construction materials of the photon detector and the gas system.

Several wire chamber prototypes have been tested before the design was finalized. In the realistic situation of a beam test the anode and cathode detection efficiencies were measured to be 98% and 90% respectively. The gating system which is essentially meant to prevent the occumulation of ion space charge in the drift tubes, works to satisfaction.

The spatial resolution of the photon detector is determined by the resolution of the wire chamber, the accuracy of the drift time measurement, the distortions in the paths of the drifting electrons and the longitudinal and transverse diffusion of the electrons.

The resolution of the wire chamber has been measured to be 0.8 mm in the x-coordinate (measured with the anode wires) and 1.7 mm in the y-coordinate (measured with the cathode strips). The error in the z-coordinate introduced by the drift time measurement is 0.2 mm. The distortions in the paths of the drifting electrons have been measured both in the x and y-direction. It is shown that, without the use of the gating system, the distortions are negligible except for a limited region close to the side walls. The longitudinal

and transverse diffusion coefficients have been measured as a function of the field strength for two different gas mixtures.

From these measurements it can be concluded that for the working conditions of the barrel RICH detector, the average spatial resolution for the x, y and z-coordinates of the Čerenkov photon conversion points is 0.9, 1.8 and 1.5 mm respectively.

Samenvatting

De centrale RICH detektor is onderdeel van het DELPHI-experiment. In deze detektor kunnen geladen deeltjes met een energie tussen 2 GeV en 25 GeV worden geïdentificeerd door de Čerenkov-hoek te meten waaronder Čerenkov-straling wordt uitgezonden. De nauwkeurigheid waarmee de Čerenkov-hoek kan worden bepaald is vooral afhankelijk van de chromatische dispersie in de radiatoren en het scheidend vermogen van de fotonendetektor.

In de centrale RICH wordt één fotonendetektor gecombineerd met twee radiatoren, een gasradiator gevuld met C_5F_{12} en een vloeistofradiator gevuld met C_6F_{14}. De keuze van deze radiatoren impliceert dat de centrale RICH bedreven wordt bij een temperatuur van 40°C en een overdruk van 0.3 bar. Dit laatste om de identificatie van kaonen en protonen te verbeteren.

De fotonendetektor bestaat uit 48 driftbuizen, die elk uit kwartsplaten geconstrueerd zijn. Iedere driftbuis wordt uitgelezen met behulp van een dradenkamer. Het gasmengsel in de driftbuizen bestaat uit 75% methaan en 25% ethaan waaraan een kleine concentratie TMAE damp is toegevoegd. Door foto-ionisatie van de TMAE molekulen worden vrije elektronen gecreëerd, die vervolgens in een elektrisch veld naar de dradenkamer driften om aldaar te worden gedetekteerd.

In dit proefschrift wordt aangetoond dat een efficiënte fotonendetektie en een nauwkeurige bepaling van ieder foto-conversiepunt mogelijk is met de centrale RICH detektor.

Een verzwakkingslengte voor het verlies van driftende elektronen groter dan 10 m kan worden bereikt, mits de TMAE vloeistof goed gereinigd is d.m.v. wassen met water en distillatie onder vacuum en mits de juiste materialen gebruikt worden voor de fotonendetektor en het gassysteem.

De testresultaten van diverse prototypes hebben geleid tot het uiteindelijke ontwerp van de dradenkamer. Onder de realistische omstandigheden van een bundel test zijn de detektie-efficiëncies van anodes en kathodes gemeten als respektievelijk 98% en 90%.

De nauwkeurigheid in de plaatsbepaling van de fotonendetektor wordt bepaald door het scheidend vermogen van de dradenkamer, de onzekerheid in de meting van de drifttijd, verstoringen in de banen va . de driftende elektronen en de longitudinale en transversale diffusie van de elektronen.

Het scheidend vermogen van de dradenkamer is 0.8 mm in de x-coördinaat (gemeten met de anodedraden) en 1.7 mm in de y-coördinaat (gemeten met de kathodestrippen). De meting van de drifttijd introduceert een te verwaarlozen fout in de z-coördinaat van

0.2 mm. De verstoringen in de banen van de elektronen zijn gemeten in zowel de x als de y richting. Daarbij blijkt dat alleen in de x richting, dichtbij de zijkanten van de driftbuis meetbare afwijkingen optreden. De longitudinale en transversale diffusie coëfficiënten zijn gemeten als funktie van de veldsterkte voor twee gasmengsels.

De conclusie uit deze metingen is dat voor de omstandigheden zoals die in de centrale RICH gelden, de gemiddelde nauwkeurigheid van de plaatsbepalingen in de x, y en z-coördinaat gelijk zijn aan respektievelijk 0.9, 1.8 en 1.5 mm.

Acknowledgements

Many people contributed to the work described in this thesis. I would like to mention some of them by name, at the risk of doing injustice to many others.

The wire chamber tests performed at NIKHEF-H would not have been possible without the strong support of Gras van Apeldoorn, Dick Toet and Emile Schyns. The test setup and wire chambers were designed by Auke Korporaal and Theo Ypma and have been constructed in the workshop of NIKHEF-H under the direction of Nico de Koning.

Several people from CRN Strasbourg contributed to the beam test. Large contributions among others came from Wojciech Dulinski, Edmond Christophel and Pierre Juillot, who also kindly provided some figures for this thesis.

Jan Timmermans introduced me patiently to the secrets of the program POISSON and its extension written by him.

During my stay at CERN I worked in "the SYBIL team" which forms part of the EF/AT group managed by Paul Queru and Ettore Rosso. Working together with Ferdinand Hahn and Stefan Haider under the inspiring guidance of Wolfgang Klempt was always enjoyable. It is a great pleasure when your collegues are also your best friends. I would like to mention Ingo Herbst, Paul Baillon, George Lenzen and Hans Jansen for the interest they showed in our work and for the many fruitful discussions.

Curriculum Vitae

De schrijver van dit proefschrift werd op 1 augustus 1961 geboren te Poortugaal. In mei 1979 behaalde hij het eindexamen atheneum-B aan de scholengemeenschap "Albert Einstein" te Hoogvliet. Daarna begon hij met de studie technische natuurkunde aan de Technische Hogeschool te Delft. Het kandidaatsexamen werd behaald in april 1983. Het vierde- en vijfdejaarsonderzoek werd verricht in de vakgroep "Instrumentatie Stralingsonderzoek" o.l.v. dr.ir. R.W. Hollander en dr.ir. C.W.E. van Eijk. Tijdens deze periode heeft hij gewerkt aan het testen van een driftkamer ten behoeve van een verstrooiings-experiment bij NIKHEF-K en aan de ontwikkeling van twee gasscintillatie detektoren ten behoeve van het LEAR-experiment PS174 op het instituut CERN te Geneve.

In de zomer van 1984 verbleef hij gedurende 3 maanden als zomerstudent op het CERN waar o.l.v. dr. F. Piuz ervaring werd opgedaan in het gebruik van microstrip detektoren in de hoge-energie-fysica.

Het ingenieursexamen werd behaald in augustus 1985. Na een korte periode van 3 maanden als medewerker aan de TH-Delft ter afronding van het laatste onderzoek werd in december 1985 begonnen met een promotieonderzoek in dienst van de stichting "Fundamenteel Onderzoek der Materie" (FOM) aan het "Nationaal Instituut voor Kernfysica en Hoge-Energie-Fysica" (NIKHEF-H) te Amsterdam. Een deel van dit onderzoek werd gedurende 2 jaar verricht op het CERN.